NANO-SCALE INTERACTIONS OF PARTICLES AND DROPS WITH HETEROGENOUS SURFACES

by

RUI ZHANG

A dissertation submitted to the Graduate Faculty in Physics in partial fulfillment of the requirements for the degree of Doctor of Philosophy
The City University of New York

2013

©2013

RUI ZHANG

All Rights Reserved

This manuscript has been read and accepted for the Graduate Faculty in Physics in satisfaction of the dissertation requirement for the degree of Doctor of Philosophy

Prof. Joel Koplik

Date — **Chair of Examining Committee**

Prof. Steven G. Greenbaum

Date — **Executive Officer**

Prof. Jeffrey Morris

Prof. Taehun Lee

Prof. Charles Maldarelli

Prof. German Drazer
Supervisory Committee

THE CITY UNIVERSITY OF NEW YORK

Abstract

NANO-SCALE INTERACTIONS OF PARTICLES AND DROPS WITH HETEROGENOUS SURFACES

by

Rui Zhang

Adviser: Joel Koplik

Recent technological developments enable one to study the behavior and interactions of particles and drops with heterogeneous surfaces at microscopic resolution, and investigate their possible applications. In this thesis, we use the microscopic calculational technique of molecular dynamics simulation, augmented by other continuum methods as appropriate, to study some prototypical examples. For applications to particle separation, we consider on the transport of particles by flow through a narrow channel of which one side has a stripe pattern of alternating wettabilities. We first consider van der Waals forces alone. The particle-wall interaction can either trap particles on the attractive stripes or deflect the trajectories of mobile particles away from the mean flow direction. Using molecular dynamics we determine how the migration angle of finite-sized rigid particles differs from the imposed fluid flow. The effects of

electrostatic interactions are considered by decorating the particles and walls with opposite charges, resulting in significantly more trapping and larger deflection angles. We then use Langevin equations to simulate larger particles in the van der Waals case, and compare the results to the MD simulations. From the analysis of the associated Fokker-Planck equation we further obtain bounds on the deflection angle. The second problem involving fluid-solid interactions is that of nano-sized drop impact on a surface, which are flat, curved or pillared, with either homogeneous interactions or cross-shaped patterns of wettability. From the simulations we observe drop bouncing, sticking, spreading or disintegrating, depending on impact velocity and surface properties. In contrast to macroscopic observation, MD shows that the presence or absence of vapor has no effect on the onset of splashing. We argue that this difference is a direct consequence of drop size. For low velocity impacts, we compare MD results with continuum lattice Boltzmann methods at the same Reynolds and Weber numbers. In most situations we observe similar drop behavior at both length scales, with the best quantitative agreement for low impact velocities on wettable surfaces. We attribute the discrepancy for relatively high impact velocities to compressibility effects, while the disagreement on non-wetting surfaces is associated with different treatments of the liquid-solid boundary conditions.

Acknowledgments

I am deeply grateful for my supervisor, Professor Joel Koplik, Levich Institute and Physics Department, City College of New York, for initiating this work and providing continual support of my research.

I am also grateful for my collaborator or supporter Professor Taehun Lee, Department of Mechanical Engineering, CCNY, Professor German Drazer, Department of Mechanical and Aerospace Engineering Rutgers - The State University of New Jersey, and Prof. Jeffrey Morris, Department of Chemical Engineering, CCNY.

In addition, I am grateful for helpful discussions with Dr. Tak Shing Lo, Weikang Chen, Samaneh Farokhirad, Dr. Kevin Connington and Dr. Bo Wen. And special thank to Dr. JunJun Mao for his kind help.

Lastly, I would like to thank my parents, without whom none of this could be possible.

Contents

List of Tables

List of Illustrations

Chapter 1

Introduction

Motivated by the idea of "lab-on-a-chip", various micro or nano fluidic devices are invented and studied in the past decades[1, 2, 3, 4, 5]. Recent developments in fabrication techniques provides well-characterized surface structures with specified properties and allow ones to study the new phenomena and possible applications brought by the surface heterogeneity. Surfaces that are available for study range from chemically homogenous to randomly disordered, from hydrophilic to super-hydrophobic, and from atomically smooth to geometrically or randomly rough[6, 7, 8, 9]. By incorporating appropriate substrate surface with the multi scale fluidic device, one can use it for a wide applications. On a ratchet surface, particles or drops can be precisily manipulated, collected or removed[10, 11, 12, 13]. On a chemically gradient surface, drop can be directionally guided towards more wetting regions [14, 15]. On a 2D periodic obstacle arrays, particle transport shows directional locking effect, i.e. moving in a few specific commensurate directions of the array lattice, regardless of the flow or force field directions. The apparatus can be used for particle sorting, chromatography or clinical diagnostics [16, 17, 18, 19, 20, 21]. Drop may bounce, spread or splash as the outcome of the impact on solid surfaces and this is fundamental for the purpose of printing and quenching, etc. [22, 23, 24]

In this thesis we are attempting two prototypical problems. One is to test in multi scale that whether surface gradient method can be used to separate particles of different sizes or charges. The other one is to observe the phenomena of nano meter

sized drop impact on heterogeneous surfaces and compare the results to the macro scale drop impact.

The separation of different particulate constituents in solution has long been an important process in many industrial applications, and numerous techniques have been developed for this purpose [25]. Frequently, separation methods take advantage of the variation in physico-chemical properties between the target particles, and discriminate between them based on the small differences in their properties, leading to the fractionation of complex mixtures. Techniques such as field-flow fractionation [26] utilize a single physiochemical property to separate particles and are inherently batch processes, or else require external fields to drive separative displacement. However, continuous operation is a desirable property in any chromatography method, and techniques with this advantage that do not require external fields include pinched flow fractionation [27, 28, 29], hydrodynamic filtration [30] and hydrophoresis [31, 32, 33]. Filtration techniques lead to local accumulation of particles which then require further manipulation, but a particularly attractive feature for nanoscale processing would be autonomous operation, where the device does not require mechanical interaction, operator intervention or other forms of tuning.

These difficulties may be avoided by method based on *vector chromatography* [34, 35], a continuous separation method based on a combination of transport in one dimension with selective displacement in the orthogonal direction, which not only operates autonomously but has greater resolving power than many of the one-dimensional techniques above. [36]. In contrast to ordinary chromatography, vector chromatography separates particles not only by different transport velocities but also by their distinctive mean migration angles. One such method, deterministic lateral displacement [16, 17, 37, 38, 39] uses a two-dimensional sieving matrix which effec-

tively blocks the linear motion of larger particles and forces particles of different size to move at different angles. Although very effective in practice, the underlying mechanism leading to separation is not completely clear, and the corresponding designs are hard to optimize [40, 20, 41].

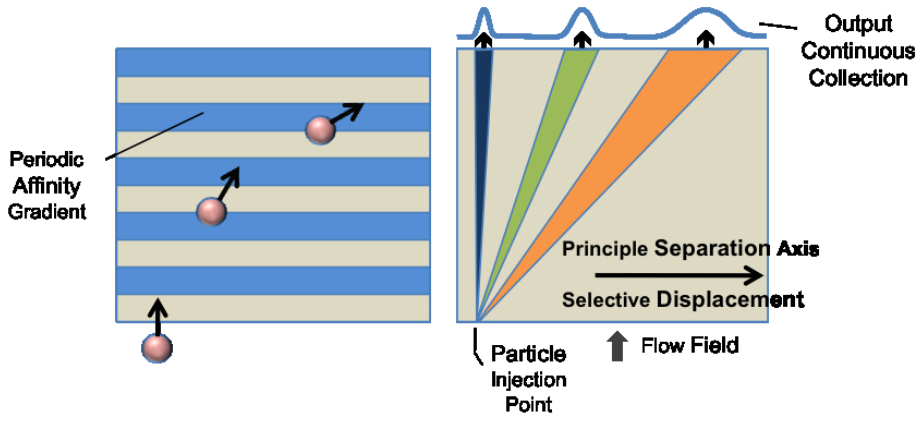

Figure 1.1 : Illustration of vector chromatography based on surface gradients.

We focus on one type of vector chromatography, the gradient surface method illustrated in Fig. 1.1, which makes use of the geometrical inhomogeneities of an attracting surface to separate particles by selectively varying the direction (and perhaps the speed) of motion according to the particle's characteristics.

We report on numerical simulations and theoretical analyses of this process, trajectory separation in the presence of a striped chemical pattern on one surface of a microfluidic channel. The results are obtained from two distinct but related calculational methods, molecular dynamics and Langevin dynamics, and a theoretical analysis based on the Fokker-Planck description of the latter method.

The impact of liquid drops on solid surfaces is an everyday phenomenon with important applications in material transport processes in industry, and whose under-

standing poses challenging questions in fluid dynamics [22, 24, 42]. The variaty of physical properties of the solid provide us with potential on the new phenomena of drop impacts[6, 7, 8, 9]. Furthermore, there are numerous possibilities for the outcome of an impact: the drop may bounce, stick, spread as a disk, spread into fingers or form a splash [43, 44, 45, 46]. A spreading liquid lamella may rupture during impact into satellite drops or fragments [46, 47, 48]. If the substrate temperature is above the liquid boiling point, the drop may levitate (the Leidenfrost effect [49]) or even leave the surface entirely, depending on its size[50]. A recent systematic review of the phenomena can be found in [43].

We provide numerical simulations with two principal motivations. First, we aim to predict in a general way how the behavior of an impacting drop is affected by the chemical and structural characteristics of the surface. Although slightly simplified physical models are used for surface properties, we hope to elucidate the trends and compare the results to experiments and earlier calculations where possible. We employ two distinct numerical simulation methods: molecular dynamics (MD), which accurately captures the behavior at the scale of individual atoms in modestly-sized systems, and the lattice Boltzmann method (LB), which solves the continuum equations of motion using a particle-based algorithm. Ostensibly the two methods operate at very different length and time scales, but in principle address the same phenomena. Our second goal in this paper is to compare the results of the two types of calculation in the non-trivial flow configurations arising in drop impact. An earlier comparison of the two methods for the confined (Poiseuille) flow of a wetting liquid [51] found good agreement, but drop impact is a more stringent test.

To anticipate the results somewhat, we find that at low values of the Reynolds and Weber numbers ($Re \lesssim 20$ and $We \lesssim 100$) the two methods produce very similar

drop behavior on wettable surfaces. On nonwettable surfaces and at higher impact velocities, and in particular in the splashing regime, deviations appear. The issue in wettability is that in the LB method, surface interactions are governed by a Cahn-Hilliard potential, and standard forms for this interaction do not appear to treat strong hydrophobicity and the consequent surface velocity slip properly. In contrast, MD methods are quite well suited to this regime, and agreement between the two methods is poor. In high velocity impacts, there is first the general issue that any splash produces a highly ramified fluid body and secondary droplets, and resolving this structure in terms of individual molecules requires a very large scale simulation. A further difficulty is that a drop several nanometers in diameter with high Re and We has a high velocity O(100 m/s), comparable to the atomic thermal velocity. One consequence is that the Mach number becomes significant and compressibility effects may appear, and a second is that impact produces temperatures exceeding the liquid/vapor coexistence value [46], and the liquid drop tends to disintegrate rather than splash in the conventional sense. Neither of these features is present in most experiments and continuum calculations, and we therefore focus on slower impacts.

A number of earlier papers have studied drop impact on heterogeneous surfaces of various kinds, using both experimental and numerical methods. Cross, stripe and chessboard chemically-patterned surfaces have been studied numerically in the lubrication approximation by Schwartz and collaborators [52, 53], using a geometry identical to one considered below. Experimentally, Vaikuntanathan *et al.* [54] considered drop impact at the junction of hydrophobic and hydrophilic half-plane surfaces, and Mock *et al.* [55] studied impacts onto hydrophilic spots and arrays of spots. A pattern made of radiating thin spokes is the subject of experiments by Lee *et al.* [56] and annular patterned surfaces are studied by Kim *et al.* [23]. Experiments by

Katsuragi [57] involve a drop impact on a granular layer surface and multiscale pillar surfaces are studied by Lohse *et al* [6, 9, 58, 59, 60].

The thesis is organized in the following: In Chapter. 2, we introduce several theoretical or numerical methods that are going to be employed in this thesis, including molecular dynamics, Langevin equations, Fokker-Planck equations and Lattice Boltzmann method. In Chapter. 3, we investigate how a stripe patterned surface can be used to separate particles by their sizes. In Chapter. 4, by comparing molecular dynamics and lattice Boltzmann method, we study the dynamics of drops impact on homogeneous or patterned surfaces of various kinds.

Chapter 2

Methodology

In this chapter, various methods, including our main approach Molecular Dynamics, are discussed.

2.1 Continuum Theory

Nano scale fluidic system involving solid particles and surfaces is considered here. In principal, *Navier-Stokes* equations[61], coupled with appropriate boundary conditions, is feasible in nano scale. However, two issues can not be covered by the *Navier-Stokes* framework: (1) Brownian Motion: at micro or nano scale, dispersed particles do "random walk" due to the thermal motion of the fluid molecules [62]; (2) Nonhydrodynamic interactions: in some applications, particle-particle interaction becomes nonhydrodynamic(hard collision) and it dominates the transport properties of the particles[20]. In addition, the liquid-solid boundary conditions are nontrivial and should be measured from a separate experiment or a molecular dynamics simulation[63, 64]. Therefore alternative theories should be considered.

To include the Brownian Motion effect of particles, *Fokker-Planck* equation and *Brownian* dynamics are introduced. *Fokker-Planck* equation claims that the spatial probability distribution function $Q(\mathbf{r}, \mathbf{t})$ of particles which are at position $\mathbf{r}$ at time t satisfies an equation of continuity[65]:

$$\frac{\partial Q}{\partial t} = \nabla \cdot \mathbf{J} = \mathbf{u}\, Q - \mathbf{M} \cdot \nabla V - k_B T\, \mathbf{M} \cdot \nabla Q \tag{2.1}$$

where the particles have mobility tensor $\mathbf{M}$ and move in a velocity field $\mathbf{u}$ under a potential V at temperature k_BT, subject to some initial condition. An equivalent form of *Fokker-Planck* equation is the *Langevin* equation which expresses the equation of motion of a single particle by[66]

$$m\frac{d\mathbf{v}}{dt} = -\gamma[\mathbf{v} - \mathbf{u}(\mathbf{r})] + \mathbf{F}_{ext} + \boldsymbol{\Gamma}(t), \tag{2.2}$$

where $\mathbf{u}(\mathbf{r})$ is the local flow velocity at the position $\mathbf{r}$ of the particle, $\gamma = 6\pi\mu R$ is the Stokes drag coefficient(μ is the fluid viscosity and R is the particle's hydrodynamic radius), and $\mathbf{F}_{ext}$ is any external force acting on the particle. The fluctuating collisions between the particle and the surrounding fluid molecules are approximated by a stochastic force $\Gamma(\mathbf{t})$ whose correlation function satisfies

$$\langle \Gamma_i(t)\Gamma_j(t')\rangle = \frac{2\gamma kT}{m}\delta_{ij}\,\delta(t-t'), \tag{2.3}$$

with δ_{ij} the Kronecker delta. *Brownian* dynamics is essentially the numerical simulation of the *Langevin* equation.

2.2 Molecular Dynamics

Molecular dynamics(MD) simulation incorporates *Newtonian* mechanics to the individual atom and models the atom-atom interaction by *Lennard-Jones* potential[67]:

$$U_{LJ}(r) = 4\epsilon\left[d_{ij}\left(\frac{\sigma}{r}\right)^{12} - c_{ij}\left(\frac{\sigma}{r}\right)^{6}\right], \quad r \le r_c$$

with σ the characteristic length scale and ϵ the potential depth. r is the atom-atom distance. The potential is cut off at distance r_c. c_{ij} and d_{ij} are the interaction coefficients between species i and j. Here we fix $d_{ij} = 1.0$ to retain the repulsive forces between atoms but tune c_{ij} to see the wettability effect. Polyatomic molecules

are modeled by a chain of atoms bounded by a finitely extensible nonlinear elastic("FENE") potential between neighboring atoms[68]. The bounding force takes the form

$$\mathbf{F}_{FENE} = -\frac{k_F \mathbf{r}}{1 - r^2/r_0^2},$$

where k_F is the strength of the force and r_0 is the upper limit of the bound length. Solid(wall) atoms are kept in their equilibrium positions by a spring force with the spring constant $k_s = m_w = 100 m_l$. Solid atom mass m_w is chosen to be much heavier than the liquid atom mass m_l. The calculations are performed by standard MD methods, including a layered linked-cell list[69], a predictor-corrector algorithm and a Nosé-Hoover thermostat[70] which fixes the system's temperature. To avoid singularities in computation, the equation of translational and rotational motion of rigid particles is described in terms of quaternion variables[71]. Depending on the geometry of the system, periodic boundary conditions may be applied to one or more dimensions.

2.3 2D Ewald Summation

The implementation of electrostatic(Coulomb) interactions is nontrivial in MD. In order to correctly account for the periodic images of the charged particles, one has to use Ewald summation in the calculation[72]. Generally, the naive summation of the Coulomb potential in a periodic system,

$$U_C = \frac{1}{2}\frac{1}{4\pi\epsilon}\sum_{l_x,l_z}\sum_{i=1}^{N}\sum_{j=1}^{N}{}' \frac{q_i q_j}{|\mathbf{r}_i - \mathbf{r}_j + l_x\mathbf{L}_x + l_z\mathbf{L}_z|}$$

is only conditionally convergent. Here, $\mathbf{L}_x$ and $\mathbf{L}_z$ are the lattice vectors, $\mathbf{r}_i$ and $\mathbf{r}_j$ are the intra-cell position vectors of the i'th and j'th particle respectively, N is the number of charges in the primary simulation cell. and the prime notation means $j \neq i$.

In the 2D Ewald summation method [72, 73, 74], the potential is rewritten as a sum:

$$U_C = U^r + U^k_{\mathbf{k}\neq 0} + U^k_{\mathbf{k}=0} + U^s.$$

The real space sum U^r is

$$U^r = \frac{1}{2}\frac{1}{4\pi\epsilon}\sum_{l_x,l_z}\sum_{i=1}^{N}\sum_{j=1}^{N}{}' \frac{q_i q_j}{|\mathbf{r}_{ij} + l_x\mathbf{L}_x + l_z\mathbf{L}_z|} erfc(\alpha|\mathbf{r}_{ij} + l_x\mathbf{L}_x + l_z\mathbf{L}_z|),$$

where $\mathbf{r}_{ij}$=$\mathbf{r}_i$−$\mathbf{r}_j$ the relative position vector and α is a constant controlling the width of the Gaussian distribution of screening charges. $U^k_{\mathbf{k}\neq 0}$ and $U^k_{\mathbf{k}=0}$ are the contributions from reciprocal space sums with and without $\mathbf{k}$=0 term:

$$\begin{aligned} U^k_{\mathbf{k}\neq 0} =& \frac{1}{4\pi\epsilon}\frac{\pi}{2|\mathbf{L}_x\times\mathbf{L}_z|}\sum_{\mathbf{k}\neq 0}\sum_{i=1}^{N}\sum_{j=1}^{N}{}' q_i q_j \frac{cos(\mathbf{k}\cdot\mathbf{r}'_{ij})}{|\mathbf{k}|} \\ & \left[e^{|\mathbf{k}|y_{ij}} erfc\left(\frac{|\mathbf{k}|}{2\alpha} + \alpha y_{ij}\right) + e^{-|\mathbf{k}|y_{ij}} erfc\left(\frac{|\mathbf{k}|}{2\alpha} - \alpha y_{ij}\right)\right], \end{aligned}$$

$$U^k_{\mathbf{k}=0} = -\frac{1}{4\pi\epsilon}\frac{1}{|\mathbf{L}_x\times\mathbf{L}_z|}\sum_{i=1}^{N}\sum_{j=1}^{N}{}' q_i q_j \left\{\frac{\sqrt{\pi}}{\alpha} e^{-(\alpha y_{ij})^2} + \pi y_{ij} erf(\alpha y_{ij})\right\}$$

and U^s is the self energy

$$U^s = -\frac{1}{4\pi\epsilon}\frac{\alpha}{\sqrt{\pi}}\sum_{i=1}^{N} q_i^2.$$

The force is obtained by differentiating with respect to $\mathbf{r}_i$.

Since the functional form of the force is complex, various approximate formulas are commonly used to reduce the computational load [73, 74, 75, 76]. As with the van der Waals forces above, we prefer to use the exact expression but construct a look-up table in advance and interpolate during the simulation to perform a fast calculation of the Coulomb forces. For the forces arising from $U^k_{\mathbf{k}\neq 0}$:

$$\begin{aligned} (F^k_{\mathbf{k}\neq 0})_\lambda =& \frac{1}{4\pi\epsilon}\frac{q_i 2\pi}{|\mathbf{L}_x\times\mathbf{L}_z|}\sum_{\mathbf{k}\neq 0}\sum_{j=1}^{N} q_j \frac{\mathbf{k}\cdot\mathbf{r}'_{ij}}{|\mathbf{k}|}(\mathbf{k})_\lambda \times \\ & \left[e^{|\mathbf{k}|y_{ij}} erfc\left(\frac{|\mathbf{k}|}{2\alpha} + \alpha y_{ij}\right) + e^{-|\mathbf{k}|y_{ij}} erfc\left(\frac{|\mathbf{k}|}{2\alpha} - \alpha y_{ij}\right)\right], (\lambda = x, z) \end{aligned}$$

we build the table of $\mathbf{f}^e_\lambda(\mathbf{r}_{ij})$ which is a function of relative position $\mathbf{r}_{ij}$:

$$\mathbf{f}^e_\lambda(\mathbf{r}_{ij}) = \sum_{\mathbf{k}\neq 0} \frac{\mathbf{k}\cdot\mathbf{r}'}{|\mathbf{k}|}(\mathbf{k})_\lambda \times \left[e^{|\mathbf{k}|y_{ij}} erfc\left(\frac{|\mathbf{k}|}{2\alpha} + \alpha y_{ij}\right) + e^{-|\mathbf{k}|y_{ij}} erfc\left(\frac{|\mathbf{k}|}{2\alpha} - \alpha y_{ij}\right)\right]$$

and the x and z forces can be evaluated from

$$(F^k_{\mathbf{k}\neq 0})_\lambda = \frac{1}{4\pi\epsilon}\frac{q_i 2\pi}{|\mathbf{L}_x \times \mathbf{L}_z|}\sum_{j=1}^{N} q_j \mathbf{f}^e_\lambda(\mathbf{r}_{ij}). \tag{2.4}$$

For y-force

$$\begin{aligned}(F^k_{\mathbf{k}\neq 0})_y =& \frac{1}{4\pi\epsilon}\frac{q_i 2\pi}{|\mathbf{L}_x \times \mathbf{L}_z|}\sum_{\mathbf{k}\neq 0}\sum_{j=1}^{N} q_j \cos(\mathbf{k}\cdot\mathbf{r}'_{ij})\times \\ & [e^{|\mathbf{k}|y_{ij}} erfc\left(\frac{|\mathbf{k}|}{2\alpha} + \alpha y_{ij}\right) + e^{-|\mathbf{k}|y_{ij}} erfc\left(\frac{|\mathbf{k}|}{2\alpha} - \alpha y_{ij}\right) \\ & - \frac{2\alpha}{\sqrt{\pi}}\frac{1}{|\mathbf{k}|} \times \left\{ \exp\left[-|\mathbf{k}|y_{ij} - \left(\frac{|\mathbf{k}|}{2\alpha} - \alpha y_{ij}\right)^2\right] + \exp\left[|\mathbf{k}|y_{ij} - \left(\frac{|\mathbf{k}|}{2\alpha} + \alpha y_{ij}\right)^2\right]\right\}],\end{aligned}$$

Introducing a function of relative position $\mathbf{r}_{ij}$:

$$\begin{aligned}\mathbf{f}^e_y(\mathbf{r}_{ij}) =& \sum_{\mathbf{k}\neq 0} \cos(\mathbf{k}\cdot\mathbf{r}'_{ij}) \times [e^{|\mathbf{k}|y_{ij}} erfc\left(\frac{|\mathbf{k}|}{2\alpha} + \alpha y_{ij}\right) + e^{-|\mathbf{k}|y_{ij}} erfc\left(\frac{|\mathbf{k}|}{2\alpha} - \alpha y_{ij}\right) \\ & - \frac{2\alpha}{\sqrt{\pi}}\frac{1}{|\mathbf{k}|} \times \left\{ \exp\left[-|\mathbf{k}|y_{ij} - \left(\frac{|\mathbf{k}|}{2\alpha} - \alpha y_{ij}\right)^2\right] + \exp\left[|\mathbf{k}|y_{ij} - \left(\frac{|\mathbf{k}|}{2\alpha} + \alpha y_{ij}\right)^2\right]\right\}],\end{aligned}$$

the y-force becomes

$$(F^k_{\mathbf{k}\neq 0})_y = \frac{1}{4\pi\epsilon}\frac{q_i 2\pi}{|\mathbf{L}_x \times \mathbf{L}_z|}\sum_{j=1}^{N} q_j \mathbf{f}^e_y(\mathbf{r}_{ij}). \tag{2.5}$$

Before the simulation, the reciprocal space summations are carried out for $\mathbf{f}^e_\lambda(\mathbf{r}_{ij})$ and $\mathbf{f}^e_y(\mathbf{r}_{ij})$ on a spatial lattice and the results stored in a table. During the simulation, an interpolation is used for each needed value of $\mathbf{r}_{ij}$, leading to an efficient and accurate evaluation of the forces.

2.4 Lattice Boltzmann Method

Unlike the traditional CFD(Computational Fluid Dynamics) methods, Lattice Boltzmann method("LB") models the fluid by fictive particles which perform consecutive propagation and collision processes over a discrete lattice mesh[77]. LB method is essentially equivalent to the Navier-Stokes equations. In order to model two-phase flows in LB one has to incorporate intermolecular interaction forces into the governing equations for the particle distribution functions. Here we employ the scheme developed by Lee and Liu [78, 79] using a scalar order parameter C, which satisfies the convective Cahn-Hilliard equation $\partial_t C + \nabla \cdot (\mathbf{u}C) = M\nabla^2\mu$[80], involving an adjustable mobility M and a chemical potential μ. The local density is determined by C in a linear way:

$$\rho = C\rho_1 + (1 - C)\rho_2,$$

with the bulk densities of the two phases ρ_1 and ρ_2. C is given by the gradient of a free energy density

$$\Psi = \int_V \left[E_0(C) + \frac{\kappa}{2}|\nabla C|^2 \right] dV + \int_S \left[\phi_0 - \phi_1 C_s + \phi_2 C_s^2 - \phi_3 C_s^3 + ... \right] dS. \qquad (2.6)$$

involving a bulk free energy $E_0(C) = \beta C^2(C-1)^2$, where β is a constant, a gradient term whose coefficient κ controls the surface tension and interfacial thickness, and surface terms which control the solid-liquid interactions, involving the the surface concentration C_s. The liquid/vapor interface profile is found by minimization of the free energy, with appropriate boundary conditions at a solid surface. The discrete Boltzmann equation governing the transport of the mixture density and momentum of the incompressible binary fluids is given by [79]:

$$\frac{Df_\alpha}{Dt} = \left(\frac{\partial}{\partial t} + \mathbf{e}_\alpha \right) f_\alpha = -\frac{1}{\lambda}(f_\alpha - f_\alpha^{eq}) + \frac{1}{c_s^2}(\mathbf{e}_\alpha - \mathbf{u}) \cdot \mathbf{F}\Gamma_\alpha,$$

where f_α is the particle distribution function, $\mathbf{e}_\alpha$ is the microscopic particle velocity in the α-direction, ρ is the density, c_s is the sound speed, λ is the relaxation time and $\mathbf{F}$ is the intermolecular force which satisfies

$$\mathbf{F} = \nabla\rho c_s^2 - (\nabla p - C\nabla\mu),$$

with the dynamics pressure p. By numerically solving the above Boltzmann equation on a discrete spatial and temporal lattice, one can simulate any binary fluid problem.

The LB method is validated by simulating a liquid drop impacting solid surfaces. We first test the resolution issue. We use a *D2Q9* lattice for a 2D grid and find that the drop spreading dynamics becomes stable when the resolution reaches 135 × 135. Next we compare our LB calculations to the benchmark results. For a 3D calculation, we use a 135 × 135 × 112 computational domain for a $D3Q27$ lattice. The boundaries are all symmetric except at the solid surface where we impose a boundary condition introduced by Liu and Lee [81]. The impact is described by three independent dimensionless numbers, the contact angle (θ), Weber number (We), and either the Ohnesorge number (Oh) or the Reynolds number (Re), defined as follows:

$$We = \frac{\rho {u_0}^2 D_0}{\sigma} \quad \text{and} \quad Oh = \frac{\eta}{\sqrt{\rho\sigma D_0}} \quad \text{or} \quad Re = \frac{\sqrt{We}}{Oh} \tag{2.7}$$

where u_0 is the drop impact speed, D_0 is the drop diameter prior to impact, and η and ρ are the liquid's viscosity and density. (Note that in the previous paper [46], Re and We are defined differently, using the drop radius instead of the diameter.) The maximum spreading factor, defined as $\xi_{max} = R_{max}/R_0$, measured for $\theta = 180°$, $Oh = 0.002$ and Weber number ranging from 8 to 90, is found consistent with the experimental data. The validations are shown in Fig. 2.1.

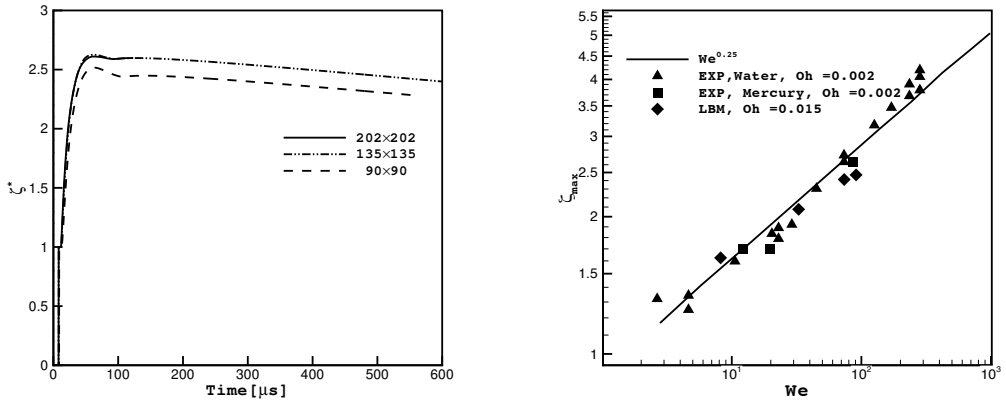

Figure 2.1 : LB validation. (Left) Mesh dependency results: spreading ratio *vs.* time for the three resolutions indicated. (Right) Maximum diameter of the spreading drop, normalized by the drop radius, as a function of the Weber number. The solid line indicates slope 1/4.

Chapter 3

Nano Particles Transport By Flow Past Patterned Surfaces

In this chapter we focus on the transport dynamics of nano particles by flow past a stripe-patterned surface. Firstly we work out the formalism of the particle-substrate interaction. Next, we use MD method to look at how point and finite sized particles interact with the substrate in presence or absence of the background flow. Lastly we use continuum theory to investigate the transport of macro scale particles by flow past the same type of substrate.

3.1 Model Description

We consider a pressure-driven flow in a three-dimensional rectangular channel bounded on two opposing sides by atomistic walls, with periodic boundaries in the other two directions. One bounding surface (the "bottom") has a periodic array of two stripes of equal width with different wettability, shown in Fig. 3.1, while the opposite ("top") surface has uniform interactions. The normal to the two walls is along the y-direction while the flow is driven by a body force parallel to the x-z plane. The underlying idea is that particles flowing over an array of strongly attracting stripes will be deflected by their attraction to the surface, to a degree that depends on particle characteristics, leading to different average trajectories for particles of different type. Referring to Fig 3.1, the particles see an alternating attractive and repulsive potential landscape in the x-direction, arising from the surface. Since the particles preferentially occupy

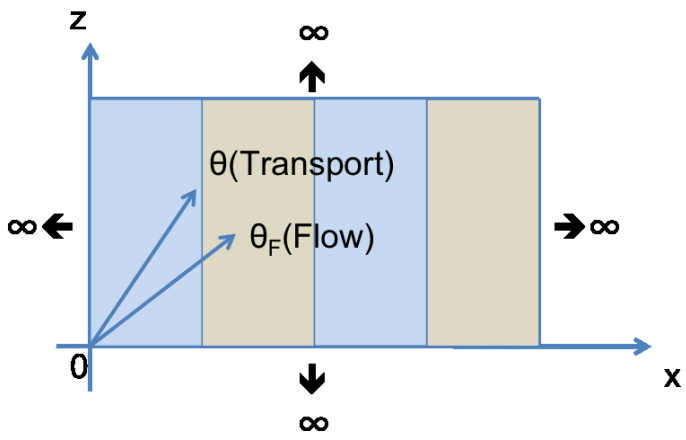

Figure 3.1 : Geometry of the gradient surface method. Particles flow past a solid surface containing alternating regions which do or do not attract them strongly. In response, the particles move at an orientation angle θ which differs from the orientation θ_F of the underlying fluid flow.

the regions above the attracting stripes, any motion away from the stripes along x is discouraged which reduces the transport in that direction. In the z-direction parallel to the stripes, however, there is no such spatial preference and particles advect more freely. The x-velocity is therefore reduced while the z-velocity is unaffected, and we expect $\theta > \theta_F$. Particles of different radii (or suitably different physical properties) will interact in different ways with the patterned wall and a difference in the migration angles is expected. In the laboratory, instead of periodicity one would have a relatively large region of x-z plane, and even a small difference in average trajectory angle will eventually drive different particles to different spatial regions where they may be selectively collected.

3.2 Particle Interacts With Patterned Substrate

We consider flow through a channel bounded by atomistic solid walls, where one "bottom" or "substrate" wall is heterogeneous with a striped pattern of alternating attractive and repulsive regions. The other "top" wall serves to confine the fluid and suspended particles, and is taken to be homogeneous and repulsive for simplicity. The calculations occur in a primary computation box, illustrated in Fig. 3.2, which is periodically replicated in the x and z directions. We assume that the interaction of a fluid or particle atom with a wall is given by the sum of the individual atom-atom potentials. The wall atoms near the solid-liquid interface are responsible for the wall's atomic structure, and produce the corrugated potential seen by fluid atoms near the solid, and these are treated as distinct (tethered) atoms in the simulations. However, the atoms further in the interior of the wall are never very close to fluid atoms, and it is a reasonable approximation to replace the sum of their individual contributions by an integral, weighted by the wall atom density. In practice, for the bottom wall we retain the two layers of wall atoms closest to the fluids explicitly, and the remainder of the wall is replaced by a half-space of atoms. Since the top wall serves only for confinement, it suffices to use just the explicit atomic layers there.

The interaction potential between a fluid or solid atom at position $\vec{r}$ and a wall atom at position $\vec{r}_w$ is then

$$U_{wp}(\vec{r}_w, \vec{r}) = 4\left[\frac{D(\vec{r}_w)}{|\vec{r} - \vec{r}_w|^{12}} - \frac{C(\vec{r}_w)}{|\vec{r} - \vec{r}_w|^{6}}\right] \tag{3.1}$$

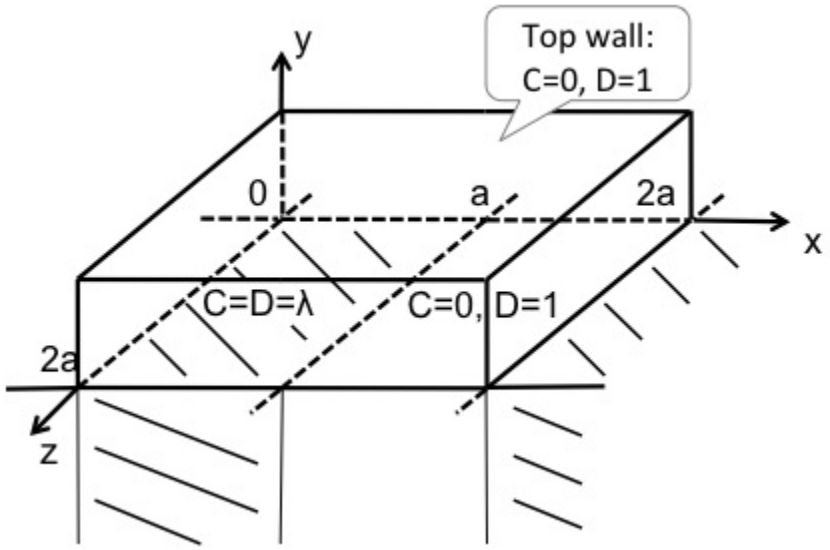

Figure 3.2 : Geometry of the computation box: fluid flows parallel to the x-z plane, confined between a uniform and repulsive top wall and a bottom wall divided equally into attractive and repulsive regions. The box repeats periodically in the x and z directions. The LJ coefficients C and D for wall-particle interactions are as indicated, where the parameter λ controls the wall attraction strength.

where $D(\vec{r}_w)$ and $C(\vec{r}_w)$ are periodic functions

$$\begin{aligned} D(\vec{r}_w) &= \begin{cases} \lambda, & 2na < x_w < (2n+1)a \\ 1, & (2n-1)a < x_w < 2na \end{cases} \\ C(\vec{r}_w) &= \begin{cases} \lambda, & 2na < x_w < (2n+1)a \\ 0, & (2n-1)a < x_w < 2na \end{cases} \end{aligned} \tag{3.2}$$

where a is the the width of a single wall stripe and n runs over all positive and negative integers. As illustrated in Fig. 3.2, we assume that the bottom wall is composed of adjoining semi-infinite slabs of material, so that $\vec{r}_w$ runs over all values of z and all $y \leq 0$. (A simpler model would have a few layers of alternating stripes atop a uniform substrate, but such a weaker interaction would be less effective in separation.) The two stripes will be referred to below as attractive ($C = \lambda$) and standard or repulsive

($C = 0$), respectively. The parameter λ will range from the reference value 1.0 to a strongly-attracting wall value of 8.0. This choice will be employed for the bottom wall in the simulations, while the top wall will be treated as standard and assigned the reference values for C and D.

The interaction between a fluid or particle atom at $\vec{r} = (x_0, y_0, 0)$ and the bottom wall integrals of the form

$$I = \int_{-\infty}^{\infty} dz \int_{-\infty}^{0} dy \int_{-\infty}^{-\infty} dx\, C(x)[z^2 + (y - y_0)^2 + (x - x_0)^2]^{-\frac{m}{2}}$$

where

$$C(x) = \begin{cases} c_1, & 2n < x < 2n + 1 \\ c_2, & 2n - 1 < x < 2n \end{cases}$$

Note that the interaction is translationally invariant in z, and for the moment we set $a = 1$ for ease of writing but restore a at the end of this section. The values $m = 6$ and 12 occur in the attractive and repulsive terms, respectively, and $n = 0, \pm 1, \pm 2, ...$

Although the integral I cannot be computed analytically, it can be expressed as a power series from which we construct a look-up table for use in the numerical simulations. The integral over z can be done easily to give

$$I = \frac{\sqrt{\pi}\Gamma(\frac{m-1}{2})}{\Gamma(\frac{m}{2})} \int_{-\infty}^{\infty} dx \int_{y_0}^{\infty} dy C(x + x_0)(x^2 + y^2)^{-\frac{m-1}{2}}.$$

Defining

$$f(x) = \frac{\sqrt{\pi}\Gamma(\frac{m-1}{2})}{\Gamma(\frac{m}{2})} \int_{y_0}^{\infty} dy (x^2 + y^2)^{-\frac{m-1}{2}} \qquad \text{and} \qquad g(x) = \int_0^x f(x')dx',$$

and writing $g(+\infty) = g_\infty$, $g(-\infty) = -g_\infty$, one has:

$$I = \int_{-\infty}^{\infty} dx C(x + x_0) f(x).$$

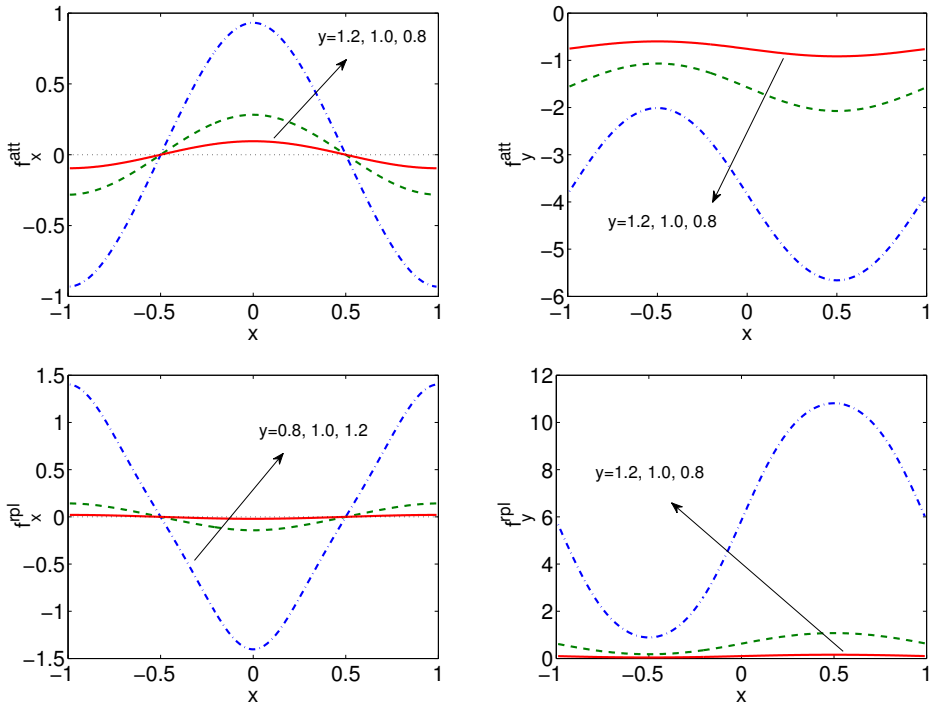

Figure 3.3 : Typical variation of forces near the bottom wall. for $c_1 = 2.0$, $c_2 = 0.0$. The solid, dashed and dash-dotted curves represent $y = 1.2$, $y = 1.0$ and $y = 0.8$ respectively. The x-force vanishes at the center of stripe and is maximum at the stripe boundaries, while the y-force takes its maximal values at the center of the stripe.

which can be integrated by parts to give

$$\begin{aligned} I =& C(x_0-)[g(0-)+g_\infty] - C(x_0+)[g(0+)-g_\infty] \\ & - (C_1 - C_2)\left[\sum_{n<x_0}(-1)^n[g(n-x_0)+g] - \sum_{n>x_0}(-1)^n[g(n-x_0)-g]\right]. \end{aligned}$$

The derivatives of I give the force components:

$$f_x^m = -\frac{\partial I}{\partial x_0} = -\int_{-\infty}^{\infty} dx\, C'(x+x_0)f(x) = -(C_1-C_2)\sum_n (-1)^n f(n-x_0), \quad (3.3)$$

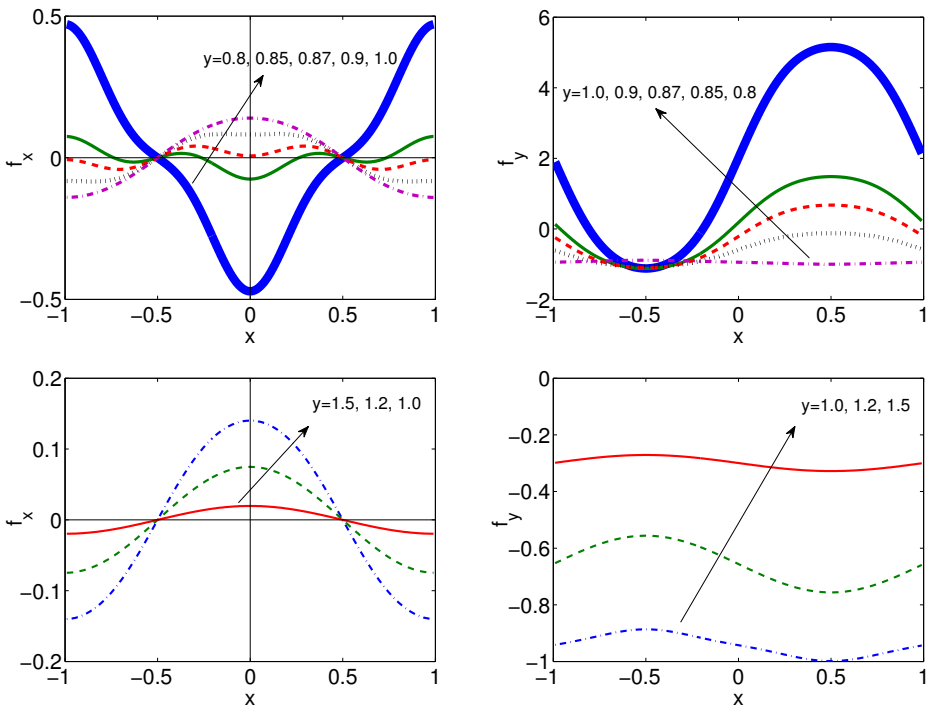

Figure 3.4 : Competition between attractive and repulsive forces near the bottom wall. Far from the wall, the x-force is small and attractive towards the stripe boundaries, but reverses on closer approach. The y-force similarly reverses in sign on approach to the wall.

$$
\begin{aligned}
f_y^m = -\frac{\partial I}{\partial y_0} = -\int_{-\infty}^{\infty} dx\, C(x+x_0)h(x) = \\
-J_\infty[C(x_0-)+C(x_0+)] + (C_1-C_2)\sum_{n<x_0}(-1)^n[J(n-x_0)+J_\infty] \\
+(C_1-C_2)\sum_{n>x_0}[J(n-x_0)-J_\infty]
\end{aligned}
\tag{3.4}
$$

where

$$
h(x) = \frac{\partial f(x)}{\partial y_0} = -\frac{\sqrt{\pi}\Gamma(\frac{m-1}{2})}{\Gamma(\frac{m}{2})}(x^2+y_0^2)^{-\frac{m-1}{2}} \qquad \text{and} \qquad J(x) = \int_0^x h(x')dx'
$$

Note that $J(x)$ is an odd function with limits $J(\pm\infty) = \pm J_\infty$.

It is useful to define an intermediate function $K_m(x,y)$ via

$$\frac{\pi}{m-2}\frac{K_m(x,y)}{x^{m-2}} = \frac{\sqrt{\pi}\Gamma(\frac{m-1}{2})}{\Gamma(\frac{m}{2})}\int_y^\infty dy'(x^2+y'^2)^{-\frac{m-1}{2}}. \tag{3.5}$$

Note that $K_m(x,y)$ is a function only of the ratio x/y, and in particular

$$K_6(x,y) = \frac{3x^2y+2y^3}{2(x^2+y^2)^{3/2}},$$

$$K_{12}(x,y) = \frac{315x^8y+840x^6y^3+1008x^4y^5+576x^2y^7+128y^9}{128(x^2+y^2)^{9/2}}.$$

If we define

$$t_m(x_0,y_0) = \sum_{n=-\infty}^{\infty}(-1)^n\frac{1-K_m(n-x_0,y_0)}{(m-2)(n-x_0)^{m-2}}, \tag{3.6}$$

then from Eq. (3.3) the x-component of the force can be written as

$$f_x^m = -\pi(c_1-c_2)t_m.$$

Likewise, defining

$$s_m(x_0,y_0) = \frac{1}{m-2}\left[\sum_{n<x_0}(-1)^n(-K_m(y_0,n-x_0)-1)+\sum_{n>x_0}(-1)^n(-K_m(y_0,n-x_0)+1)\right], \tag{3.7}$$

from Eq. (3.4) the y-component of the force due to an mth power potential is:

$$f_y^m = \frac{\pi}{y_0^{m-2}}\left[\frac{2C(x_0)}{m-2}+(c_1-c_2)s_m\right].$$

Finally, we restore the width a of the stripes by rescaling the variables in the starting integral I, leading to

$$f_x^m = -\pi(c_1-c_2)t_m(\frac{x_0}{a},\frac{y_0}{a}), \tag{3.8}$$

$$f_y^m = \frac{\pi}{y_0^{m-2}}\left[\frac{2\tilde{C}(x_0)}{m-2}+(c_1-c_2)s_m(\frac{x_a}{a},\frac{y_0}{a})\right], \tag{3.9}$$

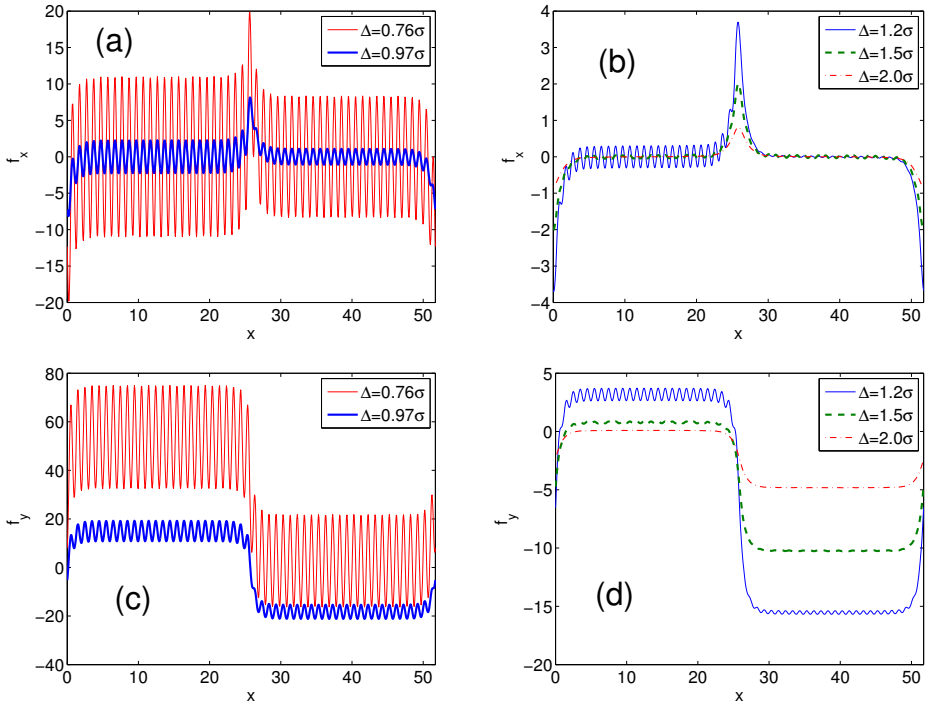

Figure 3.5 : Complete force field at various distances from the wall, combining discrete wall atom and continuum wall interactions. (a) x-force near the wall, (b) x-force away from wall, (c) y-force near the wall and (d) y-force away from wall.

where

$$\tilde{C}(x) \;=\; \begin{cases} c_1, & 2na < x < (2n+1)a \\ c_2, & (2n-1)a < x < 2na \end{cases} \tag{3.10}$$

The full LJ potential arising from a continuum wall is the difference of the $m = 12$ and $m = 6$ results; the individual terms in the force are shown in Figs. 3.3 and the sum in Figs. 3.4. Unsurprisingly, the force is strong only in the vicinity of the wall. When the particle is near the wall, the repulsive ($m = 12$) part of the force increases rapidly, but at intermediate and larger distances, the attractive force decays much more slowly and dominates the repulsive force. The net force behaves roughly as y_0^{-10} due to the r^{-12} repulsive potential when near the wall, and as y_0^{-4} at larger distances.

The complete force field acting on any atom is the sum of the continuum contribution above and the two-body potentials of the explicit wall atoms, shown in Fig. 3.2. The principal features are a stronger force near the wall and a rapid oscillation on the scale of the wall atom spacing. The y-component of the force is, as expected strongly attractive towards the wetting region, while the x-component force peaks at the stripe boundaries and tends to push the particles towards the wetting region. In the subsequent discussion, we characterize the non-uniform distribution of particles resulting from the surface interactions by the partition coefficient P, defined as the probability of finding a particle above the wetting stripe.

3.3 Simulation Results

3.3.1 Point Particle Without Flow

In the simplest case, the fluid and the suspended particles are individual atoms, which amounts to a two-component liquid with comparable sizes for the molecular components. The advantage of this assumption is that smaller particles have a larger diffusivity which leads to faster simulations, while retaining the essential physics of separation. In a simulation of a monatomic liquid in a patterned channel, a fraction ϕ of fluid atoms are randomly chosen to be point "particles" subject to modified particle-wall interactions while the remaining "solvent" atoms interact with a uniform substrate. The key quantity of interest is the partition coefficient P, defined as the fraction of particles located above the wetting stripe.

The calculations are performed using standard MD methods, including a layered linked-cell list, a predictor-corrector algorithm with a time step of 0.005τ, and a Nosé-Hoover thermostat which fixes the temperature at $k_BT = 1.0\epsilon$. The system contains

13,824 liquid and particle atoms at an overall density $0.8\sigma^{-3}$ and 2,704 (explicit) atoms in each wall, in a box of dimensions $(X, Y, Z) = (41.04, 13.68, 41.04)\sigma$. Initially, the particles are uniformly dispersed in the liquid, and during a 100τ equilibration period the enhanced wall attraction is turned off ($\lambda = 1$ so as to produce an unbiased initial state. The wall interactions are then restored, and the simulation is run until the particle distribution reaches a steady state; the time required varies from $4{,}500\,\tau$ to $7{,}500\,\tau$, depending on the interactions used. We consider particle concentrations of 1, 2, 5 and 10%, and attractive wall strengths λ=2, 4, 6 and 8, and in each case we average over 10 realizations. All interactions *except* the enhanced wetting interactions between the particles and the substrate wetting stripe are cut off at a separation $r_c = 2.5\sigma$, at which point the resulting force is quite weak. However, the interaction between the particles and the attractive parts of the bottom wall, including both the explicit atoms and the half space below it, has no cutoff. This choice is made to maximize the effect of the stripes on the particles while speeding up the calculation by omitting parts of the interaction inessential for continuum fluid behavior.

At equilibrium, one expects the particles to accumulate near the attractive (wetting) stripe, forming a roughly uniform layer, while depleting the regions near the other parts of the walls and the middle of the box. The simulation results are in agreement with this reasoning up to a point: the complete set of final states for the range of ϕ and λ considered here is shown in Fig. 3.6. We see that there is always an accumulation near the wetting stripes, to an extent that increases with both λ and ϕ, but because there are a fixed number of particles each occupying a finite volume, they may form either filled or partially filled layers, depending on the attraction strength and the number available. The region very close to the non-attractive walls where the interaction is purely short-range repulsion always remains depleted of particles,

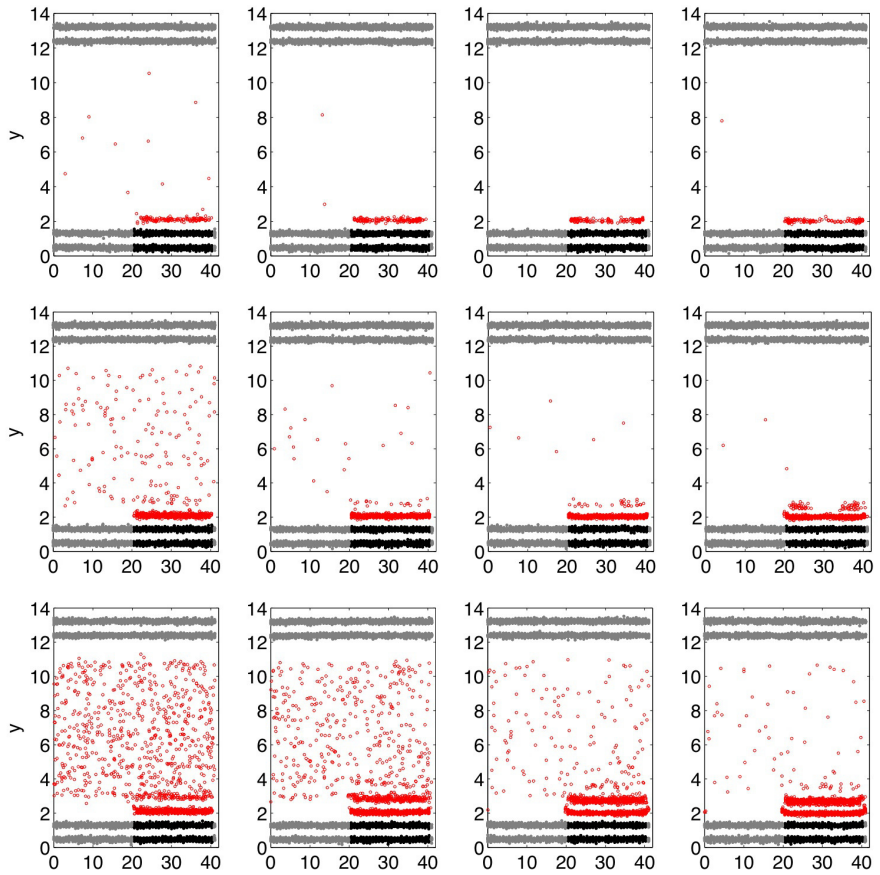

Figure 3.6 : Point Particle Model: Final configurations at $7500\,\tau$ for various parameter sets. From top to bottom: ϕ= 0.01, 0.05 and 0.1; From left to Right: λ = 2.0, 4.0, 6.0 and 8.0.

and furthermore increasing λ tends to draw particles closer to the attractive stripe.

The time evolution of the particle distribution is indicated quantitatively in Fig. 3.7, which shows the probability distribution function of distance from the attractive wall time at different times in the course of a simulation run, separately for the particles above the attracting and repulsive parts of the bottom wall. Each plot represents an average over a $450\,\tau$ time interval. During the equilibration phase before the wettability is turned on the usual density oscillations are seen at both walls; in this time

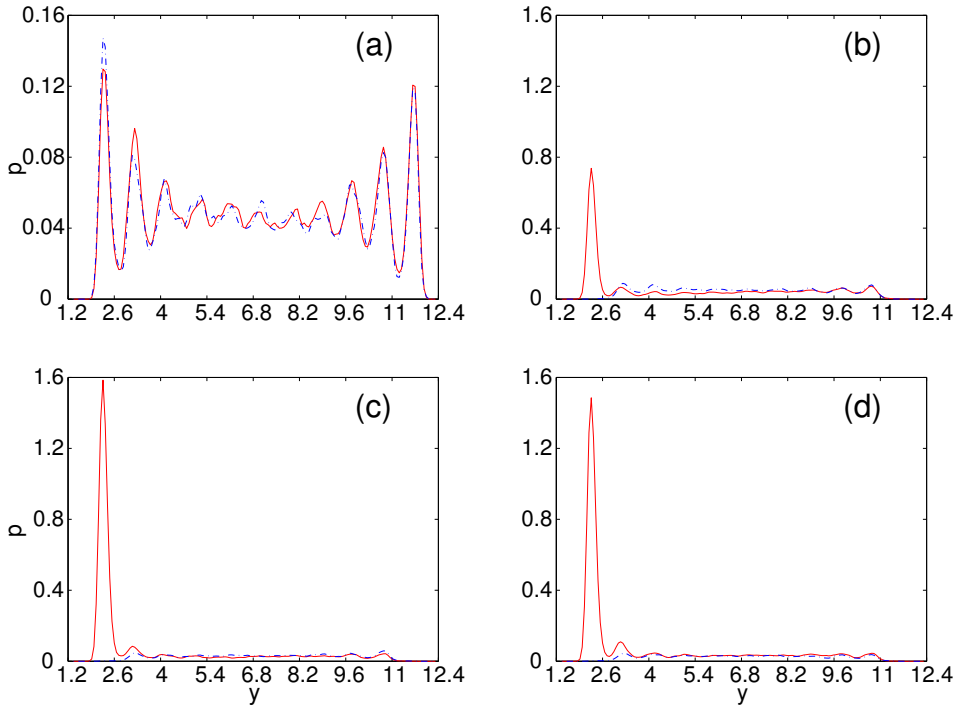

Figure 3.7 : Probability distribution of particle's distance from the wall, averaged over various time intervals, for $\phi = 0.02$ and $\lambda = 1.5$. (a) Before and (b) just after turning on the wetting interactions, (c) in the middle of the run, and (d) at equilibrium. Full (red) and dashed (blue) lines are the distributions above the wetting and nonwetting stripes, respectively.

interval the particles are indistinguishable from the solvent atoms, and a confined and dense liquid always exhibits density oscillations near a planar wall. At later times the particles in the attracting region are drawn downwards and enhance the peak near the lower wall while depleting the profile elsewhere, in this case leaving so few particles elsewhere that there is no longer any close-packing issue and the systematic density oscillations are replaced by structureless fluctuations. The height of the attractive peak increases with time until about $1500\,\tau$ and then decays to its equilibrium value.

The partition coefficient P is plotted as a function of time in Fig. 3.8 for various

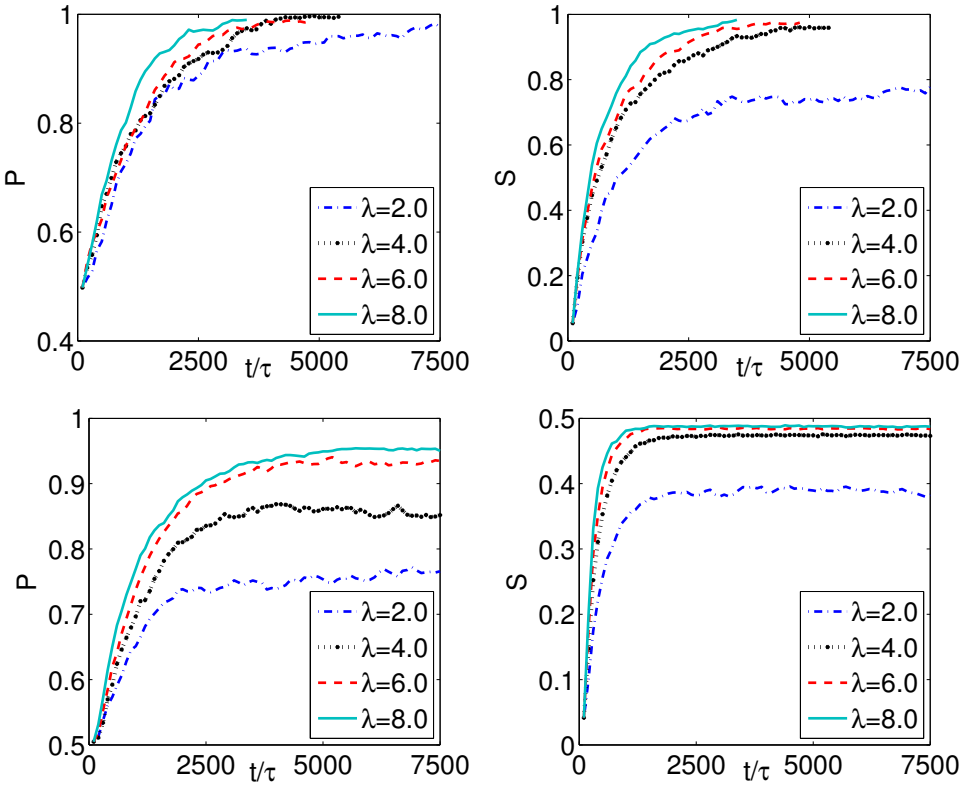

Figure 3.8 : Time dependence of the partition coefficient (left) and the fraction of stuck particles (right), for ϕ= 0.02(top) and 0.1(bottom), for various values of the interaction strength.

particle concentrations. In each case, P starts at the equilibration value 1/2 and then increases with time until a steady state plateau is reached. Naively, one would expect the plateau value to increase monotonically and and the time to reach it to decrease monotonically with λ, but in fact for most cases there is a distinct difference between the results for $\lambda = 2$ and higher values 4, 6 and 8, and little or no significant difference among the three higher values. Evidently. the effect of increasing the attraction strength saturates, which we attribute to the fact that the enhanced attraction is nonetheless weak except very close to its part of the solid wall, and once the first layer

forms this somewhat weak interaction is competing with the strongly fluctuating LJ interactions with the solvent. Similar conclusions follow from evaluating the "stuck fraction" S, defined as the fraction of particles within a distance σ of the attracting solid. Here, the steady-state value is usually below one, because any particle in a second layer at higher ϕ is certainly at a larger distance from the wall, and even particles remaining in the first layer may fluctuate slightly away from the solid. The variation of S with ϕ and λ has the same qualitative features as P does.

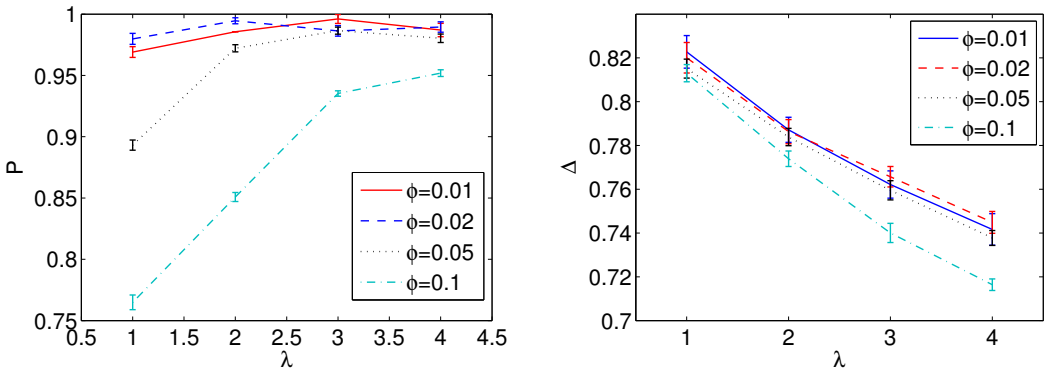

Figure 3.9 : Effects of varying the attraction strength. Left: asymptotic partition coefficient at different concentrations. Right: width of the gap between particles and the attracting solid wall.

The ability of the wall to attract particles in the absence of a flow is summarized in Fig 3.9, which shows the variation of the final state partition coefficient with interaction strength λ, for different concentrations. As mentioned above, except at the lowest concentrations, the accumulation saturates beyond $\lambda = 4$ or so, because the region in which the wall attraction is strong becomes filled with particles. However, further increases in λ do affect the configuration in that the particles draw closer to the solid: the average gap Δ decreases systematically.

3.3.2 Flowing Finite Sized Particles

Our main interest is in the separation of finite-sized particles, which are treated here as a rigid body composed of atoms with fixed relative positions. The MD simulations involve 27,648 fluid and particle atoms and 10,816 wall atoms contained in a box of size $(X, Y, Z) = (51.71, 17.24, 51.71)\sigma$, bounded by top and bottom walls in y-direction and periodic boundaries in x- and z-directions. Roughly 5% of the atoms are used to construct the particles, and the remainder are left as individual fluid (solvent) atoms. Both walls have two layers of explicit atoms, which are tethered to fixed lattice sites by springs. The bottom wall (substrate) is divided into two equal parts, where the right half (wetting stripe) interacts with all particle atoms with a variable interaction coefficient λ, while the left half (nonwetting stripe) and top wall exert a short-distance repulsion of fixed strength. A body force $\vec{g}$ is applied to each fluid atom parallel to the x-z plane at various orientations with respect to the stripe boundaries. Simulations were performed with the following parameters: the particles contain either 7, 33, 81 and 203 atoms, corresponding to radii 1.08, 2.15, 2.64 and 3.88σ, respectively, the body force g ranges from 0.005 to $0.2m\sigma/\tau^2$, and the interaction coefficient λ takes on values 1.0, 1.1, 1.5 and 2.0.

The flow field may be characterized by the Reynolds number, based on the channel width $w \approx 12.9\sigma$ and the average fluid velocity V,

$$Re = \frac{\rho/Vw}{\mu} = \frac{1}{8}\frac{\rho^2}{\mu}\, w^3\, g \tag{3.11}$$

where in the second part of the equation we have substituted the usual expression for average velocity in Poiseuille flow. The viscosity $\mu \approx 2.0$ as obtained from our simulations, so numerically $Re \approx 43g$ and is O(1) in these simulations. The particle

motion is characterized by the Péclet number

$$Pe = \frac{rV}{D} = \frac{\rho g r w^2}{8\mu D} = \frac{3\pi\rho w^2 r^2}{4k_B T}\, g \tag{3.12}$$

where we have again inserted the Poiseuille flow expression for V, and then used the Stokes-Einstein relation for spheres, $D = k_B T/6\pi\mu r$. Numerically, in these simulations $Pe \approx 1255g$ for a particle of radius 2.0.

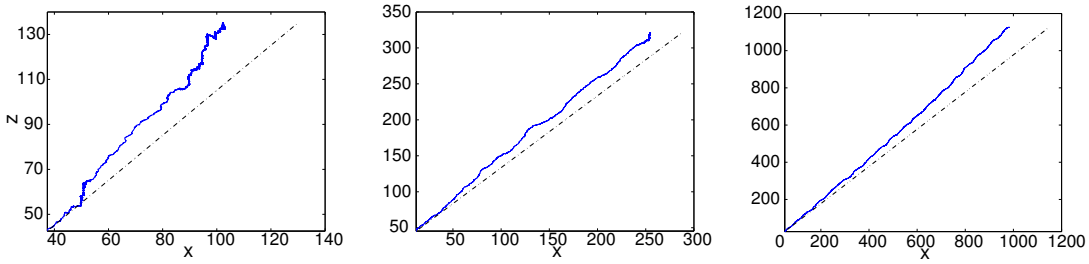

Figure 3.10 : Three examples of typical particles motion for the case $\lambda = 1.5$, $r = 2.15$ and $g = 0.02$ oriented at 45°. The trajectories are the irregular lines and the mean flow direction is the dashed line. From left to right, we see trapping, restrained motion and free motion.

Typical individual particle trajectories are shown in Fig. 3.10 for a particular parameter set. The three cases illustrate a trapped particle which becomes bound to the substrate, a mobile particle whose translational motion is restricted by substrate interactions, and a particle moving almost freely in the center of the channel. In all cases the duration of the trajectory is 15,000 τ. The distinct behaviors are manifest in the time-averaged gap distances between the lowest point of the particle and the mean position of the inner layer of substrate atoms, $\Delta = 0.5$, 1.6 and 5.4σ, respectively. in the three examples. Note the upward jumps in the first trajectory, which occur when the particle crosses the stripe boundary (recall that the periodicity of the pattern is approximately 52σ) and its x-motion is slowed by the substrate interaction. When

the particle is at an intermediate distance from the substrate (middle subgraph), the jumps are less obvious but still visible, while if the particle is far from the substrate (right subgraph), the trajectory simply appears noisy. Not surprisingly, as the particle moves away from the striped pattern its trajectory smoothes and its velocity increases.

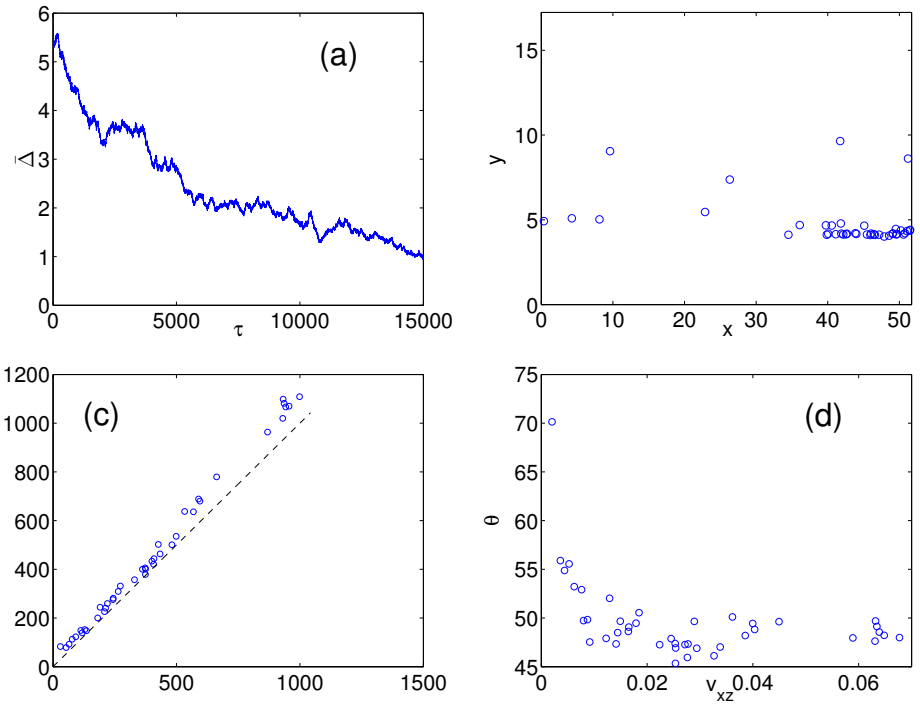

Figure 3.11 : Final configurations for the case $\lambda = 1.5$, $r = 2.0$ and $g = 0.02$ and 45° applied flow. (a) Variation of the average particle-substrate gap with time, (b) Side view of the final configuration, (c) Positions at the end of the simulation in the substrate plane, (d) Trajectory angle *vs.* mean in-plane velocity.

The final state of the same simulation, showing the positions of *all* of the particles, is shown in Fig. 3.11. The x-z plot gives the actual positions in the plane parallel to the stripes, which involves unfolding the trajectories from their periodic images within in the primary simulation box. There is a wide distribution of distances traveled, but a characteristic trajectory deflection is apparent. The x-y plot shows the final

displacement above the substrate plane, in this case in the primary box for simplicity, and we see a group of trapped particles just above the wetting stripe along with mobile ones at larger separations. The time variation of the mean gap Δ between the particles and substrate shows a systematic decay from an initial value corresponding to a uniform distribution to the small asymptotic value when eventually most of the particles are near the wetting stripe and strongly interacting with it. Lastly, the velocity plot shows that the largest deflection angles are associated with low-velocity particles which are probably trapped or diffusing within the attractive stripe, or perhaps colliding with other particles in the same situation. The very highest velocity particles show a smaller but significant deflection, consistent with the trajectory in the left-hand frame of Fig. 3.10. Although these particles are further from the substrate on average they do diffuse in the y-direction, and evidently spend enough time near the wetting stripe for their motion to be affected.

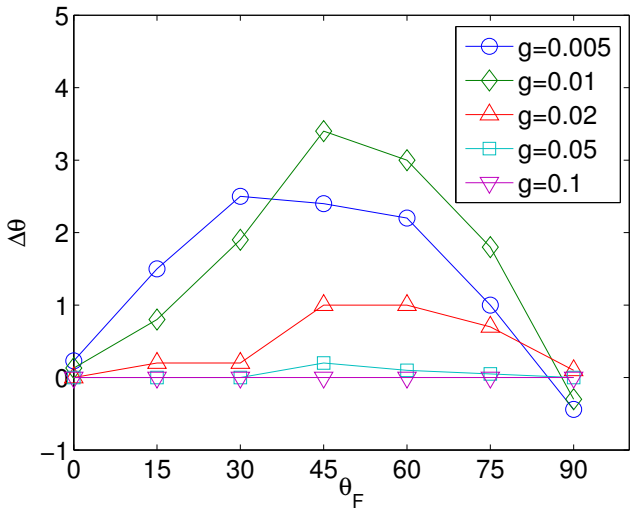

Figure 3.12 : Variation of deflection angle $\Delta\theta$ with imposed pressure gradient angles θ at various pressure gradient g.

Next we address the effects of varying the mean flow direction. As shown in Fig. 3.12, particles transporting with 45° flow have the greatest deflection in general. When the mean flow is either parallel 90° or perpendicular 0° to the stripes the deflection is approximately zero, due to symmetry. Other flow angles produce results intermediate in magnitude, and in the following discussion we focus on 45° flow simulations in order to maximize the deflection.

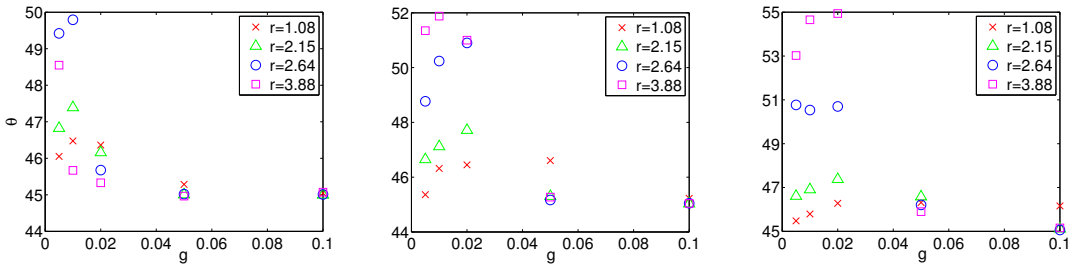

Figure 3.13 : Transport angle θ versus pressure gradient g for particle of different radius. Left to right: λ=1.1, 1.5 and 2.0.

The results for particle deflection are shown in Fig. 3.13, and some obvious trends are apparent. First, the maximum deflection increases with the attraction strength λ, over the range plotted. At still higher values there is little change, because the region just above the wetting stripes where the interaction is strongest eventually becomes saturated with particles, forcing the other particles away into regions where the wall potential is weaker. This observation alone means that it is possible to separate particles based on their chemical properties, specifically the strength of their interaction with the wetting stripes. Secondly, the velocity of the background flow, controlled here by the pressure gradient g, should be intermediate in value for the strongest deflection. At low velocities the particles move slowly and are subject to obstruction by the other particles present, rather than exploring uncovered regions

of substrate which may more readily be approached. This consideration is not an overwhelmingly important one, but does explain the rise in θ seen at the lowest g values. At high flow velocities the deflection drops off to small or negligible values – in this limit the particles are likely to be advected with the flow and the Stokes drag force overcomes the substrate attraction. The effect of the background flow on the particle velocities can be observed in a different format by a scatter plot of average particle speed in the x-z plane *vs.* position y above the substrate, shown in Fig. 3.14. At low g the speed is controlled by molecular diffusion so that low speeds are common and the higher-speed particles are located at any y, but at higher g most particles are moving and the effect of the solvent's parabolic velocity profile is apparent.

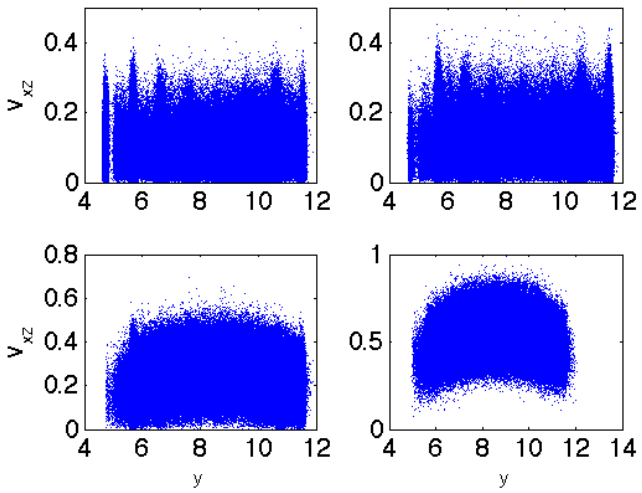

Figure 3.14 : Scatter plot of velocities in the x-z plane against y-position for $\lambda = 1.1$ and $r = 2.64$. Left: $g = 0.01$, right: $g = 0.10$.

The final qualitative result of these simulations is that the deflection angle *is* a function of particle size, so that separation based on particle size alone is possible. Our results do not show a simple monotonic trend however. For the three smaller radii,

at the lower g-values where the deflection angle is largest it increases with particle radius, reflecting a stronger substrate interaction because there is more material to interact with. The largest-sized (r=3.88σ) particle does not fit this pattern; a physical reason is that the interaction has more variation over the extent of a larger particle, which then has regions both more and less attracting to the substrate than a smaller particle, complicating its behavior. (A further technical issue is that we have fewer realizations for the larger particles, because they are more likely to trap a fluid atom between themselves, leading to closer approach and higher interatomic forces and a greater likelihood of a computational error which halts the program.)

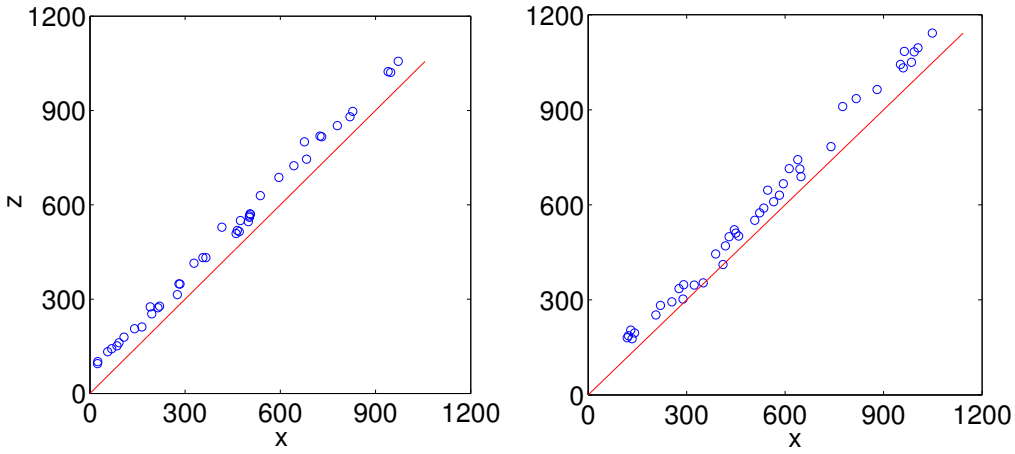

Figure 3.15 : The effect of continuum half-space interactions on particle motion. Final particle positions, Left: with, and Right: without, for a simulation with parameters $r = 2.15$, $\lambda = 1.5$ and $g = 0.02$.

Finally, we provide some *a posteriori* justification for adding a semi-infinite half-space of continuum substrate atoms in addition to the explicit atomic wall layers. Although the interaction with the explicit atoms at the surface of the wall provides the dominant force numerically at any fixed position, the half-space of continuum atoms does have a significant quantitative effect. Visually, in Fig. 3.15, the most

	With	Without	Difference
$\bar{D}_x$	432.0σ	532.8σ	25%
$\bar{D}_y$	-4.4σ	-4.1σ	7%
$\bar{D}_z$	503.1σ	597.0σ	19%
$\bar{\theta}$	49.3°	48.3°	2%

Table 3.1 : Quantitative effects of the continuum half-space interaction. Spatial components of particle mean transport distance and angle with and without the continuum interaction, for $r = 2.15$, $\lambda = 1.5$ and $g = 0.02$.

obvious effect is to trap some particles near their starting points, and produce a more uniform distribution of final positions. Quantitatively, however, Table 3.1 shows a clear difference of as much as 25% in the various components of the mean transport distance. The effect on the transport angle is present but much smaller – 2%, but recall that even a small change in angle leads to a substantial spatial separation over a long enough distance. One might have thought that the half-space interaction would be negligible because the surface layers of explicit wall atoms are much closer to the fluid and particle atoms than the continuum part of the wall. However, the former interaction falls rather rapidly as the inverse sixth power of separation, whereas the latter incorporates an infinite amount of interacting material and has a much slower decay, as the inverse third power, and is effective even in the middle of the channel.

In the simulations just described, the interaction between the particles and the solvent fluid was fixed, at the standard LJ values $C = D = 1$. If this interaction is varied, the influence of the substrate interaction takes on more or less importance and the particle motion changes. In Fig. 3.16 we compare the final positions for a range of particle-fluid interaction If we fix $C = D$, then values smaller than the standard

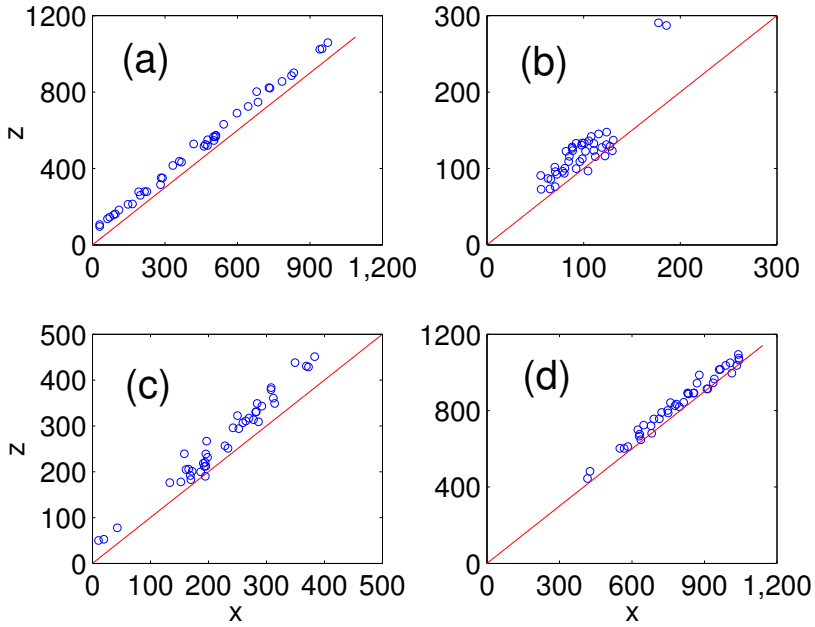

Figure 3.16 : Comparison of the final configurations with different particle-solvent interaction coefficients: (a) $C = 1.0$, $D = 1.0$, (b) $C = 0.0$, $D = 1.0$, (c) $C = 0.5$, $D = 0.5$, and (d) $C = 1.5$, $D = 1.5$.

(1.0) result in less particle motion while values greater than this result in stronger particle advection. If C=0 there is no attraction and the fluid tries to expel particles, resulting in their accumulation at the walls of the box and little transport.

3.3.3 Flowing Charged Particles

The trajectory deflections produced by van der Waals interactions with a substrate are generally small, because this interaction falls off rapidly with distance. In particular, the particles moving near the substrate which experience the strongest forces also have relatively low velocities and are more influenced by molecular diffusion, and may be trapped at an early time before the trajectory develops. To produce a stronger effect,

we turn to longer-ranged Coulomb interactions. There are innumerable possibilities of distributing charges among the atomic species in an MD simulation, and in the following discussion we focus on several specific scenarios in which electric charge is placed on the particles and bounding walls only. In reality, the solvent may be charged as well, leading to a finite screening length for the Coulomb interaction, which could be implemented through a dielectric constant which can reduce the magnitude of the interaction. In most cases we omit this effect, but examine the effect of using the dielectric constant of water in one example below. The particle motion is simulated using the MD methods described in Sec. 2.2, with the new feature that the long-ranged Coulomb interactions from the periodic copies of the primary simulation box are included using Ewald summation methods described in Sec. 2.3.

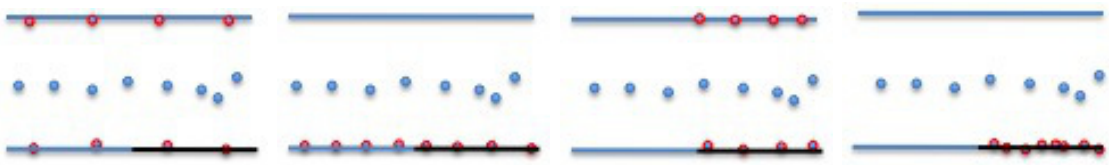

Figure 3.17 : Illustration of the different charge distribution schemes. Positive (wall) and negative (particle) charges are shown as plus and minus symbols, respectively, and the wetting stripe is shown in thick line.

For definiteness, we assume the particles have only negative charge while the walls have only positive charge, subject to overall electrical neutrality. Four different wall charge arrangements are considered, shown in Fig. 3.17. Scheme 1 distributes charges randomly on all of both walls, scheme 2 has charges on all of the bottom wall only, scheme 3 places half the charges on the wetting stripe of of bottom wall and the other half on the complementary region of the top wall, and scheme 4 has all charges on the wetting stripe of the bottom wall. Fig. 3.18 shows the the final

configurations in simulations with these charge distributions. For system with charges on both walls (schemes 1 and 3) the particles are divided into two groups, one near the top wall moving with high velocity, and the second near the bottom wall moving with low velocity, due to the attractive interaction with the substrate. The behavior in these two schemes is qualitatively similar to the uncharged case discussed above: the particles have some new attraction to either wall but not a specially enhanced attraction to the wetting stripe, and the principal effect of the electrostatic interaction is to draw the particles away from the center of the channel and thereby slow them down somewhat. If instead only the bottom wall is charged (schemes 2 and 4), particles tend to move near the bottom wall and their mean transport velocity is relatively small. Here the charges act in concert with the wetting interaction and increase the degree of trapping. We see from the figure that scheme 2 is most effective at altering the transport angle but tends to trap the particles. Schemes 1 and 3 are only modestly effective in producing a trajectory deflection but do permit transport over large distances. Scheme 4, which has the strongest patterning interaction, and which one might have anticipated to be the most effective choice, is in this case apparently too strong and simply traps the particles.

At this point we can compare the explicitly two-dimensional version of the Ewald sum to a common approximation in which the full three dimensional method is used but the effects of periodicity in the unwanted (y) direction is lessened by making the box size much larger than the actual width of the system L_y, so as to reduce the influence of those periodic copies. Fig. 3.19 shows a comparison of the two methods, where in the approximate 3D method the periodicity in y is chosen to be $5L_y$. In most cases the differences are small; the difference in transport distance is probably insignificant but, again, even a small difference in trajectory angle has a large effect

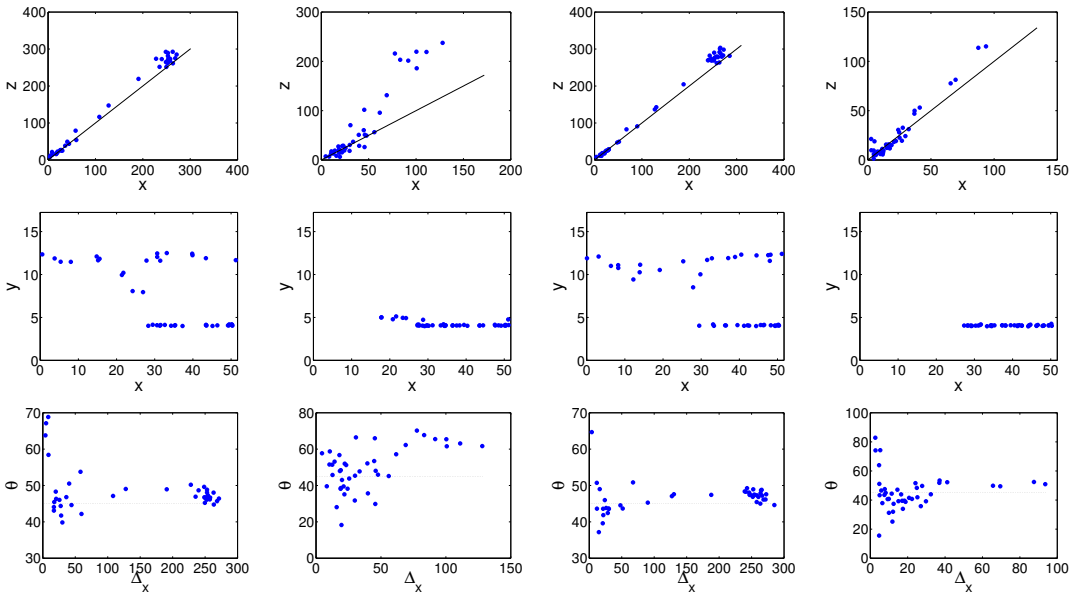

Figure 3.18 : MD results for charged system with particle radius $r = 2.15$, $\lambda = 1.5$, $g = 0.02$ and a charge per particle of $6e$. Left to right: schemes 1 to 4; Top row: final positions in the (x-z) flow plane; Middle row: side (x-y) view of the final configurations; Bottom row: transport angle θ vs transport distance Δx.

of the particle position.

The effect of varying the particle charge is indicated in Table 3.2, which gives the trajectory angle θ and distance traversed Δ_x for each scheme, averaged over the particles. In general, increasing the charge per particle leads to the decrease in Δx and increase of θ. The decrease of covered distance results from increased attraction or trapping, which in turn causes an increase in θ because such particles tend not to leave the wetting stripe while being relatively free to move parallel to it. Note that this argument would imply that the trapped particle deflections are almost as likely to be negative as positive, in contrast to the deflections of mobile particles which by the argument given in the introduction should be positive. The numerical results support this interpretation. The results in Table 3.2 again indicate very similar

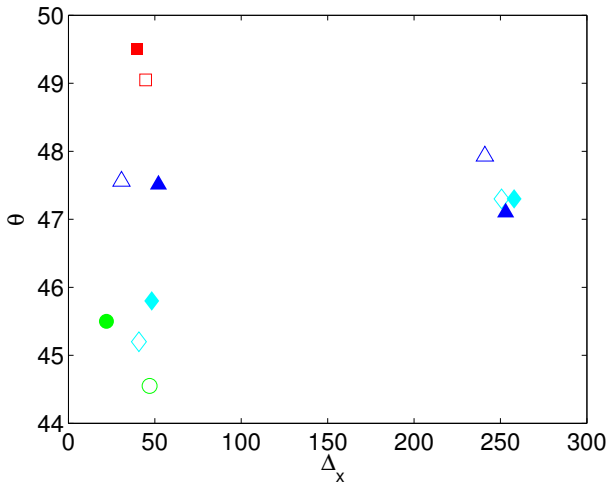

Figure 3.19 : Comparison of 2D and 3D Ewald Sum: transport angle vs transport distance Δx for particles of radius $r = 2.15$ with charge $6e$. Hollow symbol: 3D method, solid symbol: 2D method; scheme 1 (triangle), scheme 2 (square), scheme 3 (diamond) and scheme 4 (circle).

behavior for charge schemes 1 and 3, and scheme 2 shares the feature that increasing charge increases θ, but scheme 4 surprisingly has the opposite behavior.

The simulations in schemes 2 and 4 were extended to longer times, three times the duration shown above, to decisively determine their asymptotic behavior. In scheme 2, some particles are trapped near the wetting stripe on the bottom wall, but others continue to move indefinitely with a large deflection angle. In contrast, in scheme 4 all of the particles eventually become trapped on the wetting stripe, and the difference between them is presumably that in this case the charge *density* is higher than in scheme 2 and when combined to the wetting interaction leads to a very strong trapping effect. However, in scheme 2 the particle are not far from the lower wall and the wetting stripe, so even if not trapped they interact strongly enough to produce large trajectory deflections. Indeed, the deflections are larger than

in the uncharged case in Fig. 3.11, because many of the particles there do not feel any significant wall interaction at all. The net wall interaction therefore requires careful tuning for optimal separation: large enough for the particle motion to be affected but not so large as to trap them.

In these simulations the dielectric properties of the solvent were ignored; in fact in these simulations the only effect of dielectric permittivity of the solvent material is to renormalize the charge and we have accounted for this effect in Table 3.2. For example, if we use the room temperature dielectric constant of water, $\epsilon_r \approx 81$, the Coulomb force is the same as if each charge were reduced by a factor of 9. Figure 3.20 shows the simulation results of different schemes with permittivity turned on. Both the argument and the simulation suggest that higher charge density is needed for larger deflection angles

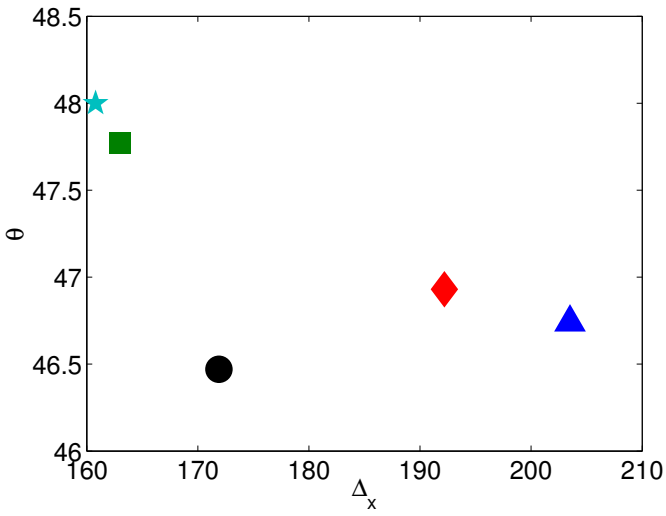

Figure 3.20 : Results of MD simulation with water's dielectric constant accounted for: transport angle θ vs transport distance Δ_x for particles of radius $r = 2.15$ with charge $9e$. Water's relative permittivity $\epsilon_r = 81$. Triangle: Scheme 1, Square: scheme 2, Diamond: scheme 3 and Pentagon: scheme 4. Circle: uncharged system.

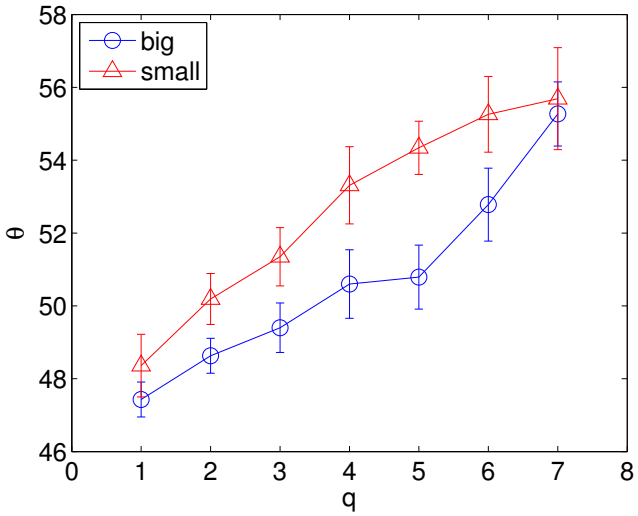

Figure 3.21 : Mean transport angle θ as a function of charge density q in mixture system. Particle number: 12 small particles with $r = 2.15\sigma$ and charge per particle q and 12 big particles with radius $r = 4.3\sigma$ and charge per particle $4q$.

To demonstate particle separation in a more practical sense we consider a mixture of charged particles of different sizes transporting in a nanochannel with a surface gradient. We consider an MD simulation of a binary mixture consisting of equal number of particles with different radii, assigned different amounts of charge proportional to their surface areas. To neutralize the particle charges scheme 2 is used, i.e., all compensating charges are uniformly distributed on the bottom wall where the surface gradient is present, with affinity parameter $\lambda = 1.5$. The flow is directed at 45° in the xz plane by a body force $g = 0.02$. The results, shown in Fig. 3.21, indicate that small particles have a higher transport angle than big particles, by approximately 2°. The observation of the positive correlation between q and θ is consistent with the fact that the particle deflection can be enhanced by the attractive wall force of which the Coulomb part is proportional to q^2. The origin of the difference can be

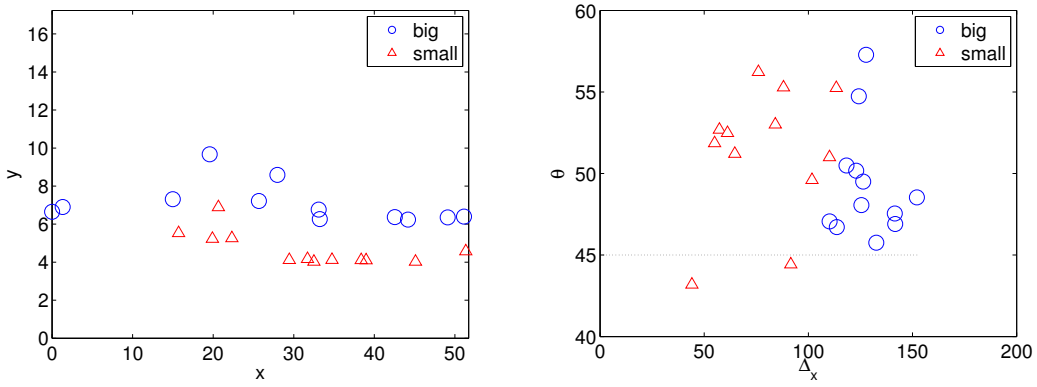

Figure 3.22 : Left: Side view of final configurations for mixture system at $q = 3e$; Right: Transport angle θ versus transport distance Δ_x for individual particle for mixture system at $q = 3e$.

seen in Fig. 3.22, which shows individual particle behaviors for the binary system at $q = 3e$. It is well known that when a binary mixture flows the large particles tend to occupy the center and exclude the small ones, which preferentially populate the region near the walls. The small particles are then more stroingly attracted to the substrate, and because of their high diffusivity can quickly respond to the attractive wall force. When the small particles saturate the region above the attracting substrate they effectively screen charge from the big particles, which then move in the weak potential region with higher velocities and smaller deflection angle. If the charge is large enough, however, the electrostatic forces overcome the hydrodynamic segregation and all particles will be drawn to the substate. In this limit the particle trajectories are relatively insensitive to size, as seen by the convergence of the two curves in Fig. 3.21 at large q.

We conclude that Coulomb potential can enhances the deflection of trajectories, but at the same time may increase the amount of particle trapping, and furthermore may not have an adequate sensitivity to particle radius for separation applications.

3.4 Continuum Model

3.4.1 Brownian Dynamics

The MD simulation method could be used for particles of any size, but as the particle size increases the amount of fluid solvent which must be included in order to simulate a dilute suspension increases in tandem, and the computational cost eventually becomes prohibitive. We turn instead to a simpler computational method, the Langevin equation, which has the further advantage that its accuracy increases with particle size. In this approach, the velocity of a suspended particle of mass m and radius R satisfies

$$m\frac{d\mathbf{v}}{dt} = -\gamma[\mathbf{v} - \mathbf{u}(\mathbf{r})] + \mathbf{F}_{ext} + \boldsymbol{\Gamma}(t), \tag{3.13}$$

where $\mathbf{u}(\mathbf{r})$ is the local flow velocity at the position $\mathbf{r}$ of the particle, $\gamma = 6\pi\mu R$ is the Stokes drag coefficient (μ is the fluid viscosity), and $\mathbf{F}_{ext}$ is any external force acting on the particle. The fluctuating collisions between the particle and the surrounding fluid molecules are approximated by a stochastic force $\Gamma(\mathbf{t})$ whose correlation function satisfies

$$\langle \Gamma_i(t)\Gamma_j(t')\rangle = \frac{2\gamma kT}{m}\delta ij\,\delta(t-t'). \tag{3.14}$$

In reality this force has finite temporal and spatial correlations due to the structure of the solvent fluid, but for large particles whose size is greater than the correlation length different regions of neighboring fluid will act independently, and furthermore large particles will not move very far over the correlation time of the solvent, and it is reasonable to approximate the solvent interaction as random kicks. Frequently a further approximation is made that the particle's motion is overdamped and the left hand side of Eq. 3.13 is set to zero, but we will retain the full equation here.

In the present situation, the external force arises from the spatially-dependent

substrate interactions, which are evaluated in the same way as in the MD simulations. The local flow velocity just corresponds to Poiseuille flow and could be inserted either analytically or from the velocity profile obtained in the MD simulations, which have little difference in this case. When the Langevin equation is solved by a time-stepping algorithm with step-length Δt, the random force is implemented as

$$\Gamma_i(t) = \sqrt{\frac{2\gamma kT}{m\Delta t}}\,\xi_i(t), \tag{3.15}$$

where at each step $\xi_i(t)$ is a new Gaussian random number with zero mean and unit variance.

The predictor-corrector method used in the MD simulations does not lend itself to a stochastic and velocity-dependent differential equation, so instead we use an algorithm suggested by the Verlet method in MD [67]. For each component of Eq. 3.13 we write

$$r(t+\Delta t) = r(t) + v(t)\Delta t + \frac{1}{2}a(t)\Delta t^2 + \frac{1}{6}\dot{a}(t)\Delta t^3 + O(\Delta t^4),$$

where $v(t)$ is the velocity, $a(t)$ the particle acceleration (the terms on the right-hand side of Eq. 3.13 divided by m) and Δt is the numerical time step. Combining this equation with its counterpart for $r(t-\Delta t)$, we can update the position using

$$r(t+\Delta t) = 2r(t) - r(t-\Delta t) + a(t)\Delta t^2 + O(\Delta t^4). \tag{3.16}$$

The velocity can be updated to third-order accuracy via

$$v(t+\Delta t) = v(t) + \frac{1}{2}[a(t) + a(t+\Delta t)]\Delta t + O(\Delta t^3).$$

where the new acceleration is simply given by the Langevin equation at time $t+\Delta t$. Substituting and rearranging the result, we have

$$\left[1 + \frac{\gamma\Delta t}{2m}\right] v(t+\Delta t) = \left[1 - \frac{\gamma\Delta t}{2m}\right] v(t) + \frac{\Delta t}{2m}\left[\phi(t) + \phi(t+\Delta t)\right] \tag{3.17}$$

where $\phi \equiv \gamma u + F_{ext} + \Gamma$.

The Langevin simulation is performed within a box of the same size as the MD simulation of finite sized particles, again with periodic boundary conditions applied in the x and z directions. The particle's explicit interaction with the substrate surface layer, which would not be resolved at the level of resolution the Langevin equation, is replaced by a simple repulsive force to prevent penetration into the walls. The external force then consists of this short-ranged repulsion plus the long-ranged attractive force from the wetting stripes. We again focus on a flow directed at 45° within the x-z plane by a body force $g = 0.01$. Initially, 100 (non-interacting) particles are distributed uniformly along the y-axis and the Langevin equations is integrated up to time $300{,}000\tau$ with time step $\Delta t = 0.01\tau$.

First, we test the agreement between the Langevin equation and its simulation method and the corresponding Fokker-Planck equation discussed in the following section. The latter is solved analytically in 2D theory. The test uses a simple periodic function for the potential, $V(x) = A\ sin(2\pi x/L)$. and the two solutions are compared in Fig. 3.23. The relation between flow velocity u_x and Péclet number Pe is $Pe = 3843u_x$ given the particle radius $r = 2.0$. The two methods match very well when the Péclet number is not too small, $Pe \geq 20$,and even in the worst case when the fluctuations in the Langevin solution are large the Fokker-Planck equation generally agrees. Note that for this potential small Péclet number($Pe \leq 200$) and small radius ($r \leq 4.0$) leads to a large deflection angle.

Next we compare the results of MD and Langevin simulations in Fig. 3.24. Note that the two methods are *not* expected to produce the same solution here, because physically they are meant to apply to particles of distinctly different sizes (comparable and much larger than the atomic scale, respectively) and algorithmically the

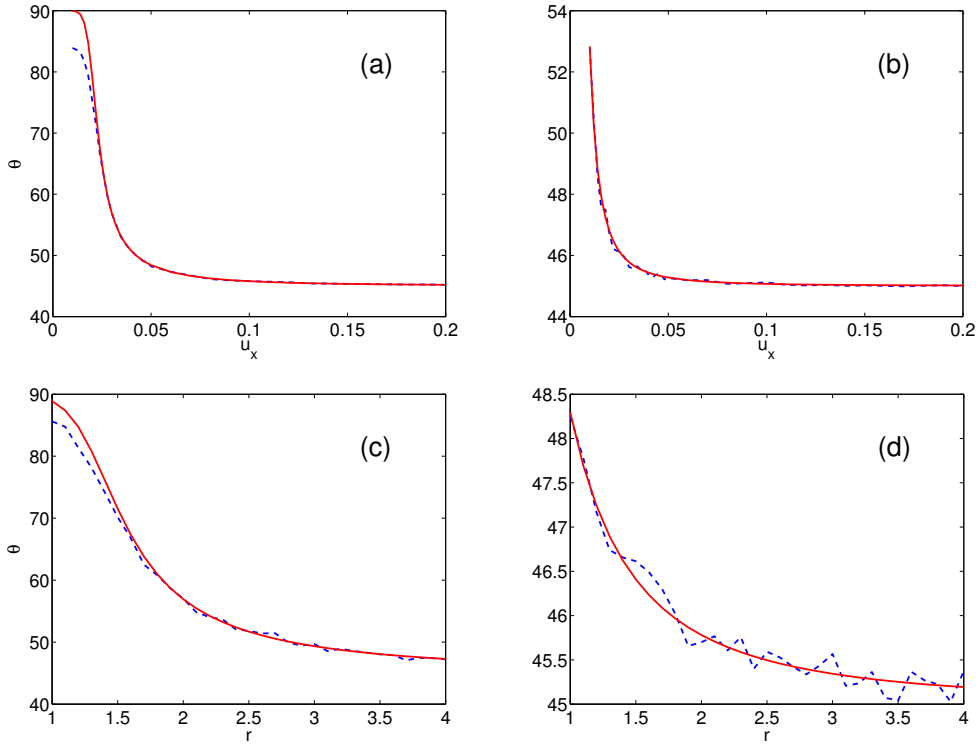

Figure 3.23 : Comparison of solutions of the Fokker-Planck (red solid line) and Langevin solutions (blue dashed line). Transport angle θ *vs. Péclet number for (a)*$A = 10.0$ *and* $r = 2.0$ *and (b)* $A = 3.0$ *and* $r = 2.0$*; Transport angle theta*vs. particle radius r at (c) $A = 10.0$ and $u_x = 0.03$ and (d) $A = 3.0$ and $u_x = 0.03$.

Langevin particles are points which see a continuum wall and while not interacting with each other. The plots indicate that at small Pe the two methods give somewhat similar results, but at high flow velocities the MD particles tend to move with same velocity while the Langevin particles distribute relatively uniformly in velocity space. Furthermore, unlike the MD situation, because the Langevin particles are non-self-interacting points, they are free to accumulate next to the patterned wall without any packing limitations and readily become trapped.

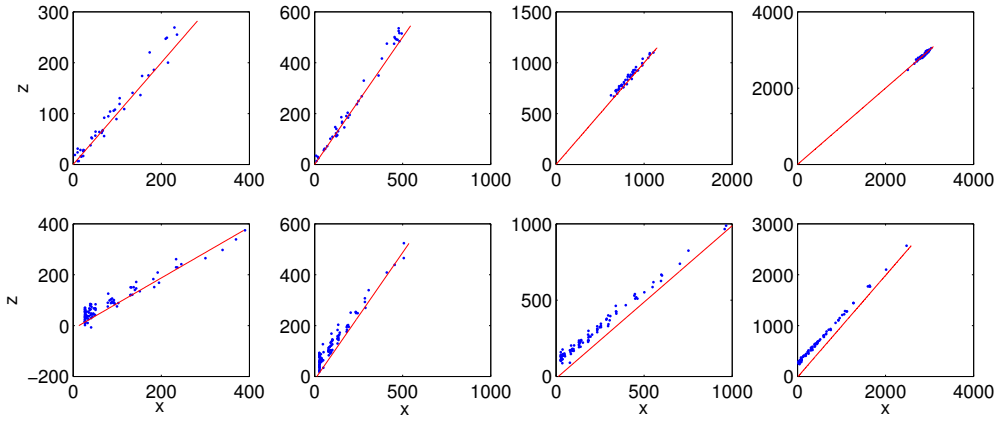

Figure 3.24 : Comparison of MD and Langevin simulations at $r = 2.15$ and $\lambda = 1.5$. Top row: MD, bottom row: Langevin; Left to right: $g = 0.005$, 0.01, 0.02 and 0.05.

3.4.2 Fokker Planck Formalism

The Langevin equation for individual particle trajectories used in the previous section is equivalent to a Fokker Planck equation for the probability distribution of the particles [65], which allows us to study this situation by analytical methods and derive bounds on the trajectory deflection. The discussion here is motivated by Bernate and Drazer's [19] macroscopic treatment of particle motion across striped substrates.

The spatial probability distribution function $Q(\mathbf{r}, \mathbf{t})$ of particles which are at position $\mathbf{r}$ at time t satisfies an equation of continuity

$$\frac{\partial Q}{\partial t} = \nabla \cdot \mathbf{J} = \mathbf{u}\, Q - \mathbf{M} \cdot \nabla V - k_B T\, \mathbf{M} \cdot \nabla Q \tag{3.18}$$

where the particles have mobility tensor $\mathbf{M}$ and move in a velocity field $\mathbf{u}$ under a potential V, subject to some initial condition. We are interested here in the steady state distribution in a 2D periodic geometry, so it is advantageous to consider the long-time limit of the distribution with respect to the primary periodic cell alone,

$$P(\mathbf{r}) = lim_{t\to\infty} \sum_{n,m} Q(\mathbf{r} + \mathbf{R}_{n,m}, t), \tag{3.19}$$

where $\mathbf{R_{n,m}}$ is the location vector of cell (n, m) in the plane and $\mathbf{r}$ is the intra-cellular position vector. By using the above notation, one can focus on a finite domain with periodic boundary conditions. The steady-state current satisfies $\nabla \cdot \mathbf{J} = \mathbf{0}$.

We begin by simplifying the problem from three dimensions to two, by noting that the velocity field is in the x-z plane, ignoring the variation across the narrow gap in y and taking the potential to be a periodic function of x alone. We then have

$$\frac{\partial J_x}{\partial x} + \frac{\partial J_z}{\partial z} = 0, \tag{3.20}$$

where

$$J_x = u_x P - \frac{\partial V}{\partial x} MP - k_B T M \frac{\partial P}{\partial x} \qquad \text{and} \qquad J_z = u_z P. \tag{3.21}$$

Note that J_z is simple because the potential varies only in x and in the long-time limit of diffusion makes P independent of z. Note that steady flow conditions imply that u_x and u_z are constants in time.

To nondimensionalize the above equations, define $x' = x/L$, $V' = V/k_BT$, $P' = LP$, $J' = LJ/u_x$ and Péclet number $G = u_x L/(k_B T M)$. Here L is the period of $V(x)$, and we use G for Péclet number in the interests of readability. Dropping the primes, Eq. (3.21) becomes

$$GJ_x = (G - \frac{\partial V}{\partial x})P - \frac{\partial P}{\partial x}. \tag{3.22}$$

P obeys periodicity and normalization conditions

$$P(x+1) = P(x), \qquad \int_0^1 P(x)\, dx = 1. \tag{3.23}$$

and should be independent of z, so from Eq. (3.20) one finds that $J_z = J_z(x)$ and J_x is constant.

To calculate the flux J_x we introduce $f(x) = e^{V(x)-Gx}$, $A(x) = \int_0^x f(x')dx'$ and

$A_1 = A(1)$. In Appendix. .2 we show that

$$\frac{1}{J_x} = G\left[\frac{A_1}{1-e^{-G}}\int_0^1 \frac{dx}{f(x)} - \int_0^1 \frac{A(x)}{f(x)}\,dx\right]. \tag{3.24}$$

If the potential $V(x)$ is constant the corresponding flux J_x^0 can be easily calculated from Eq. (3.24): $J_x^0 = 1$. We denote the ratio of J_x^0 to J_x by

$$\kappa \equiv \frac{J_x^0}{J_x} = G\left[\frac{A_1}{1-e^{-G}}\int_0^1 \frac{dx}{f(x)} - \int_0^1 \frac{A(x)}{f(x)}\,dx\right]. \tag{3.25}$$

Since J_x is a constant it automatically equals its mean flux, $\bar{J}_x = \int_0^1 J_x dx / \int_0^1 dx = J_x$, and due to the constancy of J_z and the non-dimensionalization above the mean z-flux $\bar{J}_z = \int_0^1 J_z dx / \int_0^1 dx = u_z/u_x$. The mean migration angle of the particles θ satisfies

$$\tan\theta = \frac{\bar{J}_z}{\bar{J}_x} = G\left[\frac{A_1}{1-e^{-G}}\int_0^1 \frac{dx}{f(x)} - \int_0^1 \frac{A(x)}{f(x)}\,dx\right]\tan\theta_F = \kappa\tan\theta_F. \tag{3.26}$$

and so κ describes the amount of trajectory deflection, independent of the value of the flow angle θ_F. We shall see later that necessarily $\kappa \geq 1$, which implies $J_x \leq J_x^0$ and $\theta \geq \theta_F$. It is straightforward to show that the maximum deflection angle $\Delta\theta = \theta - \theta_F$, occurs when $\theta_F^0 = \arctan(\kappa^{-1/2})$. In the MD simulations κ turned out to be close to one and the maximum deflections occurred art, $\theta_F \simeq 45°$, consistent with this result.

In Appendix. .3 we show that Eq. (3.26) can be rewritten as

$$\kappa = \frac{G}{1-e^{-G}}\int_0^1 dx \int_x^1 dx' \left[e^{G(x'-x-1)}e^{V(x)-V(x')} + e^{G(x-x')}e^{V(x')-V(x)}\right], \tag{3.27}$$

and defining an intermediate function

$$p(y) = \int_0^1 dx\, e^{V(x+y)-V(x)}, \tag{3.28}$$

which is periodic and has the property $p(0) = p(1) = 1$, one can rewrite the previous equation as

$$\kappa = \frac{G}{1-e^{-G}}\int_0^1 dy\, e^{-Gy}p(y) = G\int_0^{+\infty} dy\, e^{-Gy}p(y) \tag{3.29}$$

which is the product of G and Laplace transform of $p(y)$ with respect to G. In Appendix. .4 we show that $p(y) \geq 1$ which establishes a lower bound on κ:

$$\kappa \geq \frac{G}{1-e^{-G}} \int_0^1 dy\, e^{-G\,y} = 1. \tag{3.30}$$

The lower bound is reachable: when $G \to \infty$, eventually the e^G terms in the integrand of Eq. (3.27) dominate the e^V terms and this equation reduces to

$$\kappa = \frac{G}{1-e^{-G}} \int_0^1 \int_x^1 (e^{G(x'-x-1)} + e^{G(x-x')})\, dx dx' = 1. \tag{3.31}$$

The lower bound of κ implies that the deflection angle $\Delta\theta = \theta - \theta_F$ is always nonnegative, again consistent with the MD results. Furthermore, in Appendix. .5, we show that within the Fick-Jacobs approximation to the fully 3D version of the problem, the lower bound on κ still holds.

The lower bound can be restated as the property that the flux at steady state will always become slower when a periodic potential is present compared to zero potential case, *i.e.,* $J_x \leq J_x^0$. This reduction in flux may be understood by considering two limiting cases. In the absence of convection, Jackson and Coriell [82] pointed out that a zero-mean potential with a one-dimensional periodic variation reduces a particle's effective diffusivity. Since the diffusivity is proportional to the mobility, by Einstein's relation, this result is equivalent to stating that a particle's mean transport velocity decreases. Another limiting case concerns the Newtonian mechanics of a particle in the same class of potentials. If a particle has mass m and energy E, the transit time across one period of the potential is

$$T = \sqrt{\frac{m}{2E}} \int_0^L \frac{dx}{\sqrt{1 - V(x)/E}} \tag{3.32}$$

Write the potential as $V(x) = \alpha\beta(x)$ where $\beta(x+L) = \beta(x)$, the maximum value of $\beta(x)$ is unity, α is the maximum value of the potential and we choose $E > \alpha$ so that

the particle is not trapped in a sub-interval. The zero-mean condition is

$$\int_0^L dx\,\beta(x) = 0 = \int_{\beta(x)>0} dx\,\beta(x) - \int_{\beta(x)<0} dx\,|\beta(x)| = 0. \tag{3.33}$$

To show that the potential retards the motion it suffices to show that $dT/d\alpha > 0$. Now

$$\begin{aligned}\frac{dT}{d\alpha} &= \sqrt{\frac{m}{8E^3}}\int_0^L \frac{dx\,\beta(x)}{(1-\alpha\beta(x)/E)^{3/2}} \\ &= \sqrt{\frac{m}{8E^3}}\left[\int_{\beta(x)>0} \frac{dx\,\beta(x)}{(1-\alpha\beta(x)/E)^{3/2}} - \int_{\beta(x)<0} \frac{dx\,|\beta(x)|}{(1-\alpha\beta(x)/E)^{3/2}}\right]\end{aligned} \tag{3.34}$$

The first integral is greater than $\int_{\beta(x)>0} dx\,\beta(x)$ because the denominator is less than one everywhere in its range of integration, while the second integral is less than $\int_{\beta(x)<0} dx\,|\beta(x)|$ because its denominator is everywhere greater than one. Hence from Eq. 3.33

$$\frac{dT}{d\alpha} > \sqrt{\frac{m}{8E^3}}\left[\int_{\beta(x)>0} dx\,\beta(x) - \int_{\beta(x)<0} dx\,|\beta(x)|\right] = 0 \tag{3.35}$$

Therefore, within the approximations used above, the Fokker-Planck equation shows when that a particle advects in a constant flow field its mean transport velocity at steady state is reduced by the action of any periodic potential. Note that application of a constant force is equivalent to adding a constant flow velocity $\Delta u = MF$, and the conclusion and bounds still apply in this case.

There is also an upper bound on κ which depends only on the potential: in Appendix. .6 we show

$$\kappa \le \iint_0^1 dxdy\, e^{2(V(x)-V(y))} \Big/ \iint_0^1 dxdy\, e^{V(x)-V(y)}, \tag{3.36}$$

This upper bound need not be saturated, and in this connection, it is instructive to consider the small-Péclet number limit. When $G \to 0$, Eq. (3.27) becomes

$$\kappa \to \kappa_0 = \int_0^1 dx \int_x^1 dx' \left[e^{V(x)-V(x')} + e^{V(x')-V(x)}\right] = \iint_0^1 dxdy\, e^{V(x)-V(y)}. \tag{3.37}$$

which, by the Cauchy-Schwarz inequality, is smaller than the upper bound.

The lower bound $\kappa \geq 1$ is slightly unsatisfying because the previous arguments suggest that *any* deviation from a constant potential would deflect the particles. While we do not have a general analytic argument, in Appendix. .7 we relate the trajectory deviation to the variance of the potential in the limit that the latter is weak compared to $k_B T$. If furthermore, the Péclet number vanishes we show that $(\kappa - 1)$ is proportional to $\langle \Delta V^2 \rangle$.

Finally, note that the formula for κ is asymmetric in the spatial variable x. If the flow is driven in the opposite direction with the same Péclet number G, it is easy to show that Eq. (3.27) becomes

$$\kappa = \frac{G}{1 - e^{-G}} \int_0^1 dx \int_x^1 dx' \left[e^{G(x'-x-1)} e^{V(1-x)-V(1-x')} + e^{G(x-x')} e^{V(1-x')-V(1-x)} \right]. \tag{3.38}$$

If the potential is asymmetric, the forward and backward values of κ differ.

Scheme	Charge	$\bar{\Delta}_x(\sigma)$	$\bar{\theta}(^\circ)$	$\bar{\Delta}_x^1(\sigma)$	$\bar{\theta}^1(^\circ)$	$\bar{\Delta}_x^2(\sigma)$	$\bar{\theta}^2(^\circ)$
1	2	207.4	46.18	102.2	46.44	312.6	45.92
1	6	147.8	48.31	52.1	49.42	253.0	47.10
1	9	120.5	47.90	45.3	46.50	203.3	49.44
2	2	137.2	46.80	-	-	-	-
2	6	39.8	49.51	-	-	-	-
2	9	15.9	57.48	-	-	-	-
3	2	217.1	45.90	139.2	46.12	321.0	45.81
3	6	158.0	46.60	48.2	45.81	257.9	47.33
3	9	116.3	47.07	33.6	43.66	191.5	50.17
4	2	137.2	46.92	-	-	-	-
4	6	22.0	45.50	-	-	-	-
4	9	16.2	36.25	-	-	-	-
-	0	171.9	46.47	-	-	-	-

Table 3.2 : Transport distances and orientations for different charge schemes and values of charge per particle. In cases where there is a clear distinction between trapped and mobile particles, separate averages are presented; these are denoted by superscripts 1 and 2. The last row is a control group: the results for an uncharged system.

Chapter 4

Nano Drop Impacts On Heterogeneous Surfaces

In this chapter, we discuss the dynamics of a nano meter sized drop impact on surfaces with various properties. We first describe the physical properties of the drop and how to measure them in the MD simulations. Next we look at the typical behaviors of drops impact on homogeneous non-wetting or wettable surfaces and compare the results with LB method. In last section we simulate drop impact on various types of patterned surfaces.

4.1 Properties of Nano Drop

4.1.1 Surface Tension

Surface tension is an important dynamic property to any multiphase system. It is a contractive tendency of the surface of a phase that allows it to resist an external force. In thermodynamics, it can be regarded to be how the free energy responds to the change of surface area. Namely, Helmholtz free energy F can be expressed by

$$dF = -SdT - PdV + \gamma dA,$$

where A is the surface area and γ is the so called surface tension. S, T, P and V are the system's entropy, temperature, pressure and volume, respectively. The principle of minimum free energy can easily yield the principle of minimum surface area, which can be used to explain a wide range of phenomena, e. g. the shape of a liquid drop without contacts is always a sphere at equilibrium. Due to the interfacial tension,

the pressure between the inside and outside of a liquid drop is different. Generally speaking, given a smooth interface with principal radii of curvature R_1 and R_2, the pressure jump ΔP across the interface can be related to the interfacial tension by

$$\Delta P = \gamma \left(\frac{1}{R_1} + \frac{1}{R_2} \right).$$

By measuring the radius and the pressure inside and outside a sphere liquid drop, one can determine the surface tension of the liquid. If the interface is flat given its normal is in the z direction, it can be shown by the thermodynamical relation that γ can be calculated by

$$\gamma = \frac{1}{2A} \int_{-\infty}^{+\infty} (p_N(z) - p_T(z)) dz,$$

where $p_N(z)$ and $p_T(z)$ are the pressures normal and tangential to the interface, respectively. The Virial form of the stress tensor is

$$\vec{\vec{\sigma}} = \frac{1}{V} \left[\sum_i -m_i (\vec{u_i} - \langle \vec{u_i} \rangle)(\vec{u_i} - \langle \vec{u_i} \rangle) + \frac{1}{2} \sum_{i \neq j} \vec{r}_{ij} \vec{F}_{ij} \right].$$

The pressure tensor $p_i = -\sigma_{ii}$, $i =x$, y and z. Thus γ can be rewritten by the particle's positions and intermolecular potentials:

$$\gamma = \frac{1}{2A} \langle \sum_{i<j} \frac{r_{ij}^2 - 3z_{ij}^2}{r_{ij}} V'(r_{ij}) \rangle,$$

where $\langle \rangle$ is the ensemble average, r_{ij} is the distance between particle i and j, and $-V'(r_{ij})$ is the inter particle force between i and j. This formula can be easily implemented in the molecular dynamics. We've measured various one component systems by the above formula and list some of the results in the following table:

The surface tension of nano liquid is in the order of $1mN/m^2$, compared to $72mN/m^2$, the typical value of water-air interfacial tension at room temperature.

l	$k_BT(\epsilon)$	$\rho_l(m\sigma^{-3})$	$\rho_v(m\sigma^{-3})$	$\gamma(\epsilon/\sigma^2)$
1	0.8	0.65	0.052	0.17 ± 0.02
2	0.8	0.80	2.8×10^{-3}	0.49 ± 0.02
4	0.8	0.86	1.3×10^{-5}	0.69 ± 0.02

Table 4.1 : Surface tension γ for different polymer length l. ρ_l is the liquid phase density and ρ_v is the vapor phase density.

4.1.2 Contact Angle

Youngs's equation states that the contact angle can be related to the surface tension:

$$\cos\theta = \frac{\gamma_{vs} - \gamma_{ls}}{\gamma_{lv}},$$

where l, v and s refer to liquid, vapor and solid phase, respectively. In the MD simulation, The correspondence between the contact angle θ and c can be either roughly estimated by $\cos\theta = 1 - 2c\rho_s/\rho_l$[83], where $\rho_{s,l}$ are the liquid and solid densities, respectively, or more precisely measured by a separate simulation, with the results given in Table. 4.2.

c	0	0.4	0.67	0.8	0.9	1.0
θ	180°	134°	96°	73°	50°	0°

Table 4.2 : The contact angle θ as a function of the wettability c for dimer system of density $\rho = 0.8m\sigma^{-3}$ at temperature $T = 0.8\epsilon/k_B$.

4.1.3 Viscosity

Viscosity is the measure of the resistance of a liquid to the shear or tensile deformation. In microscopic view of point, viscosity is due to the friction between neighboring parcels of the fluid that are moving at different velocities. Dynamic(Shear) viscosity μ is defined by the ratio of the shear stress to the velocity gradient:

$$\tau_{xy} = \mu \frac{\partial u_x}{\partial y}.$$

Several methods can be used to measure the viscosity in MD. The most straightforward one is to create a Couette or Poisseuille flow in a flat channel bounded by two walls and measure the stress and velocity gradient respectively. An alternative method which does not involve solid walls is the Lees-Edwards boundary condition.

Another method measures the correlation function of the equilibrated liquid system. Given the shear stress in the Virial form

$$\sigma_{xy} = \sum_i m_i \dot{x}_i \dot{y}_i + \frac{1}{2} \sum_{i \neq j} F_{xij} r_{yij},$$

Green-Kubo relation states that the shear viscosity can be calculated by

$$\mu = \frac{\beta}{V} \int_0^\infty dt \langle \sigma_{xy}(t) \sigma_{xy}(0) \rangle$$

l	$\rho(m\sigma^{-3})$	$\mu(m\sigma^{-1}\tau^{-1})$
1	0.8	2.2 ± 0.1
2	0.8	2.7 ± 0.1
4	0.86	3.9 ± 0.1

Table 4.3 : Viscosity μ for different polymer length l at temperature $T = 0.8\epsilon/k_B$.

4.2 Model Description of Drop Impacts Heterogeneous Surfaces

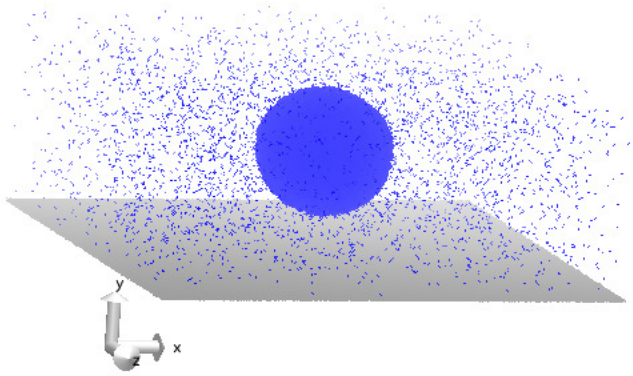

Figure 4.1 : Snapshot of a volatile dimer drop and vapor above a solid surface before impact in an MD simulation.

In a typical molecular simulation, shown in Fig. 4.1, a drop plus vapor system of 115,392 dimer molecules floats above a flat surface composed of 245,650 wall atoms arranged into one layer of *fcc* cells, all placed in a box of size (300σ, 120σ, 300σ). To quantitatively describe the drop dynamics after impact some numerical characterization of the drop shape is needed. A typical drop shape slightly after impact is shown in Fig. 4.2, along with its boundary. Provided that the solid surface is uniform and we avoid the splashing regime, the drop is observed to spread with approximate radial symmetry in the plane of the surface. Using a cylindrical coordinate system whose (y-)axis is a vertical line through the center of the drop, three obvious geometrical parameters characterizing the r-y profile are the drop height h, the spreading radius R_s and the radius of the contact area R_c. The intrinsic length scales of the MD and LB calculations are different, and to facilitate a comparison we normalize all lengths

by the initial drop radius R_0.

In drawing Fig. 4.2 the boundary of the drop is assumed to be a line, but in fact in both computations and in reality a liquid vapor interface is a transition region of finite thickness. Our procedure is based on the fluid density field $\rho(r, y)$ in the cylindrical coordinate system above. Before impact we observe that away from the interface the density has constant values ρ_l and ρ_v in the center of the drop and in the distant vapor regions, respectively, and we identify the interface as the midpoint curve on which $\rho(r, y) = (\rho_l + \rho_v)/2$. Typical MD values are $\rho_l = 0.8$ mσ^{-3} and $\rho_v = 10^{-3}\rho_l$, with an interfacial thickness O(2-3 σ). Strictly speaking, in MD simulations at any single time ρ is a sum of delta-functions centered at the current atomic positions but if we time-average over a 1 τ interval a smoothly-varying field results. In the LB the situation is simpler because this continuum density field is a direct output of the calculation.

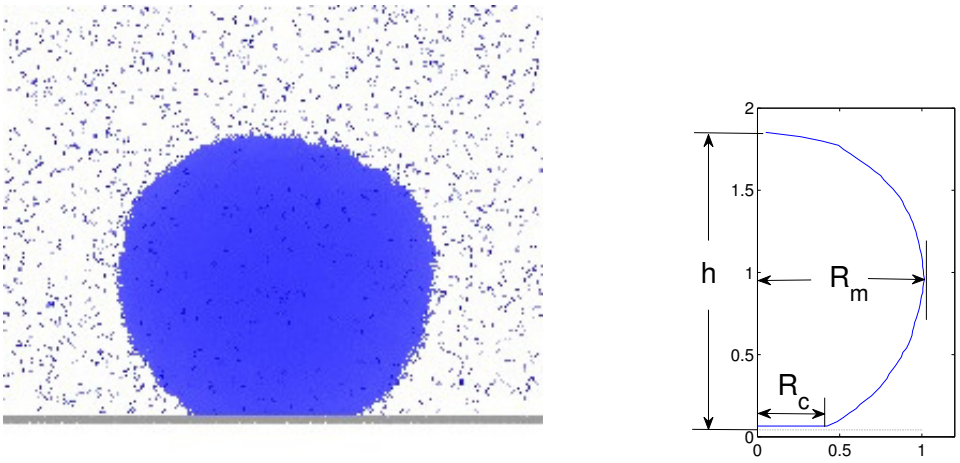

Figure 4.2 : Snapshot of an early stage of drop spreading (left) and the corresponding interfacial contour (right), as obtained by the method described in the text. The definitions of h, D_s and D_c are illustrated and the dashed line is the wall.

While h and R_m are now well defined, there is some further ambiguity in the measurement of R_c because "contact" is ill-defined at molecular scales. There is always a finite distance between the adjacent liquid and wall atoms (due to the repulsive core of the potential), whose value depends on the wettability of the surface. Our rule is to choose a critical value b_c of the gap between the interface contour defined above and the average position of the top wall atoms, and say that contact occurs where the gap $b(r) < b_c$.

In analyzing the time dependence of the drop parameters a starting time must be chosen, which is also ambiguous because of the finite range of the interaction. Our convention is to start the measurement at the moment when the drop "geometrically" touches the surface, meaning when when $h = 2R_0$. In the MD simulations, at this time there are always drop molecules within the critical gap thickness and contact in the sense of the previous paragraph has been made, but in the LB case we find that the drop height h is distorted by up to 5% before the contact line forms. In experiment an additional complication may arise - an air bubble trapped in the center immediately after drop impacts the wall [84], which may delay the formation of a contact line, but such bubbles are not observed here.

4.3 Nano Drop Impacts Homogeneous Surfaces

4.3.1 Non-wetting Surfaces

As a simplest case, we first look at non-volatile liquid drops impact on non-wetting surfaces. The drop is composed of 39, 304 tetratomic molecules. Three typical outcomes are observed, shown in Fig. 4.3. The drop shape is depicted in terms of the mean "liquid-vapor interface", the surface on which the fluid density is half of that

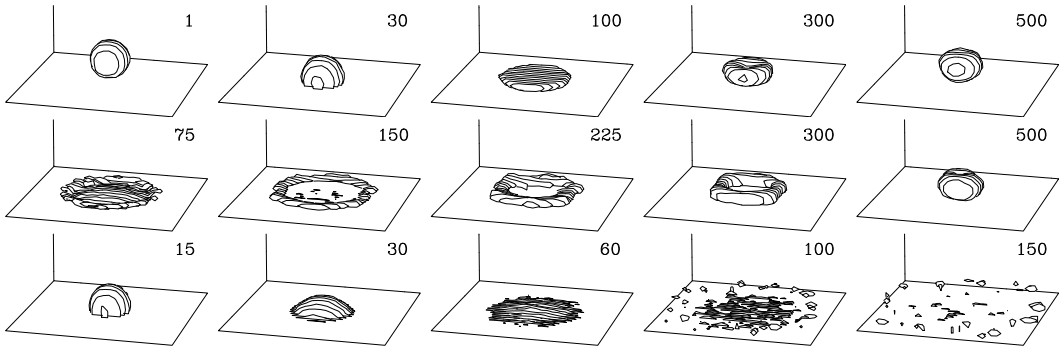

Figure 4.3 : Snapshots of the impact of a non-volatile drop on a non-wetting surface, at velocities 1 (top row), 1.5 (middle row), and 2 σ/τ (bottom row). Each plot depicts the mean interface of the drop at the time indicated in the upper right corner of the frame.

in the original drop interior.

In all cases the drop initially spherical and after impact continues to fall vertically and distorts at first into a hemisphere. When impact velocity $v_0 = 1\sigma/\tau$ or equivalently $Re = 10.3$ and $We = 56.4$, the drop bounces, first expands radially into a flat-topped lamella or pancake with maximum extension at around 100τ, and later curling up at the edges and beginning to withdraw while remaining in contact with the surface. Subsequently, the drop lifts off the wall and continues to contract into a sphere, although the completion of the latter process requires several hundred τ beyond the last frame shown. The bouncing drop contour in cylindrical coordinates at selected times is shown in the first row of Fig. 4.4.

At impact velocity $v_0 = 1.5\sigma/\tau$, or $Re = 15.5$ and $We = 127.0$, the drop also bounces, but at intermediate times develops a remarkable transient toroidal shape before surface tension acts to restore it back to a sphere. The contours are shown in the middle row of Fig. 4.3 and 4.4. The density contours are similar to the lower velocity case up to time 100τ but then show the drop continuing to spread and a

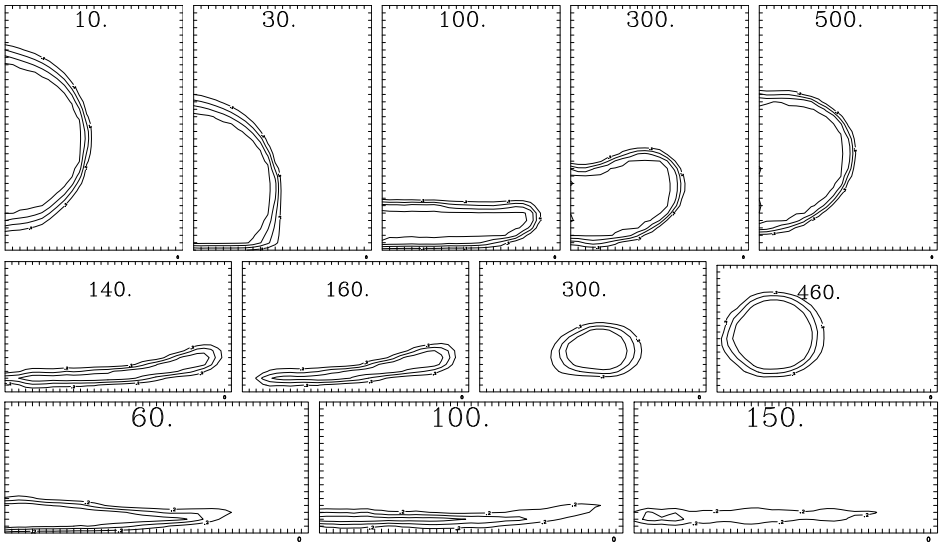

Figure 4.4 : Density contours of impacting drops on non-wetting surfaces in cylindrical coordinates. Each frame is an average over 10τ interval preceding the time indicated on the figures. The initial density at the center of the drop is $0.8m\sigma^{-3}$, the outer contour in each frame represents density 0.2, and the inner contours are spaced by 0.2. Top to bottom: impact velocities 1.0, 1.5 and 2.0 σ/τ.

hole opening at the drop center. To compare with the lower velocity case, here the spreading lamella moves outwards so rapidly as to evacuate the central region about the impact point. Aside from its transience, the toroidal state is somewhat special as it only appears in a narrow velocity range for tetramer drops and the identical state is not observed in volatile dimer system.

At still higher impact velocity $v_0 = 2.0\sigma/\tau$, or $Re = 20.6$ and $We = 226.0$, the thickness and density of the spreading lamella decrease with time, and instead of contracting it develops a splash and eventually evaporates as the drop disintegrates. The mean surface falls apart into isolated liquid regions, implying that lower-density fluid fills the simulation region. A liquid jet is in fact emitted from the edge of the lamella(a prompt splash) around time 30τ, but this is a low-density phenomenon not

evident in these plots and will be illustrated below. At even higher velocity, $3.0\sigma/\tau$, the surface and density plots are similar (on a faster time scale) but the drop seems to disintegrate without a distinct splash phase.

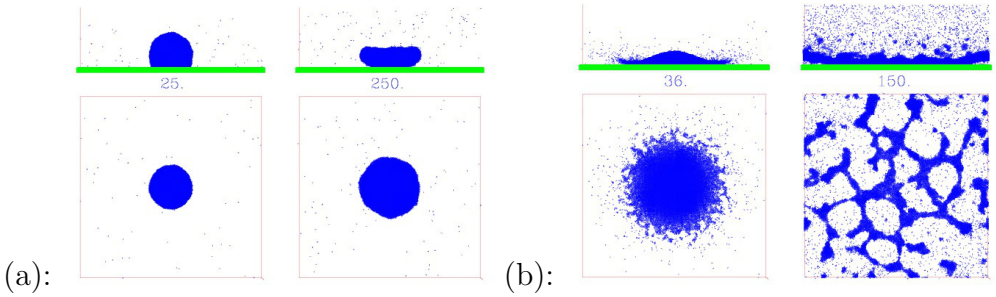

Figure 4.5 : Simultaneous top and side molecular views of an impacting tetramer drop at velocity $1.0\sigma/\tau$(a) and $2.0\sigma/\tau$ (b) at indicated time.

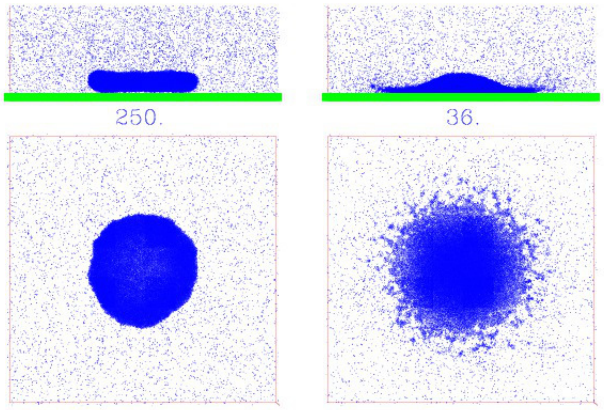

Figure 4.6 : Simultaneous top and side molecular views of an impacting dimer drop at velocity $2.0\sigma/\tau$ at indicated time.

The molecular detail of the impacting drop is shown in Fig. 4.5. At low impact velocity, the amount of vapor slightly increases and the liquid-vapor interface and contact angle are well-defined. Hence the mean interface and density plots accurately capture the shape evolution of the bouncing drop. At twice the impact velocity,

however, we see from Fig. 4.5(b) that as the liquid spreads on the surface, a significant amount of molecules are emitted into the vapor from the drop rim. This is an example of a prompt splash: at time 36τ, there is a crown-like rim rising above the surface and droplets breaking off at roughly regular angular spacing around the edge. Subsequently, the crown collapses as the drop evolves into a single pancake-like lamella, which continues to spread but becomes inhomogeneous and ruptures, meanwhile steadily emitting vapor from its entire surface. Eventually, the liquid reduces to a fragmentary pattern resembling spinodal decomposition, while enough vapor is produced to almost uniformly fill the simulation box. If the impact velocity is even higher, the drop emits vapor from the entire lamella while the edge of the rim has a radially-decreasing density with the little angular variation. The final state in this case (not shown) has a few irregular droplets on the surface and otherwise a low-density fluid filling the simulation box.

We find that the splashing or disintegration behavior is generic, independent of the choice of molecular liquid and the presence or absence of the surrounding vapor. The conclusion is based on repeating these simulations with dimer liquids, with vapor present initially, and mixed tetramer-liquid/dimer-vapor drops with the same initial radius and impact velocities as those above. In all these cases, the drop contour and density fields are very similar to those of tetramers and the only difference lies in the amount of vapor present after impact. In Fig. 4.6 we show the molecular snapshots of the dimer drop at impact velocities 1.0 and $2.0\sigma/\tau$ at two of the same times as the tetramer simulations shown in Fig. 4.5(a), respectively. The dimer drop disintegrates in essentially the same way as the tetramer, and the vapor molecules are simply floating in the background. The threshold We number for splashing/disintegration is $O(100)$, comparing to the experimental transition We number $O(500)$. And this

is why we speak of disintegration rather than splash. The insensitivity to vapor is in contrast to the behavior of larger, millimeter-sized drops, where vapor appears to form a lubrication layer, which causes a splash at sufficiently high velocity. The key difference is that although the vapor density in these simulations is similar to that at room conditions, the amount of vapor lying beneath a falling 12 nm drop is very small− tens of molecules, and insufficient to show any significant hydrodynamics behavior. When a drop impacts the surface, these vapor molecules are either adsorbed by the drop or pushed aside but have little effect on the drop splash.

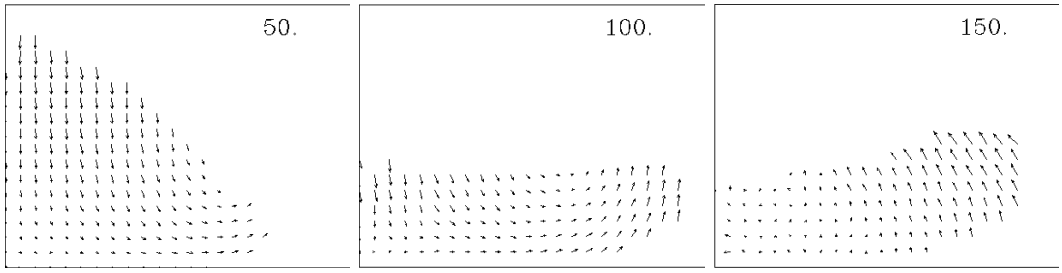

Figure 4.7 : Cylindrical averaged velocity field for non-volatile drop impacting on non-wetting surface at $v_0 = 1.0\sigma/\tau$.

The velocity field of the spreading drop is shown in Fig. 4.7. At time 50τ, there is a roughly hyperbolic flow in which the original bottom of the drop is forced outwards while the upper half is still moving downwards. The radially outwards flow produces the spreading lamella. At time 100τ, the radial motion at the edge of the rim has ceased and the rim is bending upwards, while the top of the drop continues to fall. At time 150τ, the velocities in the center of the drop become very small, while a faster contraction to a sphere is underway at the rim. The same sequence is observed for all bouncing drop cases, whereas when the surface is wetting the velocities simply decay to small random fluctuations when the initial rapid-spreading stage ends. In

splashes or disintegrations, the velocity field is simply radially outwards at later times before decaying away. In these figures, the vapor region is not shown because it contains too few molecules for averaging to produce a robust signal above the statistical fluctuations.

4.3.2 Wettable Surfaces

Drop spreading on wettable surfaces is considered here. A direct comparison between MD and LB simulations on the (azimuthally-averaged) contours of spreading drops at $Re = 24$ and $We = 128$ at two contact angles is given in Fig. 4.8. The drop shapes are very similar at the earlier times after impact, for times below $t^* = R_0/v_0$, and begin to differ afterwards although there are no gross differences. The shape very near the contact line, however, is somewhat different throughout the process, which presumably reflects differences in the modeling of the solid/liquid interactions.

For a more quantitative comparison, we consider the variation of drop height and radius with time. First, in Fig. 4.9 we plot the height of the drop in the two methods for four impact velocities at a 50° contact angle. Lower angles behave somewhat similarly, but there are substantial discrepancies in strongly non-wetting case. In the figures, the drop height h is scaled by the initial drop radius R_0 and time is scaled (inertially) by the free-space transit time across a radius, $t^* = R_0/v_0$. Generally, the height decreases linearly until impact, then less rapidly as the drop is squeezed against the solid, and then a weak nearly-linear rise as the drop re-expands upwards to its final state. The two methods are in reasonable agreement at the lower impact speeds but do not agree at higher Re. Next, we compare the results for different contact angles at a fixed impact velocity $Re = 24$ and $We = 128$. We see in Fig. 4.10 that as a function of contact angle, the $h(t)$ curves for the two methods are similar

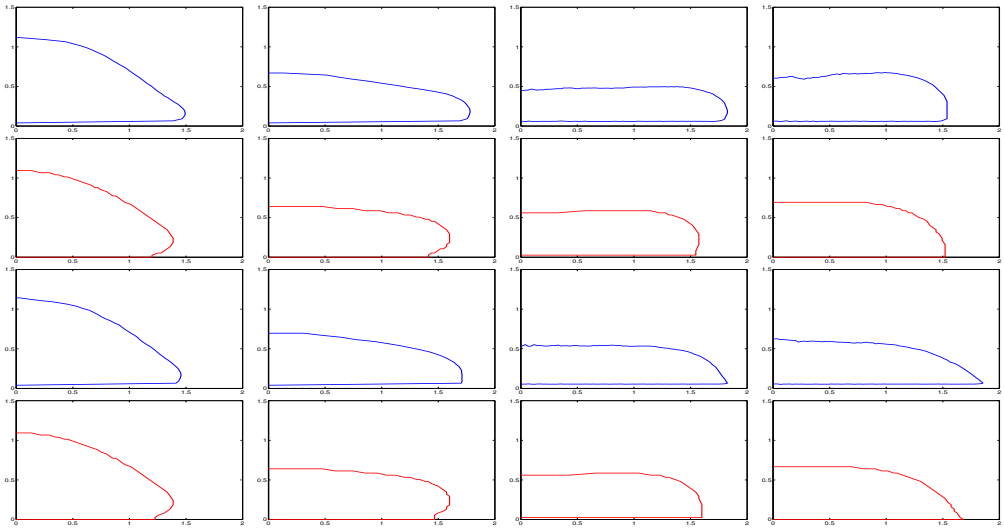

Figure 4.8 : Azimuthally-averaged drop shapes during impact for $Re = 24$ and $We = 128$. First row: MD at $\theta = 96°$. Second row: LB at $\theta = 96°$. Third row: MD at $\theta = 50°$. Forth row: LB at $\theta = 50°$. From left to right: $t/t^* = 1, 2, 4, 8$. The length unit is the initial drop radius R_0 and the time unit is $t^* = R_0/u_0$.

for low contact angles but deviate as θ increases and the wettability decreases. For a completely non-wetting surface ($\theta = 180°$) where the disagreement is largest, the MD drops simulated here have no attractive interactions at all with the solid surface and tend to float off unless there is a significant impact velocity, whereas this property is absent in the LB case. Note that the scaling behavior in these results is rather erratic: the curves for different impact velocities overlap only at early times, while those for different contact angle in wetting and partially-wetting cases form a nearly-universal curve in the LB case but do so only approximately in MD.

The variation of drop radius with time is consistent with this behavior. Since the drop shapes are irregular and not simple functions there is no unique characterization of their radius, so we have examined the two obvious choices – the maximum value R_m, corresponding to the drop size as projected from above, and the contact radius of

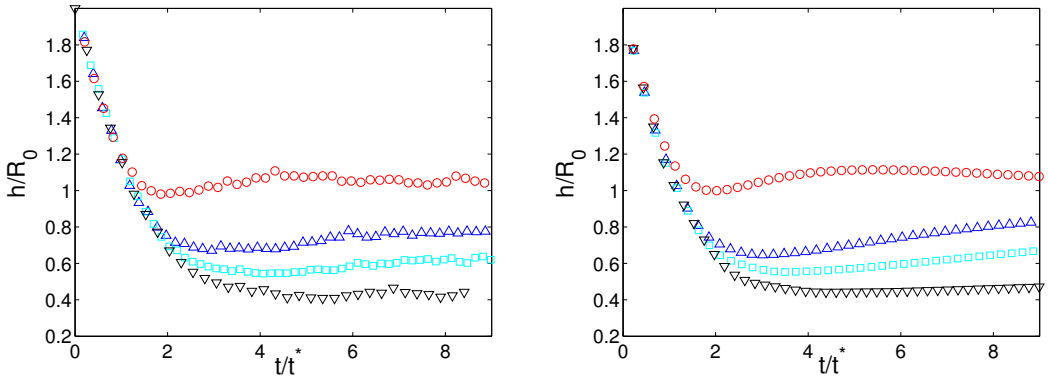

Figure 4.9 : Time dependence of the drop height after impact for various impact speeds at contact angle 50°. Left: MD, Right: LB. ○: Re=10; △: Re=19; □: Re=23.7; ▽: Re=35.6.

liquid on the surface R_c, which might be viewed from below in suitable experiments on transparent solids. The two radii are most sensitive to different physical effects. The maximum radius begins at the initial value R_0 at contact, increases due to inertia, slows due to viscosity, and may withdraw due to surface tension, although this depends on the surface properties. The contact radius is very sensitive to the liquid/solid interaction, and tends to be less than the maximum radius on nonwetting surfaces. It is difficult to anticipate the relative values of radii on partially-wetting surfaces and crossovers may occur. The dynamic contact angle itself is generally quite different from the equilibrium angle, since it starts at 180° at impact and tends to relax to the equilibrium angle when spreading halts.

We begin with Fig. 4.11 which shows the variation of the two radii with velocity for a weakly-wetting surface at contact angle 50°. In the MD case drops at all impact velocities spread and then contract, consistent with approximate incompressibility and the previous observation that the drop height rises after impact. In microscopic terms, the contraction results from weak solid/liquid attraction being overcome by

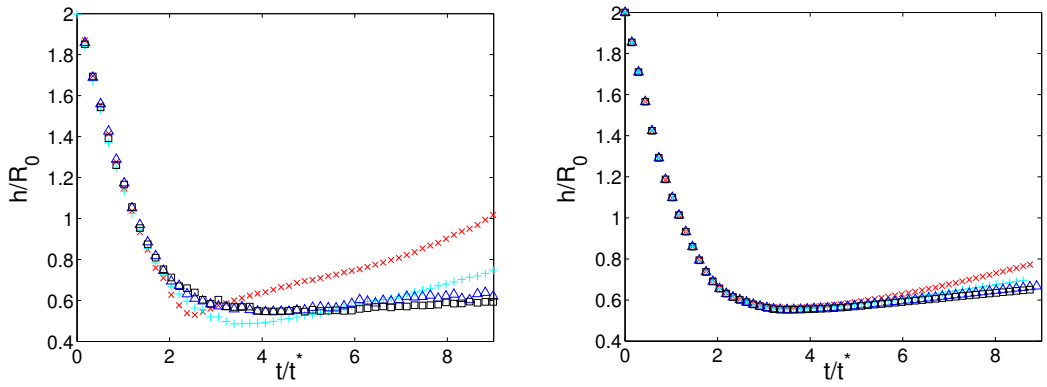

Figure 4.10 : Time dependence of the drop height after impact for various wettabilities. at $Re = 24$. Left: MD; Right: LB. Contact angle: ○: $\theta = 180°$; □: $\theta = 96°$; △: $\theta = 50°$; +: $\theta = 0°$.

liquid/vapor surface tension, whereas in continuum terms the inertially-driven spreading (Fig 4.8) drives the contact angle to a value above the equilibrium angle and the drop withdraws to return to the proper value. In contrast, on a completely wettable surface, both radii increase indefinitely as the drop attempts to cover the surface, although rather slowly after initial impact on the time scale of these simulations. In general, a receding stage may or may not be observed, depending on the surface wettability. In the LB case, a noticeable withdrawal of the drop after initial spreading is seen only in the maximum radius, and there the effect is rather weaker than in MD. The contact radius hardly withdraws at all, suggesting differences in the LB and MD treatment of surface interactions. Furthermore, as in the height variation, there is a rough agreement between the two methods at least at early times only at lower impact velocities.

A possible source of discrepancy at higher velocities is in the treatment of slip. In MD, the contact line motion is that of the atoms in that region, as controlled by the interplay of interactions with the solid and with the rest of the liquid. It is well known

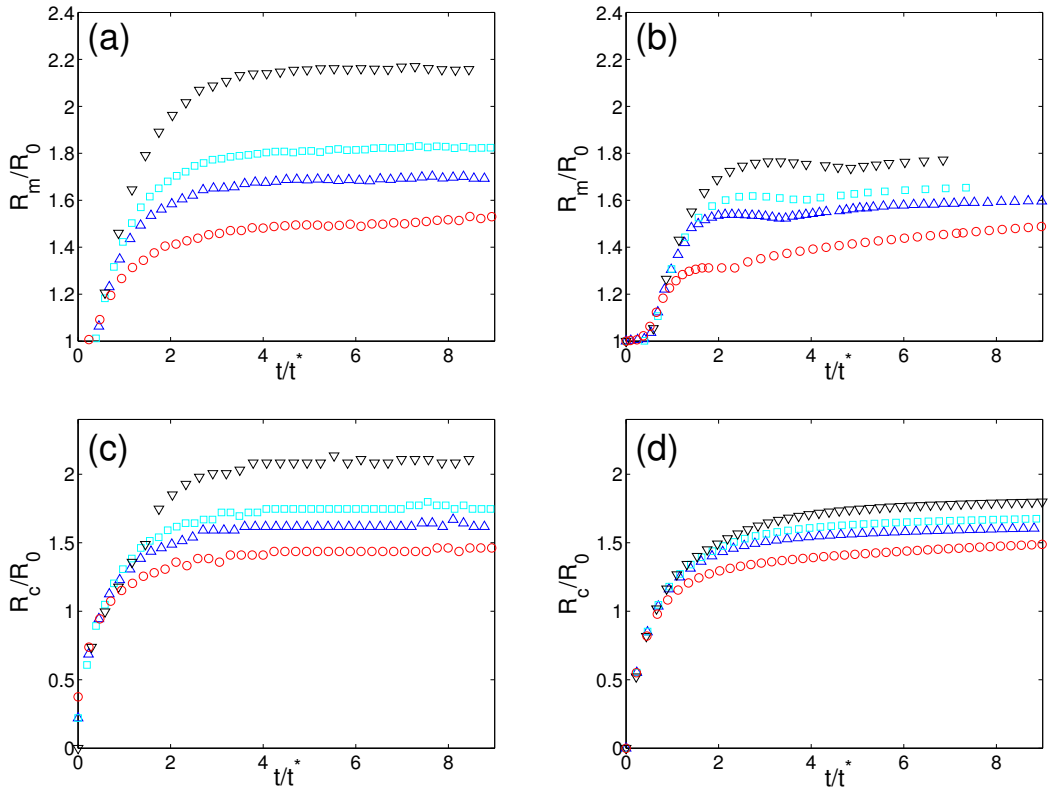

Figure 4.11 : Time dependence of the drop radii after impact, for fixed equilibrium contact angle (50°) and various impact speeds. (a) R_m in MD; (b) R_m in LB; (c) R_c in MD; (d) R_c in LB. ○: Re=10; △: Re=19; □: Re=23.7; ▽: Re=35.6.

that the resulting slip length increases systematically as the fluid velocity increases and as wettability decreases. In the highest-velocity impact ($Re = 35.6$) substantial slip is observed on non-wetting surfaces [46] which promotes rapid spreading. In the LB method, the surface interactions are constructed so as to produce a non-slip boundary condition for the velocity, but in fact the motion of the contact line is due to diffusion of the Cahn-Hilliard concentration field. (It has been shown [**?**] that reducing interfacial thickness while keeping the mobility constant gives the sharp interface limit with a diffusion length scale corresponding to the slip length, and in

agreement with the asymptotic analysis of Cox [**?**]). The resulting value of the contact line velocity differs in the two methods, as illustrated in Fig. 4.12. In both models, the contact line velocity is obtained from the time-dependence of the concentration midpoint value in the row of bins (sampling and computational in the MD and LB methods, respectively). Except at early times, the contact line velocity is somewhat larger in MD, which enhances the spreading. Note also the anomalous behavior in MD in the nonwetting 180° case, which shows distinctly more slip than for the other contact angles.

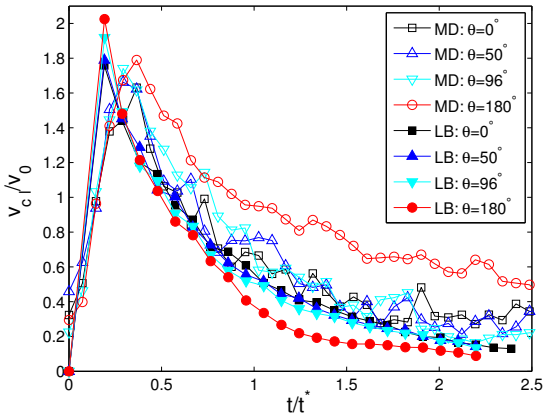

Figure 4.12 : Time-dependence of the contact line velocity for unit impact velocity, comparing MD and LB results for different contact angles as indicated in the inset.

There are also distinctions in the drop shapes between the two methods, arising from the fact that the MD simulations operate near the boundary of the splashing regime whereas the LB calculations produce smooth and stable drop shapes in these conditions. At the higher Reynolds numbers, the MD drops exhibit features which might be thought of a precursors to splashing: an irregular edge and transient holes appear in the spreading lamella during the expansion stage, as shown in Fig.4.13.

Furthermore, the drop at $Re = 36$ on a nonwetting surface does in fact splash, and the results for this case in the figures above are restricted to times before the splash.

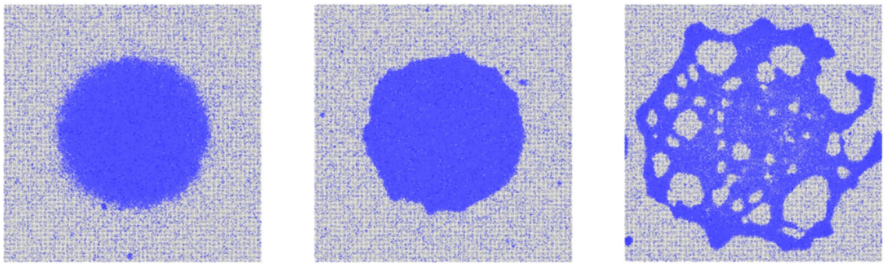

Figure 4.13 : Top view of the drop shape at $Re = 36$ and $We = 288$ for different wettabilities at $t = 6t^*$. Left to right: $\theta = 0°$, $\theta = 96°$ and $\theta = 180°$.

A second source of the discrepancy between the MD and LB calculations as impact velocity increases is the effect of Mach number. At $Re = 10$, in these MD simulations the Mach number $Ma \approx 0.1$ [46], which at first glance is worrisome for comparisons to normal liquids in typical impact experiments and simulations, but from the average density output of the calculation (the volume enclosed by the interface contours) we estimate that the maximum variation in drop volume is at most only about 2% – see Fig 10. However, the Mach number increases linearly with impact velocity and correspondingly the volume variation rises to about 7% when Ma = 0.24, which is a cause for concern. In the LB calculations, the Mach number may be varied to some degree to address this point, but beyond $Ma \approx 0.1$ the calculation fails to converge properly. However, if we extrapolate the LB calculations to the values of Ma relevant to the MD simulations, then as shown in Fig. 4.14 the disagreement in maximum spreading radius is significantly reduced.

The wettability dependency of the spreading radii is shown in Fig. 4.15. Note the anomalous behavior of the fully non-wetting $\theta = 180°$ case: except at the earliest

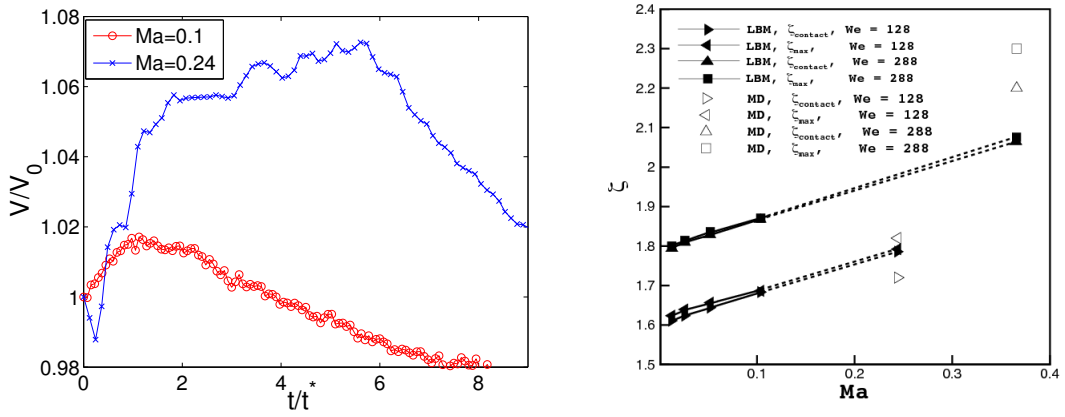

Figure 4.14 : Mach number effects in the LB calculations. Left: volume change during impact. Right: variation of the maximum spreading factor with Ma. The curves are computed for $Ma \leq 1$ and linearly extrapolated to larger values.

times, the variation of the radii is entirely different from the other cases where there is some degree of wetting. Furthermore, the contact radius varies erratically in the MD plot, while the maximum radius grows very rapidly and then decays very rapidly, corresponding to a drop which is barely in contact with the solid surface while rapidly expanding and then contracting from a lamella state. The LB results partly echo this behavior, although contact with the solid is maintained so that R_c varies smoothly and time-dependence of R_m is is less rapid. In the other cases, there is approximate agreement between the two methods and some uniform scaling behavior at early times up to 2-3t^* suggesting that inertia dominates the spreading dynamics there. Notice that the radii grow at long times in the two wetting cases ($\theta = 0°$ and $50°$) but decay after initial growth in the non-wetting case ($\theta = 90°$ and $180°$). Furthermore, the scaled time at which the two radii reach their maximum values in non-wetting situations is in the range 1.8-3.9 in Figs. 4.11 and 4.15, consistent with the data of Dong et al. [22] (note that a different definition of scaled time is used in this paper).

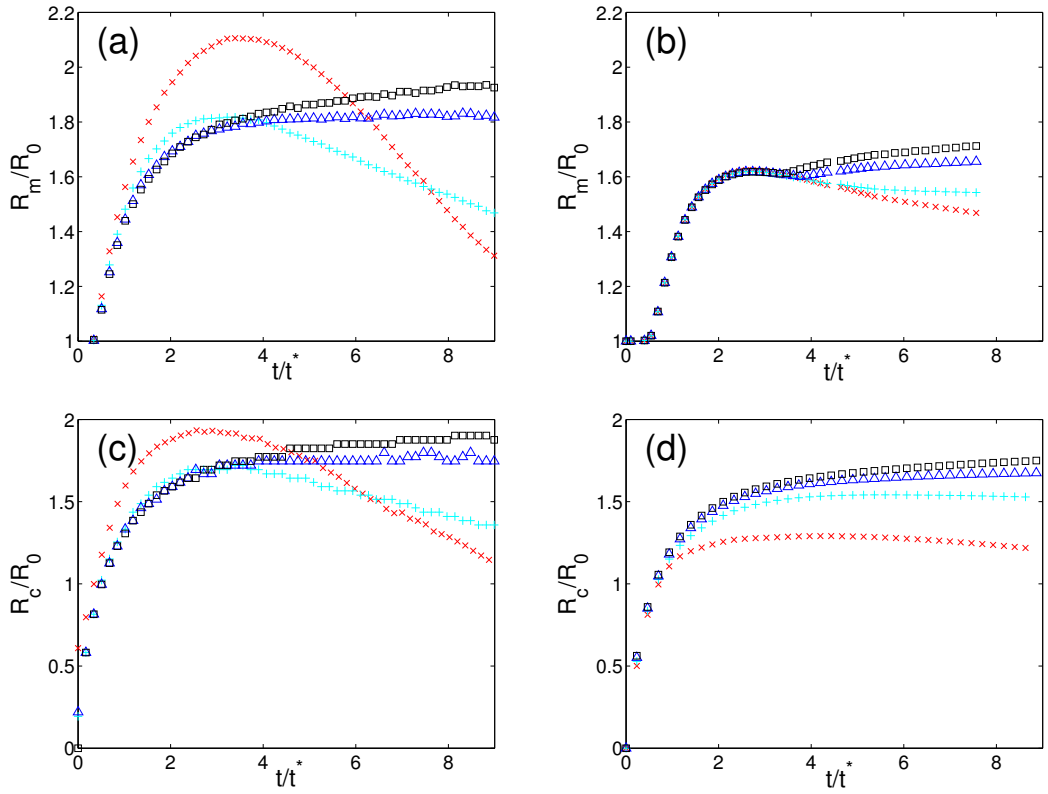

Figure 4.15 : Variation of spreading radii with wettability at $Re = 24$ and $We = 128$. (a) Maximum radius from MD; (b) Maximum radius from LB; (c) Contact radius from MD; (d) Contact radius from LB. $\times$: $\theta = 180°$; $+$: $\theta = 96°$; $\triangle$: $\theta = 50°$; $\square$: $\theta = 0°$.

Lastly, we compare the present simulations to results in the literature. There are direct experimental results on hydrophobic surfaces by Clanet *et al.* [85], which indicate that the We number dependency of the maximum spreading factor is $\xi_{max} \sim We^{1/4}$ [85], where ξ_{max} is the maximum spreading diameter during impact scaled by the initial drop diameter D_0. An empirical extrapolation from experiments by Scheller and Bousfield [86], a combination of data and theory by Roisman [87] and models based on energy balance arguments by Pasandideh-Fard *et al.* extrapolated to the fully hydrophobic case show slightly different behavior, a scaling law with a

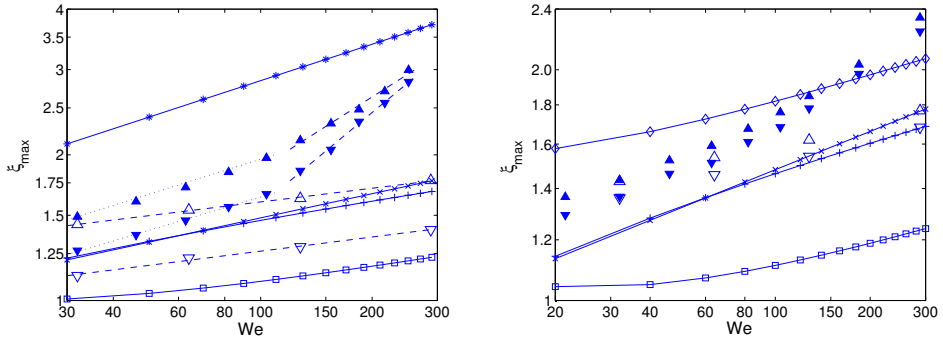

Figure 4.16 : We number dependency of maximum spreading factor, for contact angles left: 180° and right: 96°. MD (filled) and LB results (open triangles): ▲ or △: ξ_{max} calculated from D_m; ▼ or ▽: ξ_{max} calculated from D_c. Experiments and extrapolations thereof: -∗-: Clanet *et al.* [85]; -×-: Scheller and Bousfield [86]; -+-: Roisman [87]; -□-: Pasandideh-Fard *et al.* [88]; -◇-: Chandra and Avedisian [89].

different prefactor and a smaller exponent. Our MD results Fig. 4.16 lie in between the data, and exhibit qualitatively consistent behavior: we find almost the same scaling exponent (0.24) at lower We, where the calculation is in the best correspondence to experiment (lower Ma) but a more rapid variation with exponent around 0.5 at higher impact velocities: For $We > 120$, ξ_{max} scales as $We^{0.49}$ for D_m and $We^{0.56}$ for D_c (the two dashed lines in the figure). At still higher We the spreading lamella in the MD simulations begins to break up at its edges (see Fig. 4.13), and the results there are uncertain. The LB results instead vary as a single power-law which is bracketed by the experimental points and overlaps the MD points at low We. For the weakly wetting case $\theta = 96°$ there are only extrapolated or theoretical previous results, which again have some spread. The MD simulations again show distinct power-laws at low and high We, and are only in rough agreement with previous work at the higher We values. The LB points again have uniform power-law behavior and have the same relation to the other data as in the nonwetting case.

4.4 Nano Drop Impacts Textured Surfaces

4.4.1 Surfaces With A Cross Pattern

As a prototypical example of a heterogeneous surface we consider drop impact on a surface with a cross-shaped region of one wettability superposed on a background with a different value. Since different regions of the edge of a drop on a cross pattern have different contact angles, its motion will no longer be radially symmetric and interesting spreading patterns result. The surface is indicated schematically in Fig. 4.17, where two complimentary cases are shown: a wettable cross pattern on a nonwetting substrate (case A), and a nonwetting cross pattern with a wettable background (case B). The width of the cross b is set to $R_0/2$, and the drop impact is centered at the middle of the cross, so that the drop necessarily covers regions of both wettabilities. The equilibrium contact angles inside and outside the cross are denoted as θ_i and θ_o, respectively, and the specific values used are 73° and 180° for wetting and nonwetting regions, respectively. In MD simulations, we treat the wall atoms in different regions as different species and set the liquid-wall interaction strength c so as to produce the appropriate contact angle. In LB simulations, the contact angles are direct inputs and we simply assign different θ's to the different wall region.

A similar problem was previously studied numerically by Schwartz *et al.* [52, 53], although the configuration included a thin wetting layer covering the substrate to avoid a no-slip singularity in the lubrication approximation calculation. Various drop motions resulted, including spreading, migration and drop breakup, but the differences in assumptions preclude a detailed comparison with the present work.

Snapshots of the two simulations for $Re = 24$ and $We = 128$ for the two patterns are given in Fig. 4.18. In the MD simulations, during the spreading stage after impact,

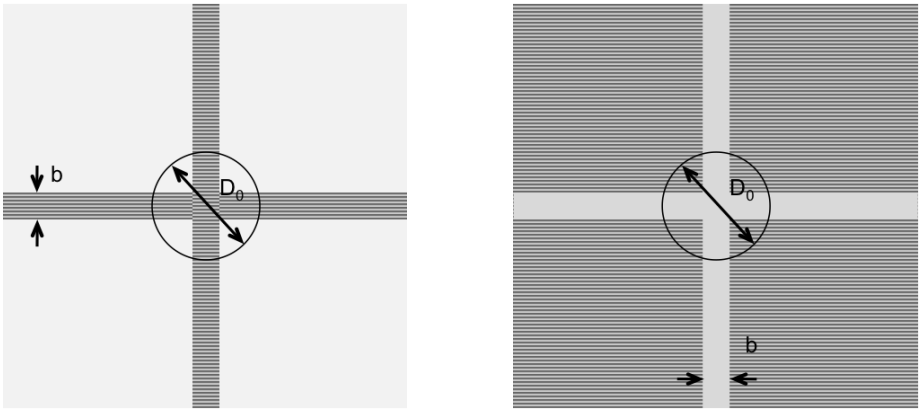

Figure 4.17 : Illustration of the cross patterns of wettability. Left: case A; Right: case B. Dark and light regions are wettable and nonwetting, respectively.

for $t \leq 2t^*$ in the figure, the drop spreads more slowly on wetting than on nonwetting surfaces, resulting in a rectangular shape in case A and a diamond shape in case B. When the drop recedes, it likewise does so more slowly on the wetting region, leaving a squarish shape with nodes along the wetting stripes in case A and an approximate disc with indentations along the cross in case B. The corresponding LB simulation results show a much smoother drop shape at all times, as well as a much weaker variation of the drop radius with time, but the shape are qualitatively similar in terms of protuberances and indentations along the cross.

To quantify the shape for this pattern geometry, we measure the spreading radii of the drop along the four axes and four diagonal (45°) directions. Averaging along symmetry directions yields two radii, one along the axes (the cross) and the other along the diagonals (outside the cross). The time evolution of the two spreading radii can be compared to that on homogeneous surfaces with the same wettabilities, as shown in both cases, the early stage of spreading are identical to that on a homogeneous wall, but differences occur when the drops recede. In case A in the MD

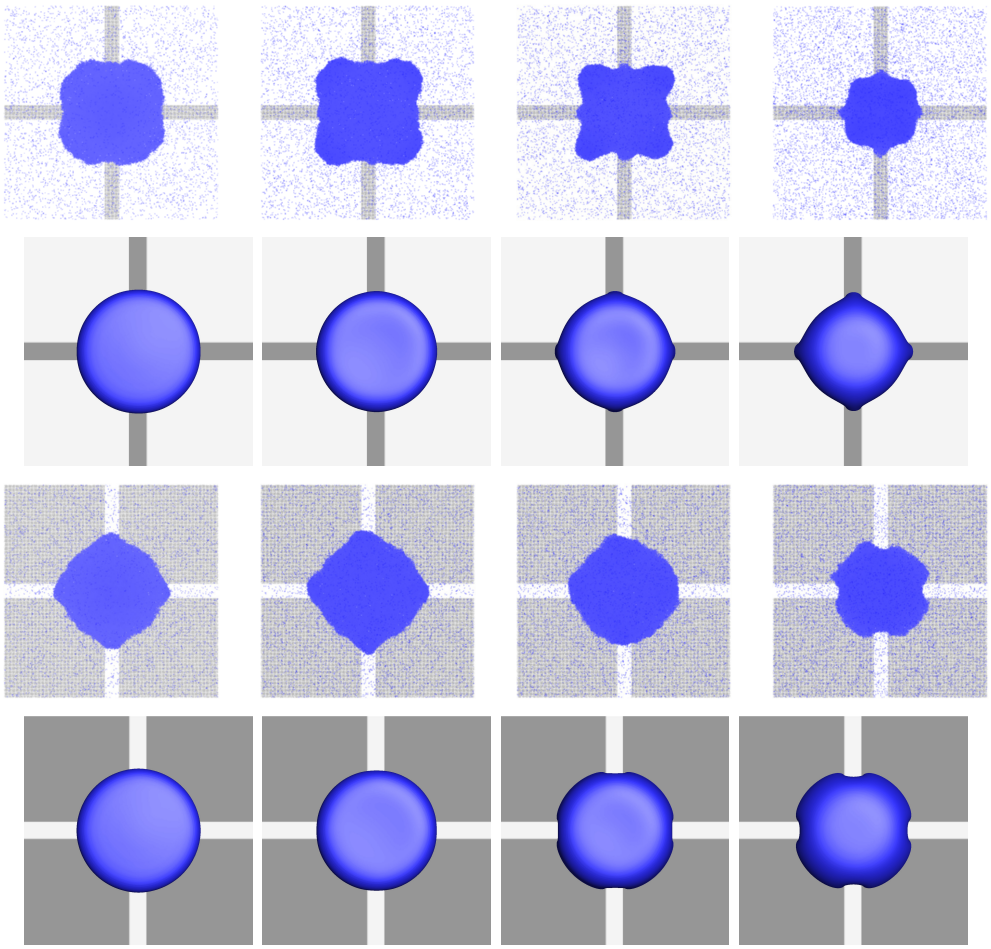

Figure 4.18 : Snapshots of the top view of the drop shape during impact at $Re = 24$ and $We = 128$. First row: MD for case A; Second row: LB for case A; Third row: MD for case B; Fourth row LB for case B. left to right: $t/t^* = 2, 4, 6, 10$.

simulations, the drop recedes more rapidly along the wettable cross then for a homogeneously wettable surface, because it is puller inwards by the rapidly-receding fluid in the nonwettable diagonal regions. In the corresponding LB figures the radii hardly differ until times around $3t^*$, and then the behavior on the two regions is close to their respective homogeneous cases. In case B, the MD fluid along the nonwetting cross is slightly slowed by the slow-moving fluid in the wetting diagonals, and the

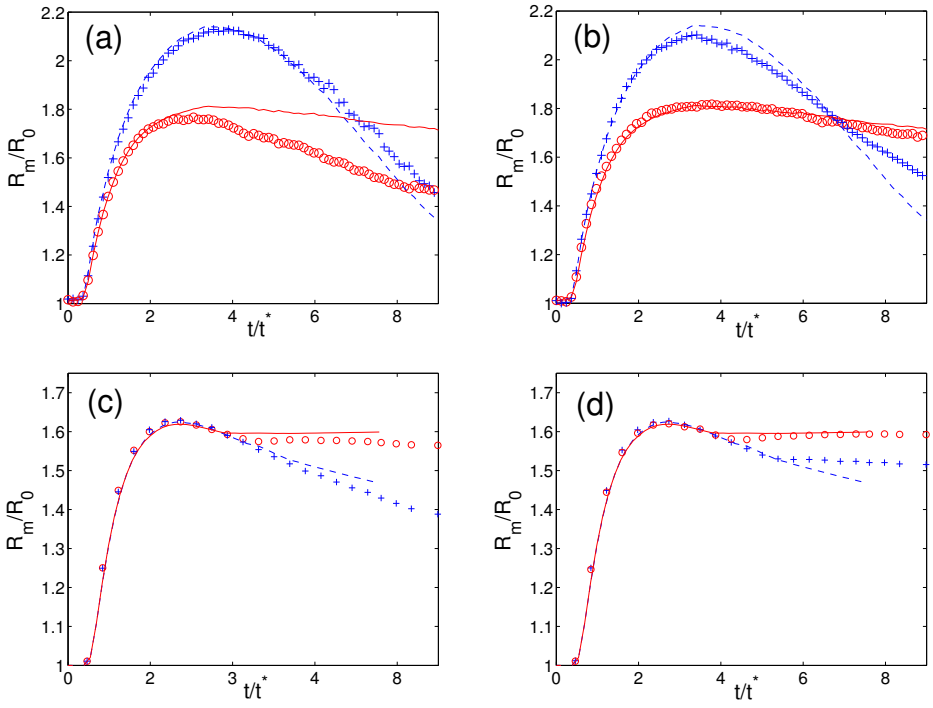

Figure 4.19 : Drop spreading radius on a cross patterned surface with $Re = 24$ and $We = 128$. (a) Case "A" in MD; (b) Case "B" in MD; (c) Case "A" in LB; (d) Case "B" in LB. ○: wetting pattern; –: uniform wettable surface; ×: nonwetting pattern; - -: uniform nonwetting surface. Case "A": ○: along axes and ×: along diagonals; Case "B": ○: along diagonals and ×: along axes.

effect is weaker because the amount of fluid there is less. Here, again the LB results differ from MD and resemble case A.

Interesting behavior occurs if we consider higher impact velocity, $Re = 36$, which was previously shown to produce a splash on a homogeneous nonwetting surface [46] but, as discussed in the previous section, simply deforms the drop on wettable surfaces. On the cross patterns, the result is a mixture of these behaviors: snapshots at time $t = 2t^*$ are given in Fig. 4.20. In case A most of the the solid beneath the drop is nonwetting, to an increasing degree as the drop spreads, and the behavior in the

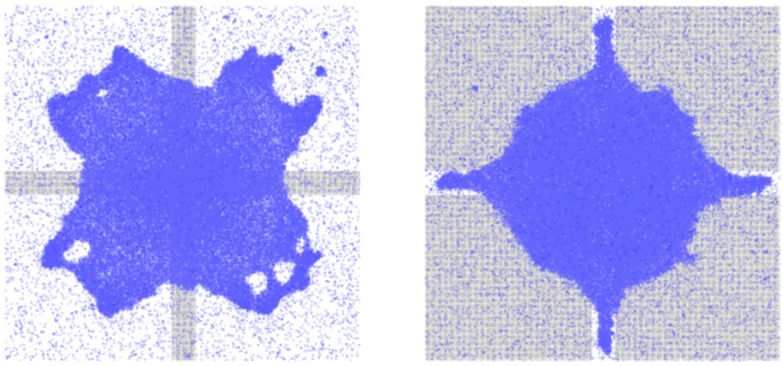

Figure 4.20 : Higher velocity impact in MD. Top view of the drop shape at time $t = 2t^*$ at $Re = 36$ and $We = 228$. Left: case "A"; Right: case "B". Dark region is wetting and light region is nonwetting.

four diagonal nonwetting directions away from the cross pattern is splash-like. Along the cross the motion is slower with a stable interface, and these segments of the drop surface act to stabilize the entire drop, somewhat mitigating the unstable splashing behavior on the diagonals. The result is an irregular pattern with holes and satellite drops, but far less disordered as that on a fully nonwetting surface. Because the drop breaks up, it does not contract at later times. In case B the surface is reversed and most of the drop spreads along a wetting surface which is stable at this Re. The result is a spreading pattern with rapidly moving fingers along the nonwetting cross axes which break up at later times and a slower and slightly irregular circular edge advancing in the diagonal directions.

The cross-patterned surfaces provide a vivid illustration of the difference between LB and MD in fully nonwetting cases. We consider an impact at "zero velocity:" a drop is placed at rest just within interaction range of the surface (separation less than the cutoff distance 2.5σ of the Lennard-Jones interaction in MD) and allowed

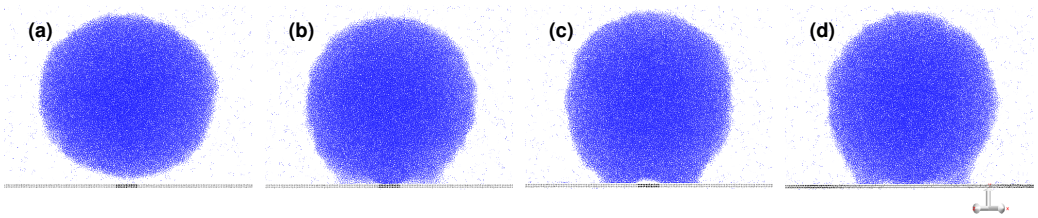

Figure 4.21 : Static drop shapes above a cross pattern. (a) Initial shape of a drop near the surface. (b) Equilibrium shape in case A. (c) Equilibrium shape in case B, viewed along the x-axis. (d) Equilibrium shape in case B, viewed along a 45° diagonal.

to move freely. The drop is drawn to the surface by the attraction from the wettable regions, but the final state depends on the pattern. Side views of the initial and final drop shapes (which stabilize after 400τ) are shown in Fig. 4.21. In case A the drop is attracted to the cross and nearby fluid molecules approach the solid closely. Fluid above the nonwetting solid regions would tend to float away, but the result would be a significant distortion in the drop shape and surface tension suppresses this. The resulting drop is a near-sphere, slightly flattened at the surface. In case B the cross repels nearby fluid molecules but the diagonal regions attract them, and since there is more surface along the diagonals the drop is still bound to the solid. However, as seen in the figure, a cavity opens above the cross. In contrast, LB simulations of a static drop in case B do not exhibit a cavity. Evidently, there are differences in the surface interactions between the two simulation methods: the sharp distinction between attracting and non-attracting surface atoms in MD is not entirely equivalent to a spatial variation of the boundary coefficients in the Cahn-Hilliard potential in LB.

4.4.2 Pillared Surfaces

Realistic solid surfaces are not often atomically smooth, as in the examples discussed above, and a variation in height is the general case. A weak variation would presumably produce local variations in shape, while strong variations would lead to pinning effects, and a rather extensive study would be needed to explore the range of fluctuation amplitudes and correlation lengths present in different materials. Here we focus on the effects of periodic pillar arrays on spreading, since such surfaces are both practically relevant because they can exhibit superhydrophobic behavior and theoretically interesting because of the interplay of Cassie and Wentzel states [90, 91] which have different degrees of liquid filling in the gaps between the pillars. In fact, some earlier MD simulations [92, 93] have specifically explored the transitions between the various filled states, but only for drops initially at rest.

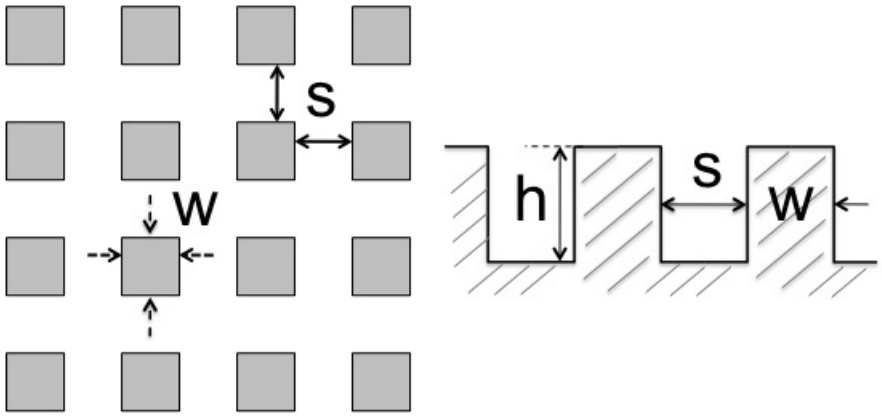

Figure 4.22 : Geometry of pillared array surfaces. Left: top view, where grey squares indicate the tops of the pillars. Right: side view, where the solid is shadowed. The pillars have width w and height h and are separated by a gap s.

The geometry is given in Fig. 4.22, and consists of square pillars of width w and height h, arrayed on a square. We vary the pillar density by changing the spacing ratio

$\rho_p = w/(w+s)$ while keeping $w+s \simeq 0.2R_0$. The contact area is awkward to quantify in simulations here, since liquid may coat part of a pillar, and difficult to measure experimentally for the same reason, so we consider the projected or maximum radius R_m only.

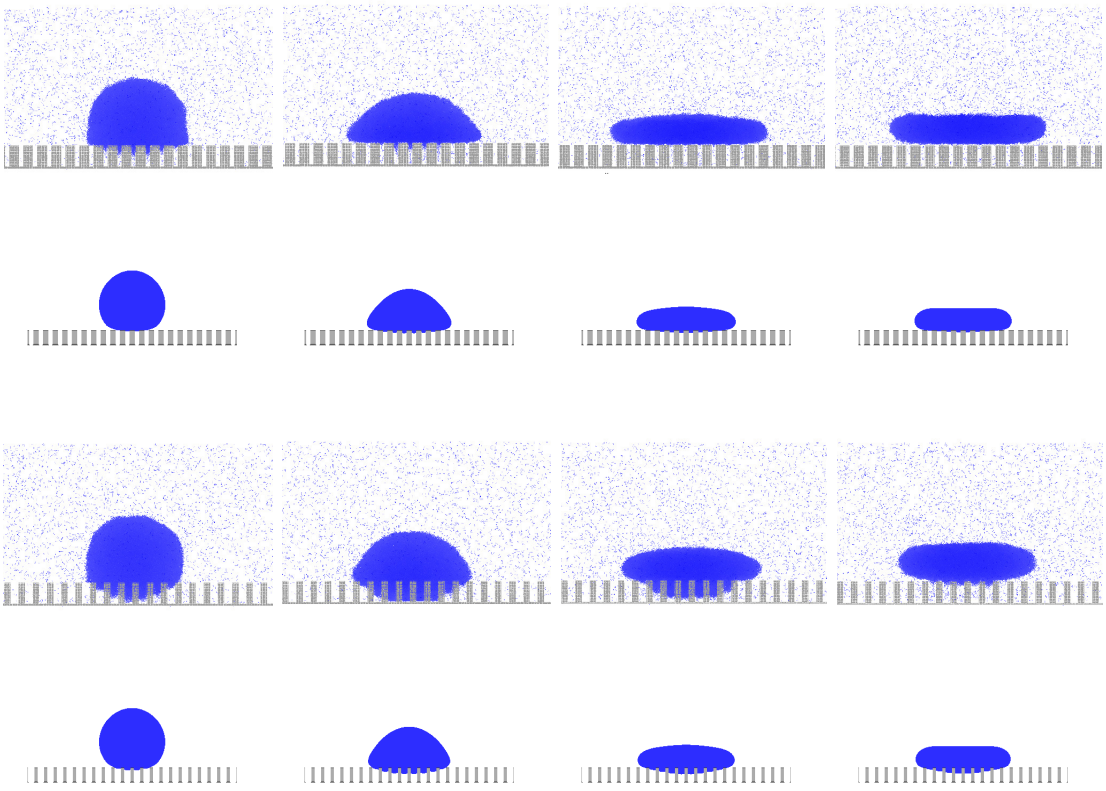

Figure 4.23 : Side views of spreading drops on nonwetting pillars $Re = 17$. First row: $\rho_p = 5/8$ in MD; Second row: $\rho_p = 5/8$ in LB; Third row: $\rho_p = 3/8$ in MD; Bottom row: $\rho_p = 3/8$ in LB. Time from left to right: $t/t^* = 0.5, 1, 2, 3$.

The pillar spacing has a strong effect on drop behavior, as shown in Fig. 4.23. For non-wetting pillars, when $\rho_p = 5/8$, the gap between pillars is small and the pressure in the drop is too small to overcome the capillary pressure necessary for the fluid to

invade a narrow channel, giving a Cassie state of fluid advancing atop the pillars. If the pillar are more widely spaced, at $\rho_p = 3/8$, the gaps are wide enough to be invaded, resulting in a partially-filled state. Here, because the surface is nonwetting, the drop will eventually evacuate the gaps but this process delays the advance of the drop and leads to considerably smaller spreading diameters. Note that gap-filling is rather more rapid in the MD case.

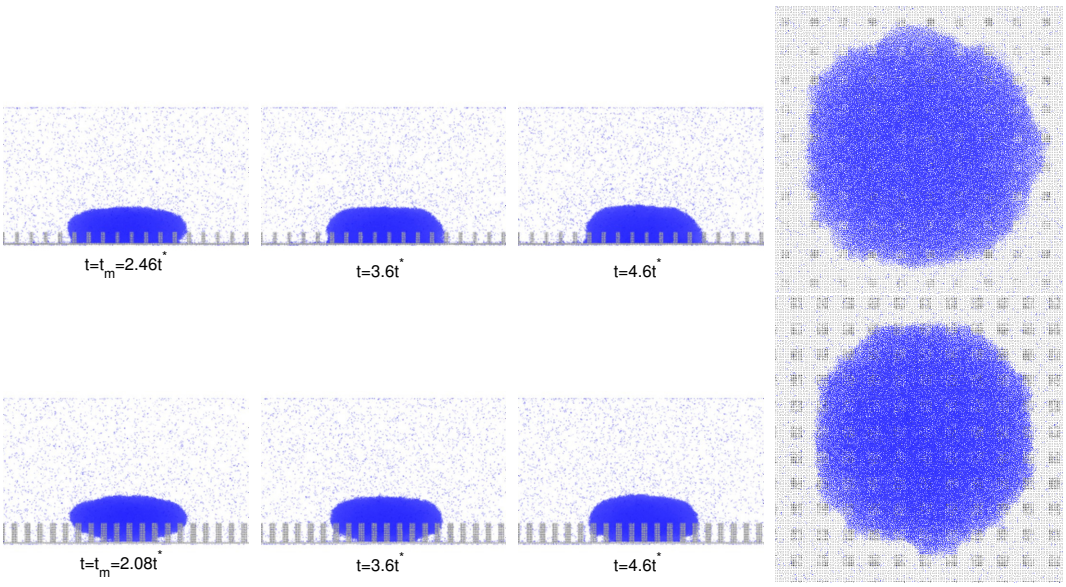

Figure 4.24 : Late-time evolution of drop shape on wettable pillars with $\theta = 50°$ at $Re = 17$ and $We = 63$. Top row: $\rho_p = 2/9$ and $h = 0.16R_0$; bottom row: $\rho_p = 3/8$ and $h = 0.3r_0$. t_m is when the drop reaches its maximum deformation and the last column is the top view at $t = 4.6t^*$.

If instead the solid surface is wetting, the gaps are always fully invaded and produce a Wentzel state, but the time-dependent dynamics depends on the geometry. In Fig. 4.24, we show the drop states at the time of maximum spreading for a partially wetting surface with equilibrium contact angle 50° and two choices of pillar shape. If the pillars are shallow and widely spaced the drop first deforms to its maximum

extension with a dynamic contact angle greater than 90°, filling the gaps as it spreads, and then gradually increases its contact area while decreasing the contact angle as the gap filling at the edge of the drop adjusts. However, if the pillars are deep and slightly more densely packed, the gaps are incompletely filled during spreading, and as they fill afterwards the drop withdraws to provide the necessary fluid and lowers R_m. The top view of the drop at late stage of impact shows how the surface irregularities perturb the shape of the lamella: the fluid is attracted to the pillars and the rim of the drop is flattened parallel to the axes.

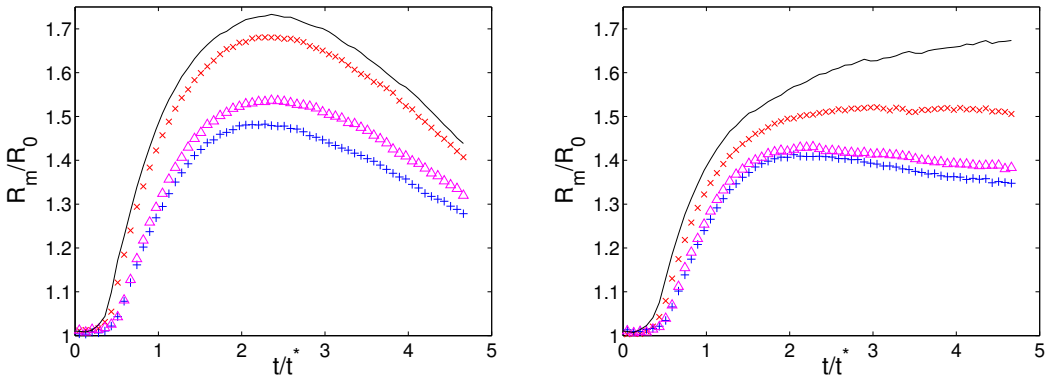

Figure 4.25 : Maximum drop spreading radius for impact on non- and partially-wetting surface for pillars of various sizes at $Re = 17$ and $We = 63$. Left: $\theta = 180°$; Right: $\theta = 180°$. $\times$: $\rho_p = 5/8$; $+$: $\rho_p = 3/8$; $\triangle$: $\rho_p = 3/8$ with shallower depth $h/D_0 = 0.09$; $-$: $\rho_p = 1$(flat surface).

For the quantitative time dependence, first in Figs. 4.25, we consider the effects of varying the pillar shape, for two choices of wettability. Unsurprisingly, in both cases the spreading rates and maximum diameters on a pillared surface is less than those of a flat one. In the nonwetting case, the drop always expands and then contracts, and increasing the pillar areal density and decreasing the pillar depth both promote spreading. In the partially-wetting case the relative amount of spreading exhibits the

same trend as the pillar geometry varies, but in the presence of the pillars the drops halt or contract at later times. On a flat surface this liquid would spread until the contact angle reaches the equilibrium value of 50°, at times beyond those simulated, but here the maximum spreading radius is less because liquid is "lost" in starting to fill the gaps, and the late-time decay results as the gaps fill completely.

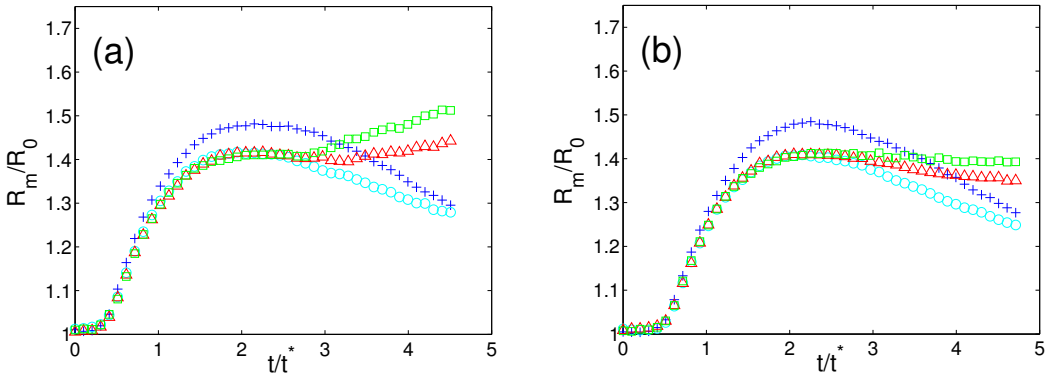

Figure 4.26 : Drop spreading radius on pillars of various wettabilities with $Re = 17$ and $We = 63$. (a) $\rho_p = 2/9$ and depth $0.16R_0$; (b) $\rho_p = 3/8$ and depth $0.3R_0$. +: $\theta = 180°$; ○: $\theta = 96°$; △: $\theta = 50°$; □: $\theta = 0°$.

The interplay of pillar geometry and wettability can be illustrated by comparing the spreading curves for four contact angles in two geometries, in Fig. 4.26. We refer to the two pillar arrays as case C, with spacing ratio $\rho_p = 2/9$ and depth $0.16R_0$, and case D with $\rho_p = 3/5$ and depth $0.16R_0$, respectively, and and the ratio of their gap volumes is about 0.6. The figure indicates a qualitative difference in behavior between the two less-wetting and the two more-wetting contact angles. On the nonwetting surfaces, drops always spread and contract, both at slower rates than in the case of a flat surface (see Fig. 4.15 above). The reduction in rate is due to the transition to a Wentzel state, as discussed earlier, and the fact that the reduction is similar in the two geometries even though the gap volumes differ can be attributed to incomplete

filling of the gap due to the nonwetting nature of the liquid in this situation. For the two wettable surfaces, the effect of the pillars is again to halt the advance after the initial spreading, at times around $2t^*$, but the subsequent behavior in the two geometries differs. Here, the liquid *will* fill the gaps completely, but more is required to fill the higher volume in case D, so that in case C there is additional liquid available for the drop to continue to spread to reach its final contact angle.

4.4.3 Curved Surfaces

A different form of deviation from a flat surface is curvature, which may be though of as a model of large scale roughness appropriate to a drop which is smaller than the characteristic size of surface features. There are again numerous distinct impact configurations available, depending on the local value of the curvature and the orientation of the impact velocity with respect to the surface, but we focus on the simplest cases of normal impact on a concave or convex but otherwise homogeneous surface. Examples of both cases are shown in Fig. 4.27 for two choices of wettability and a radius of curvature of $4R_0$.

Generally the spreading drop attempts to move along the surface and its bottom follows the local curvature for both wettabilities, even after the drop floats off the nonwettable concave surface. Presumably this is an an effect of inertia: the drop molecules' initial downward momentum is first redirected laterally by the impact, and a concave shape acts to redirect this lateral momentum upwards and towards the drop axis, carrying the drop upwards and slightly inwards. In the convex case, instead, some of the downward component of the initial momentum persists and pushed the drop downwards along the surface. The drop then spreads further along the surface and the lamella thins in comparison to the concave case. The quantitative results

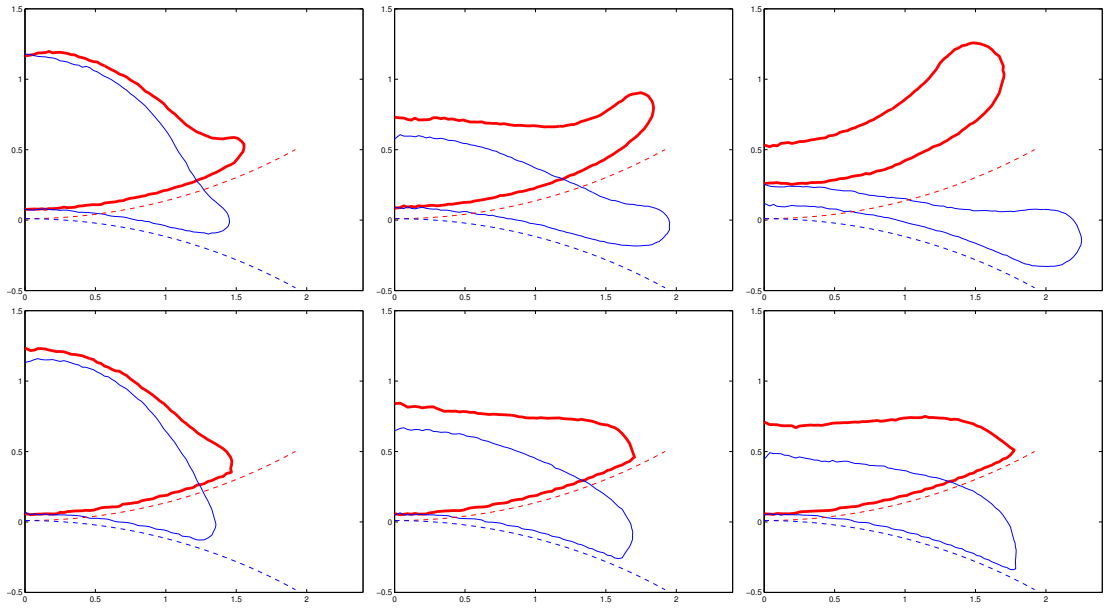

Figure 4.27 : Side view of spreading drops on walls with radius of curvature $4R_0$. The solid and dotted lines lines are the drop and wall shapes, respectively, with concave in red and convex in blue. Top row: $\theta = 180°$; Bottom row: $\theta = 50°$. Time from left to right: $t/t^* = 1, 2, 5$.

for the thickness are given in Fig. 4.28, which indicates that convex and nonwettable surfaces have thinner lamella than concave wettable ones.

The influence of the *value* of the curvature on spreading is shown in Fig. 4.29, for three different wettabilities (the completely wetting case is similar to that at 50°). The spreading radius in this situation is taken to be the circumferential distance along the surface. If we take the sign of the curvature to be negative for concave and positive for convex, the overall qualitative effect is that both the maximum spreading radius and the time required to reach it increase with curvature. More precisely, when these quantities are plotted directly in Fig. 4.30, there is a very strong variation with curvature on nonwetting surfaces, for the reasons discussed above. In the wetting case the liquid tends to wrap itself around the solid whatever its shape and spread

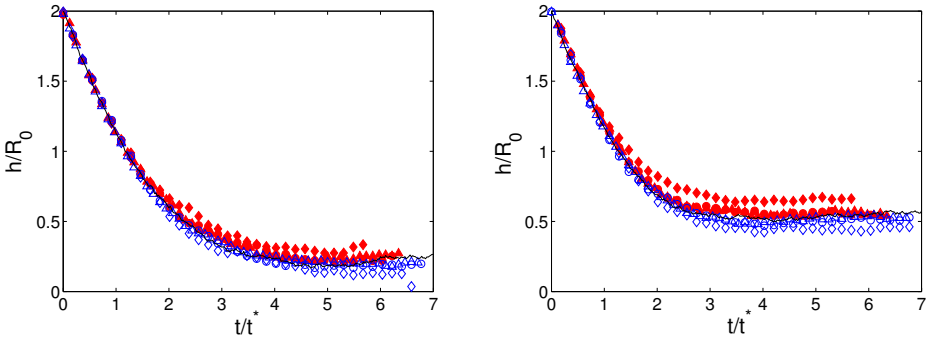

Figure 4.28 : Drop thickness at the center after impact on curved surfaces at $We = 128$ and $Re = 24$. Left: $\theta = 180°$; Right: $\theta = 50°$. Open(blue) symbols refer to a convex surface and filled(red) markers are for concave and the solid lines refer to a flat surface. Radius of curvature: ◇ or ♦: $R = \pm 2D_0$; ○ or ●: $R = \pm 6D_0$; △ or ▲: $R = \pm 10D_0$; −: $R = \infty$.

until the impact kinetic energy and momentum are dissipated, almost independently of the curvature.

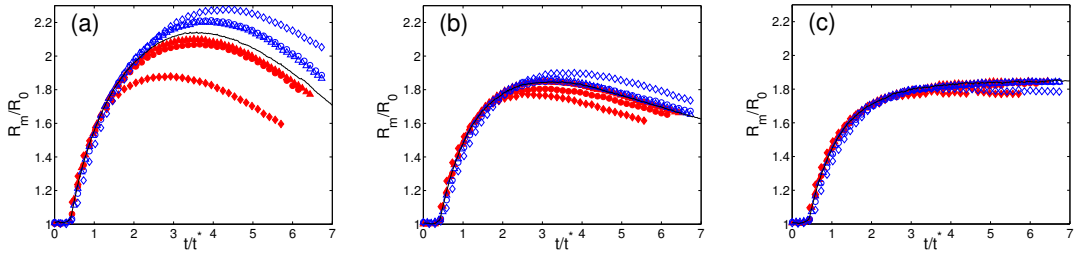

Figure 4.29 : Drop spreading on surfaces with different curvature at $Re = 24$ and $We = 128$. (a) $\theta = 180°$; (b) $\theta = 96°$; (c)$\theta = 50°$. Open (blue) markers are convex surfaces, filled (red) markers are concave surfaces and the solid line is for a flat surface. The radii of curvature shown are ◇ or ◆: $R = \pm 4R_0$: ○ or ●: $R = \pm 12R_0$; △ or ▲: $R = \pm 20R_0$.

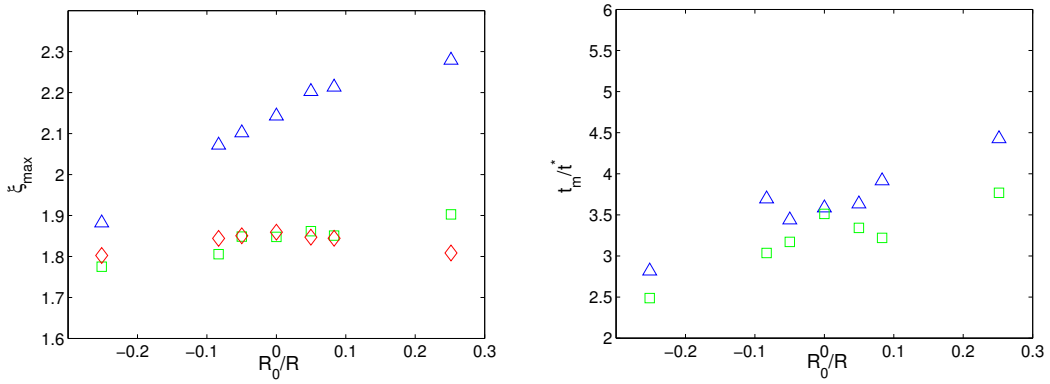

Figure 4.30 : Left: Maximum spreading factor ξ_{max} on surface of curvature R_0/R; Right: Time to reach maximum deformation t_m/t^* on surface of curvature R_0/R. Wettability: △: $\theta = 180°$; □: $\theta = 96°$; ◇: $\theta = 50°$. t_m for $\theta = 50°$ is not shown.

Chapter 5

Conclusion

We have presented numerical evidence based on simulations at two length scales, accompanied by an approximate analytic arguments, that striped patterns of enhanced interactions on a substrate will deflect particle trajectories away from the direction imposed by pressure-driven flow. The amount of deflection varies with the particle size or interaction parameters, and therefore a microfluidic device based on patterned wall interactions may be used to provide continuous and autonomous particle separation. Patterned interactions based on both van der Walls and Coulomb forces were studied, and both produce generally comparable results. As in the analogous problem of separation by flow through an obstacle array [18], we expect that the form of the driving mechanism is immaterial, and similar behavior would be found if the particles were driven past the pattern by an external force.

The numerical results for nanometer-sized particles were obtained from MD simulations, while the behavior of larger (but still colloidal) particles arises from simulations of the corresponding Langevin equation. By investigating the Fokker-Planck equation corresponding to a 2D (FIck-Jacobs) limit of the Langevin system, we are able to demonstrate the generality of trajectory deflection, obtain some general limits on the results, and partly guide parameter optimization. The results of the simulations indicate optimal parameter choices for the particular particle and substrate models considered, but we are unable to state completely general criteria. The difficulty is that large particle deflection angles are preferable for separation, which sug-

gests strengthening the interactions, but in this limit particle trapping is enhanced as well and thereby reduces the efficiency of separation. The ideal balance between these two considerations is then rather system dependent. Nonetheless, we have found that selective trajectory deflection and particle separation are ubiquitous consequences of flow past a patterned interaction, and a device based on this principle is viable.

We then use both molecular dynamics and lattice Boltzmann simulation techniques to simulate drop impact on surfaces with various shapes and textures for a range of moderate impact velocities ($10 \leq Re \leq 36$ and $20 \leq We \leq 300$) and fixed Ohnesorge number $Oh = 0.4774$. Lower velocities lead to smaller initial deformations and dynamics dominated by quasi-static spreading considerations. Higher velocities lead to drop splashing, for which neither method is appropriate. Aside from illustrating the evolving drop shapes, we quantify the behavior in terms of the time dependence of the drop height and spreading radius. Since MD operates at atomic length and time scales while LB is constructed to solve the Navier-Stokes equations at continuum scales, a comparison of the results of the two methods is of some interest. We find reasonable agreement between the methods for slow impact on wettable surfaces, and some deviation otherwise. There are two sources of disagreement: compressibility in the MD case and boundary effects in LB. In order to increase the Reynolds number to higher values for a nanometer-sized drop the impact velocity exceeds the thermal velocity of the fluid and begins to approach the sound speed. The observed variation in volume at the highest impact velocities discussed in this paper is around 5% at $Ma \approx 0.3$. In principle the LB calculations can be modified to finite Ma, but convergence issues arise at the relevant high velocities. The second distinction between the methods is in the treatment of solid boundaries. Both MD and LB work well for surfaces which are at least partially wettable, where a no-slip

boundary condition is appropriate at low shear rates. Otherwise, MD predicts systematically increasing slip lengths and, for very low wettability, only tenuous contact between the drop and the surface. In LB the surface interaction is implemented in an entirely different way, and the slip velocity is independent of wettability during the spreading stage.

Aside from a comparison of two methods, we have explored the behavior of drops impacting surfaces which are not atomically smooth and homogeneous. To study the effects of the variability of surface wetting properties, we considered an example studied previously involving a surface with a cross pattern of one wettability embedded in a differently wettable background. The fact that spreading is more rapid as wettability decreases leads to final drop shapes with various indentations and protuberances, and different degrees of spreading. In the case of surface structural heterogeneity, we focused on periodic arrays of pillars, a configuration relevant to super-hydrophobic behavior. Here the filling of the gaps between pillars leads to lower areal coverage by the drop, related to transitions between Cassie and Wenzel states. Finally, we considered surfaces with various curvatures which reflect larger scale rough features. Curvature has a pronounced effect in the nonwetting case, and leads to spreading distances and times which increase with curvature, a thinner spreading lamella and more of a tendency for an impacting drop to bounce, although the effect is small in the wetting case.

The results indicate a partial overlap in the results of the two computational methods, along with distinct limitations on the range of operating conditions where this agreement holds. The MD method does not have many internal "computational" parameters to adjust: once the potential is specified, quantities such as the time step are fixed by numerical accuracy and stability requirements, the material properties and

transport coefficients are determined, and the numbers of the various atomic species present are in direct correspondence to the physical size of the system being studied. The LB method is, like the Navier-Stokes equations themselves, not restricted to a particular system scale, but it does involve a number of internal variables without a direct physical counterpart, such as the Cahn-Hilliard potential and the mobility, which allow the material and dynamic properties to be adjusted to some degree. In this paper the particular LB algorithm has allowed some improvements along these lines, which might be regarded as calibrating the method using the results of (external, numerical) experiments, but a robust computational tool spanning the full range of hydrodynamic phenomena needs further development.

Appendix

Appendix

.1 Sound Speed

The sound speed is given generally by

$$u_s^2 = \left(\frac{\partial p}{\partial \rho}\right)_S = -\frac{V}{\rho}\left(\frac{\partial p}{\partial V}\right)_S,$$

where p and ρ are the pressure and density of the medium, respectively. The second form is useful in MD calculations, where it can be implemented by a sequence of NVT simulations in which the volume V is slowly varied while the constant entropy (S) constraint is satisfied by isolating the system thermally so that there is no heat flux. We first equilibrate a system of 16, 000 dimer molecules in a periodic cube of size 34.2σ at temperature $0.8\epsilon/k_B$ and density either slightly above or below the target value $0.8m\sigma^{-3}$. The volume is then either decreased or increased by 0.5% over a 400τ time interval, approximately an adiabatic variation in volume, so as to bracket the target density. The resulting pressure variation is shown in Fig. .1(a), from which the slope of the linear least-squares fit gives $u_s = (4.1 \pm 0.1)\sigma/\tau$.

As a check on the result, we use a second method: direct simulation of a sound wave. Here we place a dimer liquid at the desired density in a rectangular simulation box of dimension $(X, Y, Z) = (20.5, 215.5, 20.5)\sigma$, bounded by two solid walls in the (long) y-direction. After equilibration, one wall is rigidly oscillated in y at frequency $\omega = 0.6\tau^{-1}$ and amplitude σ. The opposite wall is fixed in place and thermostated to absorb the energy flux resulting from the oscillation. After a transient period,

we observe a traveling wave of spatial variation in density, shown at one time in Fig. .1(b). For reference, the density variation due to the oscillation is compared to that resulting from equilibrium fluctuations in the same fluid in a fixed volume. A clear signal is present near the oscillating wall, although the wave decays near the fixed wall due to energy adsorption there. From the spatial variation of density, a wavelength can be extracted and, given the frequency, we find $u_s = (4.8 \pm 0.3)\sigma/\tau$. The two methods are in qualitative agreement, but we consider the first to be more reliable. Some deficiencies of the second method are (1) the temperature of the liquid is not controlled, (2) we have not taken into account any reflected wave, and (3) a rather high frequency is needed in order to have a wavelength well below the size of the simulation box.

The measurements are repeated for monoatomic and tetratomic Lennard-Jones fluid, and the results are summarized in Table. .1. The point of the monomer measurement is that this simulated material is a reasonable approximation to liquid Argon, whose sound speed has been measured experimentally to be 853 m/s at 44.4 MHZ and 85 K and atmospheric pressure, close to the simulation result for method I. The fact that the sound speed in dimer liquids is lower than in monomer liquids is consistent in trend with ideal gas theory where $u_s = (\gamma k_B T/m)^{(\frac{1}{2})}$: the adiabatic index γ is lower for dimers than monomers. Monomer liquid of the same density is also measured using the above two methods. We conclude all the results in table .1.

.2 Expression for the particle flux

If we introduce $f(x) = e^{V(x)-Gx}$, Eq. (3.22) can be written

$$-G\, J_x\, f(x) = \frac{\partial}{\partial x}(f(x)P(x)),$$

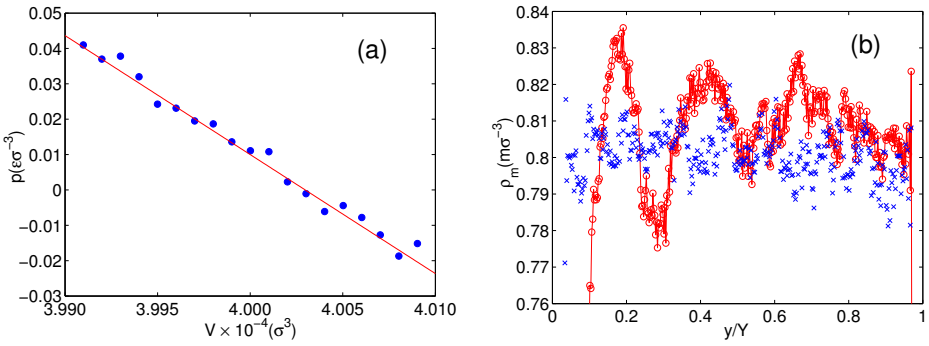

Figure .1 : (a) p-V diagram for dimers; (blue)pints are simulation results are the (red)line is a fit. (b) Density profile produced by an oscillating wall: ∘, oscillating wall, ×, stationary wall.

Liquid	$\rho(m\sigma^{-3})$	Method I	Method II
Monomer	0.8	5.0 ± 0.1	5.7 ± 0.6
Dimer	0.8	4.1 ± 0.1	4.8 ± 0.3
Tetramer	0.86	4.8 ± 0.2	5.5 ± 0.4

Table .1 : Measurements of the speed of sound at $T = 0.8\epsilon/k_B$. Method I refers to the isentropic process simulation and Method II refers to the direct simulation of sound wave.

equation Integrating from 0 to x,

$$-G\,J_x \int_0^x f(x')\,dx' = f(x)P(x) - f(0)P(0). \tag{.1}$$

If we define $A(x) = \int_0^x f(x')dx'$ and $A_1 = A(1) = \int_0^1 f(x')dx'$, and evaluate the above equation at $x = 1$ we have

$$-G\,J_x\,A_1 = (e^{-G} - 1)f(0)P(0),$$

which gives $P(0)$. Equation (.1) become

$$-G\,J_x\,A(x) = f(x)P(x) + G\,J_x\,A_1\frac{1}{e^{-G}-1},$$

Dividing both sides by $f(x)$ and integrating from 0 to 1 gives

$$-GJ_x\int_0^1 \frac{A(x)}{f(x)}\,dx = 1 + \frac{G\,J_x\,A_1}{e^{-G}-1}\int_0^1 \frac{dx}{f(x)}.$$

Solving for J_x, we find

$$\frac{1}{J_x} = G\left[\frac{A_1}{1-e^{-G}}\int_0^1 \frac{dx}{f(x)} - \int_0^1 \frac{A(x)}{f(x)}\,dx\right]. \tag{.2}$$

.3 Other forms of the solution

To prove Eq. (3.27), first introduce the definition of A_1 in Eq. (.2):

$$\begin{aligned}
\kappa &= G\left[\frac{1}{1-e^{-G}}\int_0^1 f(x')\,dx'\int_0^1 \frac{dx}{f(x)} - \int_0^1 \frac{A(x)}{f(x)}\,dx\right] \\
&= G\left[\frac{1}{1-e^{-G}}\left(\int_0^1 \frac{dx}{f(x)}\int_0^x f(x')\,dx' + \int_0^1 \frac{dx}{f(x)}\int_x^1 f(x')\,dx'\right) - \int_0^1 \frac{dx}{f(x)}\int_0^x f(x')\,dx'\right] \\
&= G\left[\left(\frac{1}{1-e^{-G}}-1\right)\int_0^1 \frac{dx}{f(x)}\int_0^x dx'\,f(x') + \frac{1}{1-e^{-G}}\int_0^1 \frac{dx}{f(x)}\int_x^1 f(x')\,dx'\right] \\
&= G\left[\frac{e^{-G}}{1-e^{-G}}\int_0^1 dx\int_0^x dx'\,e^{G(x-x')}e^{V(x')-V(x)} + \frac{1}{1-e^{-G}}\int_0^1 dx\int_x^1 dx'\,e^{G(x-x')}e^{V(x')-V(x)}\right],
\end{aligned}$$

Changing the order of integral variables in the first term above, one has

$$\kappa = G\left[\frac{e^{-G}}{1-e^{-G}}\int_0^1 dx'\int_{x'}^1 dx\,e^{G(x-x')}e^{V(x')-V(x)} + \frac{1}{1-e^{-G}}\int_0^1 dx\int_x^1 dx'\,e^{G(x-x')}e^{V(x')-V(x)}\right],$$

and then switching x and x' in the first term gives

$$\begin{aligned}
\kappa &= G\left[\frac{e^{-G}}{1-e^{-G}}\int_0^1 dx\int_x^1 dx'\,e^{G(x'-x)}e^{V(x)-V(x')} + \frac{1}{1-e^{-G}}\int_0^1 dx\int_x^1 dx'\,e^{G(x-x')}e^{V(x')-V(x)}\right] \\
&= \frac{G}{1-e^{-G}}\int_0^1 dx\int_x^1 dx'\left[e^{G(x'-x-1)}e^{V(x)-V(x')} + e^{G(x-x')}e^{V(x')-V(x)}\right].
\end{aligned} \tag{.3}$$

To prove Eq. (3.29), use the periodicity of $V(x)$:

$$\kappa = \frac{G}{1-e^{-G}} \int_0^1 dx \int_x^1 dx' \left[e^{G(x'-(x+1))} e^{V(x+1)-V(x')} + e^{G(x-x')} e^{V(x')-V(x)} \right]$$
$$\equiv \frac{G}{1-e^{-G}} \left[A + B \right],$$

In A, changing the order of integration:

$$A = \int_0^1 dx' \int_0^{x'} dx\, e^{G(x'-(x+1))} e^{V(x+1)-V(x')},$$

and let $y = x + 1 - x'$, so that:

$$A = \int_0^1 dx' \int_{1-x'}^1 dy\, e^{-Gy} e^{V(x'+y)-V(x')} = \int_0^1 dx \int_{1-x}^1 dy\, e^{-Gy} e^{V(x+y)-V(x)}.$$

Similarly, let $y = x' - x$ in B to give:

$$B = \int_0^1 dx \int_0^{1-x} dy\, e^{-Gy} e^{V(x+y)-V(x)},$$

Combining,

$$\kappa = \frac{G}{1-e^{-G}} \int_0^1 dx \int_0^1 dy\ e^{-Gy} e^{V(x+y)-V(x)},$$

and using the definition of $p(y)$ in Sec. 3.4.2, we recover Eq. (3.29).

.4 Proof of $p(y) \geq 1$

Since $V(x)$ can be shifted by a constant without changing the integral defining $p(y)$, we may assume that $0 \leq V(x) \leq V_0$. If $V_0 \leq 1$, the exponential function $e^{V(x+y)-V(x)}$ can be expanded as

$$p(y) = \int_0^1 dx \left[1 + [V(x+y) - V(x)] + \sum_{n=1}^{+\infty} \left(\frac{[V(x+y)-V(x)]^{2n}}{(2n)!} + \frac{[V(x+y)-V(x)]^{2n+1}}{(2n+1)!} \right) \right],$$

the first term of which is 1 after integration and the second term is 0. Since $|V(x+y) - V(x)| \leq 1$,

$$\frac{(V(x+y)-V(x))^{2n}}{(2n)!} \geq \left| \frac{(V(x+y)-V(x))^{2n+1}}{(2n+1)!} \right|$$

and the third term is nonnegative, which implies $p(y) \geq 1$.

If $V_0 > 1$, one has

$$p(y) = \int_0^1 dx \left[\exp\left(\frac{V(x+y)}{V_0} - \frac{V(x)}{V_0} \right) \right]^{V_0}.$$

By Hölder's Inequality, one has

$$p(y) \geq \left[\int_0^1 dx \, \exp\left(\frac{V(x+y)}{V_0} - \frac{V(x)}{V_0} \right) \right]^{V_0}.$$

Since $0 \leq V(x)/V_0 \leq 1$, the same argument gives

$$\int_0^1 dx \, e^{\frac{V(x+y)}{V_0} - \frac{V(x)}{V_0}} \geq 1,$$

and since $V_0 > 1$, $p(y) \geq 1$.

.5 Use of the Fick-Jacob approximation

The Fick-Jacob approximation [94, 95] is appropriate for narrow channels, and assumes that the particle density comes to equilibrium rapidly in that direction, and the conditional probability density $\rho(y, z|x)$ is Boltzmann,

$$\rho(y, z|x) \approx \rho(y, z|x)_{eq} = e^{-V(\vec{r})/k_B T} / I(x),$$

where $I(x)$ is some normalization function. Firstly consider that particle is drifted purely by an external force F. According to Eq. (25) in Drazers' paper([19]),

$$\kappa = \frac{G}{1 - e^{-G}} \int_0^1 dy \; e^{-G \; y} \int_0^1 dx \frac{\int_0^1 dy \; M(y') \; e^{-V(x,y')}}{\int_0^1 dy \; M(y') \; e^{-V(x+y,y')}}.$$

Introducing an effective potential $U(x)$ which satisfies

$$e^{-U(x)} = \int_0^1 dy' \; M(y') \; e^{-V(x,y')},$$

$U(x)$ is also a periodic function, thus:

$$\kappa = \frac{G}{1-e^{-G}} \int_0^1 dy\ e^{-Gy} \int_0^1 dx\ e^{U(x+y)-U(x)},$$

which is identical to the formula in 2D theory. Therefore $\kappa \geq 1$. One can use the same trick for particle convected purely by a flow $u(y)$. According to Eq. (32) in Drazer's paper([19]):

$$\kappa = \frac{G}{1-e^{-G\Phi(1)}} \int_0^1 dy \int_0^1 dx\ e^{-G(\Phi(x+y)-\Phi(x))} e^{U(x+y)-U(x)},$$

where $\phi(x) = \frac{\bar{u}(x)}{\bar{M}_{\|}(x)}$, $\Phi(x) = \int_0^x dx' \phi(x')$. If the flow is invariant longitudinally(along x), $\phi(x) = \phi = 1$, $\Phi(x) = x$, the above equation reduces to

$$\kappa = \frac{G}{1-e^{-G}} \int_0^1 dy \int_0^1 dx\ e^{-Gy} e^{U(x+y)-U(x)},$$

which is again identical to the pure force case. Thus $\kappa \geq 1$.

.6 Upper bound on κ

Defining the average of $p(y)$ as

$$\bar{p}(y) \equiv \int_0^1 dy\, p(y) = \iint_0^1 dx dy\, e^{P(x+y)-P(x)},$$

and letting $z = x + y$, one has

$$\begin{aligned}
\bar{p}(y) &= \int_0^1 dz \int_0^z dx\, e^{V(z)-V(x)} + \int_1^2 dz \int_{z-1}^1 dx\, e^{V(z)-V(x)} \\
&= \int_0^1 dz \int_0^z dx\, e^{V(z)-V(x)} + \int_0^1 dz \int_z^1 dx\, e^{V(z+1)-V(x)} \\
&= \int_0^1 dz \int_0^z dx\, e^{V(z)-V(x)} + \int_0^1 dz \int_z^1 dx\, e^{V(z)-V(x)} \\
&= \int_0^1 dz \int_0^1 dx\, e^{V(z)-V(x)} = \int_0^1 dx_1 \int_0^1 dx_2\, e^{V(x_1)-V(x_2)},
\end{aligned}$$

By the Cauchy-Schwarz inequality,

$$\begin{aligned}
p(y)\bar{p}(y) &= \iiint_0^1 dx_1 dx_2 dx\, e^{V(x_1)-V(x_2)} e^{V(x+y)-V(x)} \\
&= \iiint_0^1 dx_1 dx_2 dx\, e^{V(x_1)-V(x)} e^{V(x+y)-V(x_2)} \\
&\leq \left(\iiint_0^1 dx_1 dx_2 dx\, e^{2V(x_1)-2V(x)} \right)^{\frac{1}{2}} \left(\iiint_0^1 dx_1 dx_2 dx\, e^{2V(x+y)-2V(x_2)} \right)^{\frac{1}{2}} \\
&= \left(\iint_0^1 dx_1 dx\, e^{2V(x_1)-2V(x)} \right)^{\frac{1}{2}} \left(\iiint_0^1 dx dx_2\, e^{2V(x)-2V(x_2)} \right)^{\frac{1}{2}} \\
&= \iint_0^1 dx_1 dx\, e^{2(V(x_1)-V(x))}.
\end{aligned}$$

Thus an upper bound of $p(y)$ is

$$\begin{aligned}
p(y) \leq \sup p(y) &= \iint_0^1 dx_1 dx\, e^{2(V(x_1)-V(x))} / \bar{p}(y) \\
&= \iint_0^1 dx dy\, e^{2(V(x)-V(y))} / \iint_0^1 dx dy\, e^{V(x)-V(y)},
\end{aligned}$$

and therefore an upper bound on κ is

$$\begin{aligned}
\kappa = \frac{G}{1-e^{-G}} \int_0^1 dy\ e^{-Gy} p(y) &\leq \frac{G}{1-e^{-G}} \int_0^1 dy\ e^{-Gy} \cdot \sup p(y). \\
= \sup p(y) = \iint_0^1 dx dy\ e^{2(V(x)-V(y))} &/ \iint_0^1 dx dy\ e^{V(x)-V(y)}
\end{aligned}$$

.7 Weak potential approximation

Appendix .6 shows that the upper bound of κ is $K = \iint_0^1 dx dy e^{2(V(x)-V(y))} / \iint_0^1 dx dy e^{V(x)-V(y)}$. Suppose that the potential is weak, in the sense that $0 \leq V(x) \leq 1$ (recall that V has been nondimensionalized by $k_B T$), which implies that $|V(x) - V(y)| \leq 1$. Since

$$\iint_0^1 dx dy\, (V(x) - V(y))^2 = 2 \int_0^1 dx\, V(x)^2 - 2 \left(\int_0^1 dx\, V(x) \right)^2 = 2\langle \Delta V^2 \rangle,$$

one has

$$\begin{aligned}\iint_0^1 dxdy\, e^{2(V(x)-V(y))} &= 1+\frac{2^2}{2!}\iint_0^1 dxdy\,(V(x)-V(y))^2+\frac{2^4}{4!}\iint_0^1 dxdy\,(V(x)-V(y))^4+...\\ &\le 1+(\frac{2^2}{2!}+\frac{2^4}{4!}+...)\iint_0^1 dxdy\,(V(x)-V(y))^2\\ &= 1+(e^2+e^{-2}-2)\langle\Delta V^2\rangle,\end{aligned}$$

because the odd terms vanish identically, and

$$\begin{aligned}\left[\iint_0^1 dxdy\, e^{V(x)-V(y)}\right]^{-1} =&[1+\frac{1}{2!}\iint_0^1 dxdy\,(V(x)-V(y))^2\\ &+\frac{1}{4!}\iint_0^1 dxdy\,(V(x)-V(y))^4+...]^{-1}\\ &\le\left[1+\langle\Delta V^2\rangle\right]^{-1}.\end{aligned}$$

Thus,

$$K\le\frac{1+(e^2+e^{-2}-2)\langle\Delta V^2\rangle}{1+\langle\Delta V^2\rangle}\le 1+(e^2+e^{-2}-3)\langle\Delta V^2\rangle\simeq 1+4.52\langle\Delta V^2\rangle.$$

If the Péclet number $G\to 0$:

$$\kappa\to\kappa_0=\iint_0^1 dxdy\, e^{V(x)-V(y)}=1+\frac{1}{2!}\iint_0^1 dxdy\,(V(x)-V(y))^2+...\ge 1+\langle\Delta V^2\rangle,$$

showing a non-vanishing deflection. For a more refined estimate, write

$$\begin{aligned}\kappa_0 &= 1+\frac{1}{2!}\iint_0^1 dxdy\,(V(x)-V(y))^2+\frac{1}{4!}\iint_0^1 dxdy\,(V(x)-V(y))^4+...\\ &\le 1+(\frac{1}{2!}+\frac{1}{4!}+...)\iint_0^1 dxdy\,(V(x)-V(y))^2\\ &= 1+(e+e^{-1}-2)\langle\Delta V^2\rangle\\ &= 1+1.086\langle\Delta V^2\rangle.\end{aligned}$$

Therefore in general $1\le\kappa\le 1+4.52\langle\Delta V^2\rangle$ and in slow flow $\kappa\approx 1+1.1\langle\Delta V^2\rangle$.

Bibliography

[1] H. Craighead, "Future lab-on-a-chip technologies for interrogating individual molecules," *Nature*, vol. 442, pp. 387–393, 2006.

[2] G. M. Whitesides, "The origins and the future of microfluidics," *Nature*, vol. 442, pp. 368–373, 2006.

[3] P. S. Dittrich and A. Manz, "Lab-on-a-chip: microfluidics in drug discovery," *Nature Review Drug Discovery*, vol. 5, pp. 210–218, 2006.

[4] J. Zeng and T. Korsmeyer, "Principles of droplet electrohydrodynamics for lab-on-a-chip," *Lab Chip*, vol. 4, pp. 265–277, 2004.

[5] S. Haeberlea and R. Zengerle, "Microfluidic platforms for lab-on-a-chip applications," *Lab Chip*, vol. 7, pp. 1094–1110, 2007.

[6] P. Tsai, R. van der Veen, M. van de Raa, and D. Lohse, "How Micropatterns and Air Pressure Affect Splashing on Surfaces," *Langmuir*, vol. 26, no. 20, p. 1609016095, 2010.

[7] A. Theodorakakos, T. Ous, M. Gavaises, J. M. Nouri, N. Nikolopoulos, and H. Yanagihara, "Dynamics of water droplets detached from porous surfaces of relevance to PEM fuel cells," *J. Colloid Inter. Sci.*, vol. 300, pp. 673–687, 2006.

[8] C. Antonini, M. Innocenti, T. Horn, M. Marengo, and A. Amirfazli, "Understanding the effect of superhydrophobic coatings on energy reduction in anti-icing

systems," *Cold Regions Sci. Technol.*, vol. 67, pp. 58–67, 2011.

[9] J. B. Lee and S. H. Lee, "Dynamic wetting and spreading characteristics of a liquid droplet impinging on hydrophobic textured surfaces," *Langmuir*, vol. 27, pp. 6565–6573, 2011.

[10] R. D. Astumian and M. Bier, "Fluctuation driven ratchets: Molecular motors," *Phys. Rev. Lett.*, vol. 72, no. 11, pp. 1766–1769, 1994.

[11] G. Oster, "Brownian ratchets: Darwin's motors," *Nature*, vol. 417, p. 25, 2002.

[12] G. Lagubeau, M. L. Merrer, C. Clanet, and D. Quéré, "Leidenfrost on a ratchet," *Nat. Phys.*, vol. 7, pp. 395–398, 2011.

[13] M. Chinappi, E. D. Angelis, S. Melchionna, C. M. Casciola1, S. Succi, and R. Piva1, "Molecular Dynamics Simulation of Ratchet Motion in an Asymmetric Nanochannel," *Phys. Rev. Lett.*, vol. 97, p. 144509, 2006.

[14] J. D. Halverson, C. Maldarelli, A. Couzis1, and J. Koplik, "A molecular dynamics study of the motion of a nanodroplet of pure liquid on a wetting gradient," *J. Chem. Phys.*, vol. 129, no. 16, p. 164708, 2008.

[15] S. Daniel, S. Sircar, J. Gliem, and M. K. Chaudhury, "Ratcheting Motion of Liquid Drops on Gradient Surfaces," *Langmuir*, vol. 20, no. 10, pp. 4085–4092, 2004.

[16] L. R. Huang, E. C. Cox, R. H. Austin, and J. C. Sturm, "Continuous Particle Separation Through Deterministic Lateral Displacement," *Science*, vol. 304, pp. 987–990, 2004.

[17] J. A. Davis, D. W. Inglis, K. J. Morton, D. A. Lawrence, L. R. Huang, S. Y. Chou, J. C. Sturm, and R. H. Austin, "Continuous Particle Separation Through Deterministic Lateral Displacement," *Proc. Natl. Acad. Sci.*, vol. 103, pp. 14779–14784, 2006.

[18] J. Koplik and G. Drazer, "Nanoscale simulations of directional locking," *Phys. Fluids*, vol. 22, p. 052005, 2010.

[19] J. A. Bernate and G. Drazer, "Partition-induced vector chromatography in microfluidic devices," *J. Colloid and Inter. Sci.*, vol. 356, no. 1, pp. 341–351, 2011.

[20] J. Frechette and G. Drazer, "Directional locking and deterministic separation in periodic arrays," *J. Fluid Mech.*, vol. 627, pp. 379–401, 2009.

[21] A. E. Herr, A. V. Hatch, D. J. Throckmorton, H. M. Tran, J. S. Brennan, W. V. Giannobile, and A. K. Singh, "Microfluidic immunoassays as rapid saliva-based clinical diagnostics," *Proc. Nat. Aca. Sci.*, vol. 104, no. 13, pp. 5268–5273, 2007.

[22] H. Dong, W. W. Carr, D. G. Bucknall, and J. F. Morris, "Temporally-resolved inkjet drop impaction on surfaces," *AIChE J.*, vol. 53, pp. 260–2617, 2007.

[23] S. Kim, M.-W. Moon, and H.-Y. Kim, "Drop impact on super-wettability-contrast annular patterns," *J. Fluid Mech.*, vol. 730, pp. 328–342, 2013.

[24] T. Bennett and D. Poulikakos, "Splat-quench solidification: estimating the maximum spreading of a droplet impacting a solid surface," *J. Mat. Sci.*, vol. 28, pp. 963–970, 1993.

[25] J. C. Giddings, *Unified Separation Science*. New York: Wiley-Interscience, 1991.

[26] J. C. Giddings, "Field-flow fractionation: analysis of macromolecular, colloidal, and particulate materials," *Science*, vol. 260, pp. 1456–1465, 1993.

[27] M. Yamada, M. Nakashima, and M.Seki, "Pinched Flow Fractionation: Continuous Size Separation of Particles Utilizing a Laminar Flow Profile in a Pinched Microchannel," *Anal. Chem.*, vol. 76, pp. 5465–5471, 2004.

[28] J. Takagi, M. Yamada, M. Yasuda, and M. Seki, "Continuous particle separation in a microchannel having asymmetrically arranged multiple branches," *Lab Chip*, vol. 5, pp. 778–784, 2005.

[29] Y. Sai, M. Yamada, M. Yasuda, and M. Seki, "Continuous particle separation in a microchannel having asymmetrically arranged multiple branches," *J. Chromatogr. A*, vol. 1127, no. 1-2, pp. 214–220, 2006.

[30] M. Yamada and M. Seki, "Hydrodynamic filtration for on-chip particle concentration and classification utilizing microfluidics," *Lab Chip*, vol. 5, pp. 1233–1239, 2005.

[31] S. Choi and J. Park, "Continuous hydrophoretic separation and sizing of microparticles using slanted obstacles in a microchannel," *Lab Chip*, vol. 7, pp. 890–897, 2007.

[32] S. Choi and J. Park, "Tuneable hydrophoretic separation using elastic deformation of poly(dimethylsiloxane)," *Lab Chip*, vol. 9, pp. 1962–1965, 2009.

[33] S. Choi, S. Song, C. Choi, and J. Park, "Hydrophoretic Sorting of Micrometer and Submicrometer Particles Using Anisotropic Microfluidic Obstacles," *Anal. Chem.*, vol. 81, pp. 50–55, 2009.

[34] K. D. Dorfman and H. Brenner, "Vector Chromatography: Modeling Micropatterned Separation Devices," *J. Colloid and Inter. Sci.*, vol. 238, no. 2, pp. 390–413, 2001.

[35] K. D. Dorfman and H. Brenner, "Separation mechanisms underlying vector chromatography in microlithographic arrays," *Phys. Rev. E*, vol. 65, p. 052103, 2002.

[36] K. D. Dorfman and H. Brenner, "Two-dimensional separations: concept and promise," *Anal. Chem.*, vol. 56, pp. 1258A–1264A, 1984.

[37] Z. Li and G. Drazer, "Separation of Suspended Particles by Arrays of Obstacles in Microfluidic Devices," *Phys. Rev. Lett.*, vol. 98, p. 050602, 2007.

[38] K. J. Morton, K. Loutherback, D. W. Inglis, O. K. Tsui, J. C. Sturm, S. Y. Chou, and R. H. Austin, "Crossing microfluidic streamlines to lyse, label and wash cells," *Lab Chip*, vol. 8, p. 1448, 2008.

[39] K. J. Morton, K. Loutherback, D. W. Inglis, O. K. Tsui, J. C. Sturm, S. Y. Chou, and R. H. Austin, "Hydrodynamic metamaterials: Microfabricated arrays to steer, refract, and focus streams of biomaterials," *Proc. Natl. Acad. Sci.*, vol. 105, p. 7434, 2008.

[40] J. Herrmann, M. Karweit, and G. Drazer, "Separation of suspended particles in microfluidic systems by directional locking in periodic fields," *Phys. Rev. E*, vol. 79, p. 061404, 2009.

[41] M. Balvin, E. Sohn, T. Iracki, G. Drazer, and J. Frechette, "Directional Locking and the Role of Irreversible Interactions in Deterministic Hydrodynamics Separations in Microfluidic Devices," *Phys. Rev. Lett.*, vol. 103, p. 078301, 2009.

[42] L. Xu, W. W. Zhang, and S. R. Nagel, "Drop Splashing on a Dry Smooth Surface," *Phys. Rev. Lett.*, vol. 94, p. 184505, 2005.

[43] A. L. Yarin, "Drop impact dynamics: Splashing, spreading, receding, bouncing, . . .," *Annu. Rev. Fluid Mech.*, vol. 38, pp. 159–192, 2006.

[44] R. Rioboo, C.Tropea, and M.Marengo, "Outcomes from a drop impact on solid surfaces," *Atomization Spray*, vol. 11, p. 2, 2001.

[45] H. Marmanis and S. T. Thoroddsen, "Scaling of the fingering pattern of an impacting drop," *Phys. Fluids*, vol. 8, pp. 1344–1346, 1996.

[46] J. Koplik and R. Zhang, "Nanodrop impact solid surfaces," *Phys. Fluids*, vol. 25, p. 022003, 2013.

[47] R. Dhiman and S. Chandra, "Rupture of thin films formed during droplet impact," *Proc. R. Soc. A*, vol. 466, pp. 1229–1245, 2010.

[48] L. Courbin, J. C. Bird, A. Belmonte, and H. A. Stone, "Black hole nucleation in a splash of milk," *Phys. Fluids*, vol. 29, p. 091106, 2008.

[49] J. G. Leidenfrost, *De Aquae Communis Nonnul lis Qualitatibus Tractatus*. Duisburg, 1756. English translation by C. Wares, Int. J. Heat Mass Transfer **9**, 1153 (1966).

[50] F. Celestini, T. Frisch, and Y. Pomeau, "Take Off of Small Leidenfrost Droplets," *Phys. Rev. Lett.*, vol. 109, p. 034501, 2012.

[51] J. Horbach and S. Succi, "Lattice Boltzmann versus molecular dynamics simulation of nanoscale hydrodynamic flows," *Phys. Rev. Lett.*, vol. 96, p. 224503, 2006.

[52] L. W. Schwartz and R. R. Eley, "Simulation of Droplet Motion on Low-Energy and Heterogeneous Surfaces," *J. Colloid Inter. Sci.*, vol. 202, pp. 173–188, 1998.

[53] L. W. Schwartz, "Hysteretic Effects in Droplet Motions on Heterogeneous Substrates: Direct Numerical Simulation," *Langmuir*, vol. 14, pp. 3440–3453, 1998.

[54] V. Vaikuntanathan, R. Kannan, and D. Sivakumar, "Impact of water drops onto the junction of a hydrophobic texture and a hydrophilic smooth surface," *Colloids Surf A*, vol. 369, pp. 65–74, 2010.

[55] U. Mock, T. Michel, C. Tropea, I. Roisman, and J. Rühe, "Drop impact on chemically structured arrays," *J. Phys. Condens. Matter*, vol. 17, pp. S595–S605, 2005.

[56] M. Lee, Y. S. Chang, and H.-Y. Kim, "Drop impact on microwetting patterned surfaces," *Phys. Fluids.*, vol. 22, p. 072101, 2010.

[57] H. Katsuragi, "Morphology Scaling of Drop Impact onto a Granular Layer," *Phys. Rev. Lett.*, vol. 104, p. 218001, 2010.

[58] G. O. Berim and E. Ruckenstein, "Nanodrop on a nanorough hydrophilic solid surface: Contact angle dependence on the size, arrangement, and composition of the pillars," *J. Colloid and Interface Sci.*, vol. 359, pp. 304–310, 2011.

[59] G. O. Berim and E. Ruckenstein, "Nanodrop on a nanorough solid surface: Density functional theory considerations," *J. Chem. Phys.*, vol. 129, p. 014708, 2008.

[60] D. Sivakumar, K. Katagiri, T. Sato, and H. Nishiyama, "Spreading behavior of an impacting drop on a structured rough surface," *Phys. Fluids*, vol. 17, p. 100608, 2005.

[61] L. D. Landau and E. M. Lifshitz, *Fluid mechanics, Course of Theoretical Physics 6*. Oxford: Pergamon Press, 2nd revised ed. ed., 1987.

[62] A. Einstein, "Über die von der molekularkinetischen Theorie der Wärme geforderte Bewegung von in ruhenden Flüssigkeiten suspendierten Teilchen," *Annalen der Physik*, vol. 17, no. 8, pp. 549–560, 1905.

[63] C. L. M. H. Navier, "Mémoire sur les lois du mouvement des uids," *Mem. Acad. Sci. Inst. Fr.*, vol. 6, pp. 389–416, 1823.

[64] P. A. Thompson and S. M. Troian, "A general boundary condition for liquid flow at solid surfaces," *Nature*, vol. 389, no. 25, pp. 360–362, 1997.

[65] H. Risken, *The Fokker-Planck Equation*. New York: Springer, 1984.

[66] P. Langevin, "On the Theory of Brownian Motion," *C. R. Acad. Sci.*, vol. 146, pp. 530–533, 1908.

[67] D. Frenkel and B. Smit, *Understanding Molecular Simulation*. New York: Academic, 2nd ed. ed., 2002.

[68] K. Kremer and G. S. Grest, "Molecular dynamics simulation for polymers in the presence of a heat bath," *Phys. Rev. A*, vol. 36, pp. 3628–3631, 1986.

[69] B. Quentrec and C. Brot, "New method for searching for neighbors in molecular dynamicscomputations," *J. Comput. Phys.*, vol. 13, pp. 430–432, 1973.

[70] M. Allen and D. Tildesley, *Computer Simulation of Liquids*. Oxford: Oxford University Press, 1989.

[71] D. J. Evans and S. Murad, "Singularity free algorithm for molecular dynamics simulation of rigid polyatomics," *Mol. Phys.*, vol. 34, p. 327, 1977.

[72] P. Ewald, "Die Berechnung optischer und elektrostatischer Gitterpotentiale," *Ann. Phys.*, vol. 64, pp. 253–287, 1921.

[73] F. E. Harris, "Ewald summations in systems with two dimensional periodicity," *Inter. J. Quan. Chem*, vol. 68, pp. 385–404, 1998.

[74] I. Yeh and M. L. Berkowitz, "Ewald summation for systems with slab geometry," *J. Chem. Phys.*, vol. 111, p. 7, 1999.

[75] J. Hautman and M. L. Klein, "An Ewald summation method for planar surfaces and interfaces," *Mol. Phys.*, vol. 75, p. 379, 1992.

[76] M. Kawata and M. Mikami, "Rapid calculation of two-dimensional Ewald summation," *Chem. Phys. Lett.*, vol. 340, p. 157, 2001.

[77] S. Succi, *The Lattice Boltzmann Equation for Fluid Dynamics and Beyond*. Oxford: Oxford University Press, 2001.

[78] T. Lee and L. Liu, "Lattice Boltzmann simulations of micron-scale drop impact on dry surfaces," *J. Comput. Phys.*, vol. 229, pp. 8045–8063, 2010.

[79] T. Lee, "Effects of incompressibility on the elimination of parasitic currents in the lattice Boltzmann equation method for binary fluids," *Comp. Math. Appl.*, vol. 58, pp. 987–994, 2009.

[80] C. M. Elliott and S. Zheng, "On the Cahn-Hilliard equation," *Arch. Rational Mech. Anal.*, vol. 96, no. 4, pp. 339–357, 1986.

[81] L. Liu and T. Lee, "Wall Free Energy Based Polynomial Boundary Conditions for Non-Ideal Gas Lattice Boltzmann Equation," *Int. J. Modern. Phys. C*, vol. 20, no. 11, pp. 1749–1768, 2009.

[82] J. L. Jackson and S. R. Coriell, "Effective Diffusion Constant in a Polyelectrolyte Solution," *J. Chem. Phys.*, vol. 38, p. 959, 1963.

[83] J.-L. Barrat and L. Bocquest, "Large Slip Effect at a Nonwetting Fluid-Solid Interface," *Phys. Rev. Lett.*, vol. 82, p. 23, 1999.

[84] T. Tran, H. D. Malepradea, C. Sun, and D. Lohse, "Air entrainment during impact of droplets on liquid surfaces," *J. Fluid. Mech.*, vol. 726, p. R3, 2013.

[85] C. Clanet, C. Béguin, D. Richard, and D. Quéré, "Maximal deformation of an impacting drop," *J. Fluid Mech.*, vol. 517, p. 199, 2004.

[86] B. L. Scheller and D. W. Bousfield, "Newtonian Drop Impact with a Solid Surface," *AICHE J.*, vol. 41, pp. 1357–1367, 1995.

[87] I. V. Roisman, "Inertia dominated drop collisions. II. An analytical solution of the Navier-Stokes equations for a spreading viscous film," *Phys. Fluids*, vol. 21, p. 052104, 2009.

[88] M. Pasandideh-Fard, Y. Qiao, S. Chandra, and J. Mostaghimi, "Capillary effects during droplet impact on a solid surface," *Phys. Fluids*, vol. 8, p. 650, 1996.

[89] S. Chandra and C. T. Avedisian, "On the Collision of a Droplet with a Solid Surface," *Proc. R. Soc. Lond. A*, vol. 432, pp. 13–41, 1991.

[90] R. N. Wenzel, "Resistance of solid surfaces to wetting by water," *Ind Eng Chem*, vol. 28, pp. 988–994, 1936.

[91] A. B. D. Cassie and S. Baxter, "Wettability of porous surfaces," *Trans. Faraday Soc.*, vol. 40, pp. 546–551, 1944.

[92] T. Koishi, K. Yasuoka, S. Fujikawa, T. Ebisuzaki, and X. C. Zeng, "Coexistence and transition between Cassie and Wenzel state on pillared hydrophobic surface," *Proc. Nat. Aca. Sci.*, vol. 106, pp. 8435–8440, 2009.

[93] A. Giacomello, S. Meloni, M. Chinappi, and C. M. Casciola, "Cassie-Baxter and Wenzel States on a Nanostructured Surface:Phase Diagram, Metastabilities, and Transition Mechanism by Atomistic Free Energy Calculations," *Langmuir*, vol. 28, pp. 10764–10772, 2012.

[94] M. H. Jacobs, *Diffusion Processesa*. New York: Springer, 1967.

[95] R. Zwanzig, "Diffusion past an entropy barrier," *J. Chem. Phys.*, vol. 96, p. 3926, 1992.